Universitat Autònoma de Barcelona

Low-cost point-of-care biosensor device for clinical diagnosis in developing countries

Patricia Ramirez Priego

Universitat Autònoma de Barcelona

Doctorat en Biotecnologia

Departament de Genètica i de Microbiologia – Facultat de Biociències

Low-cost point-of-care biosensor device for clinical diagnosis in developing countries

Doctoral Thesis – 2020

Patricia Ramirez Priego
Author

Prof. Laura M. Lechuga
PhD supervisor

Dr. Esther Vázquez
Tutor

CSIC
Consejo Superior de Investigaciones Científicas

ICN2
Institut Català de Nanociència i Nanotecnologia
Excelencia Severo Ochoa

A mis padres

Abstract

Nowadays, Tuberculosis (TB) diagnosis is carried out at centralised laboratories, employing bulky equipment, complex reagents, and trained staff, increasing costs and the time to obtain the results. For that reason, the aim of this Doctoral Thesis is to develop a point-of-care (POC) platform able to deliver a prompt and reliable response to TB diagnosis, taking advantage of a highly sensitive evanescent wave optical sensor. The POC platform integrates a novel photonic sensor consisting of a Mach-Zehnder Interferometer transducer array incorporated in a disposable microfluidic cartridge.

Firstly, an optical characterisation was carried out to study the new POC performance and its ability to be employed for biosensing applications. Once the POC platform was optically characterised, diverse biofunctionalisation strategies were tested in order to incorporate specific antibodies as bioreceptors to the sensor surface. After an in-depth study, the optimal biofunctionalisation strategy was selected and employed for the analysis of the TB biomarkers. The TB biomarkers were evaluated in both buffer and biological samples, particularly human urine. The most promising and well-known TB biomarker was lipoarabinomannan (LAM), a bacterial cell wall component. In particular, this biomarker detection was validated with clinical samples from TB patients and healthy donors, showing the ability of our POC platform to discriminate those patients with active TB. Moreover, taking advantage of the photonic sensor design, which allows the simultaneous detection of six different biomarkers, we initiated the proof-of-concept of the POC platform for a TB biomarker panel detection using Dip-Pen Nanolithography for each corresponding bioreceptor deposition.

Our results, if validated with larger clinical studies, could have important diagnostic implications taking into account the advantages added by our POC biosensor in comparison with the methods recommended by the World Health Organisation.

Resumen

Actualmente el diagnóstico de Tuberculosis (TB) se realiza en laboratorios centralizados, empleando equipos voluminosos, reactivos complejos y personal capacitado, aumentando los costes y el tiempo para obtener los resultados. Por esta razón, el objetivo de esta Tesis Doctoral es el desarrollo de una plataforma *point-of-care* (POC) capaz de ofrecer una respuesta rápida y fiable en el diagnóstico de TB. Para llevar a cabo este objetivo, la plataforma POC integra un novedoso sensor fotónico incorporado en un cartucho de micofluídica desechable. El sensor fotónico consiste en un conjunto de interferómetros Mach-Zehnder que ofrecen una alta sensibilidad.

En primer lugar, se llevó a cabo una caracterización óptica para estudiar el rendimiento de la plataforma POC y su capacidad para ser empleada en aplicaciones biosensoras. Una vez caracterizada ópticamente, se evaluaron distintas estrategias de biofuncionalización para incorporar anticuerpos específicos como bioreceptores a la superficie del sensor. Después de un estudio en profundidad, se seleccionó y empleó la estrategia de biofuncionalización óptima para el análisis de los biomarcadores de TB. Los biomarcadores de TB se evaluaron tanto en solución tampón como en muestras biológicas, particularmente en orina humana. El biomarcador más prometedor y conocido de TB es el lipoarabinomanano (LAM), un componente de la pared celular bacteriana. En concreto, la detección de este biomarcador fue validada con muestras clínicas de pacientes con TB y donantes sanos, mostrando la capacidad de nuestra plataforma POC para discriminar a aquellos pacientes con Tuberculosis activa. Además, el diseño del sensor fotónico permite la detección simultánea de seis biomarcadores distintos. Teniendo esto en cuenta, hemos llevado a cabo una prueba de concepto del empleo de la plataforma biosensora POC para la detección de un panel de biomarcadores de TB utilizando nanolitografía *Dip-Pen* para la deposición de cada bioreceptor en cada sensor.

Nuestros resultados, validados en estudios clínicos más amplios, podrían tener importantes implicaciones diagnósticas. Además, nuestro biosensor POC ofrece una serie de ventajas en comparación con los métodos recomendados por la Organización Mundial de la Salud.

Agradecimientos

Después de estos años de esfuerzo y trabajo, no sería justo culminar esta etapa sin agradecer a todas aquellas personas que, directa o indirectamente lo han hecho posible.

En primer lugar, me gustaría dar las gracias a mi directora de tesis, la Profesora Laura Lechuga, por brindarme la oportunidad de realizar el doctorado en su grupo, y por toda la orientación y soporte recibido durante todo este tiempo. Gracias por confiar en mí cuando ni tan solo había terminado el grado, y por haberme animado a seguir en el mundo de los biosensores. Ha sido un autentico placer compartir y aprender tantísimas cosas de ti.

I would also like to thank all the partners involved in the European POCKET Project. Without your valuable work and help, it would not have been possible to carry out this Thesis. Mainly, I would like to express my gratitude to Prof. Mahavir Singh and Dr Ayssar Elamin from LIONEX Diagnostics & Therapeutics GmbH (Germany) for collaborating with us and provide us all the biological reagents and clinical samples. I would also like to thank Pieterjan Soetaert from TRINEAN (Belgium) for helping me to solve all the technical problems with the POC platform.

Agradecer también a todos los miembros y ex miembros del grupo nanoB2A por su apoyo en el día a día: Ana B., Jesús, Daniel, Santos, Adrián, Sonia, Priyanka, Roger, Berto, Maria, Alejandro, Leyre, Gisela y Paula. Durante todo este tiempo no he podido tener mejores compañeras de aventura, de despacho y de *escape rooms*, infinitas gracias a Olalla, Blanca y Nuria. Tampoc m'oblido de tots els moments *after work* i de totes les llagrimetes que ens han caigut al cinema, moltes gràcies per tots i cadascun dels moments viscuts Jessica. Agrair també tot el que m'ha ensenyat i tots els cops de mà que m'ha donat la M. Carmen. Gràcies a la Mireia per endolcir el final d'aquesta etapa i per transmetre'm aquesta energia tan positiva que desprèn. Bernat, llàstima que aquí no es puguin posar *stickers* per agrair-te tot el que m'has ensenyat i per tots els moments que hem compartit durant

aquest últim any pel laboratori. Quiero hacer una mención especial a Mª Cruz, que se ha convertido en mi mayor apoyo desde el primer día que llegó: muchísimas gracias por escucharme y apoyarme cuando más lo necesitaba. Por todos esos momentos de terapia y de risas en el trayecto de casa al trabajo y viceversa, y por todos los que están por llegar ahora que soy libre.

Muchísimas gracias a mi parcerita (Cristina) por hacerme más amenos los días en el laboratorio y por todos los momentos vividos juntas. Gracias también a mi medio paisano cordobés, César, por haberme dejado aprender tantísimo de él y por ayudarme siempre que lo he necesitado. Por todas esas lecciones sobre la vida que he tenido el placer de recibir por parte de mis "hermanas mayores" Rebeca y Cristina Kurachi, os quiero y os echo de menos. Espero veros pronto cuando la situación sanitaria lo permita. ¡Habéis sido unos compañeros excepcionales!

También quiero agradecer a los estudiantes de grado que he tenido el placer de supervisar y que me han ayudado con mi trabajo: Isabel y Pedro. Però sobretot agrair al meu primer estudiant, Miquel, al que li tinc un afecte especial i l'he vist créixer professionalment al laboratori.

Pero sobre todo quiero agradecer a la gran amiga que me dio esta etapa: Denise. Te echo mucho de menos, nunca me olvido de todo lo que vivimos juntas en Barcelona y mis Navidades por tu ciudad, New York. De ti aprendí muchas cosas y aunque hoy nos separen 6162 km nuestra amistad nos mantendrá unidas.

Por supuesto, no me olvido de mis amigas de toda la vida: Cristina, Sara y Noelia que han sobrellevado mi parcial y a veces total ausencia en sus planes. Muchas gracias a vosotras también por comprenderme y apoyarme en todo momento.

Gracias también a mi familia: mis primas y primos, tías y tíos, abuela y abuelo, que a pesar de la distancia siempre estuvieron a mi lado para saber cómo iban mis investigaciones.

Finalmente, todo esto no hubiese sido posible sin el apoyo incondicional de mis padres. Gracias por vuestros consejos y paciencia. Todo lo que soy hoy os los debo a vosotros por motivarme constantemente a alcanzar mis metas. Os quiero y os estaré eternamente agradecida.

Muchas gracias a todos.

Motivation and Objectives

Tuberculosis is an infectious disease caused by *Mycobacterium tuberculosis*. According to WHO, TB is the ninth cause of death worldwide and the first cause of death globally from a single infectious agent, ranking above HIV/AIDS. In 2018, TB infected 10 million people, resulting in 1.5 million deaths. Over 95% of TB cases and deaths occur in low-resource countries with weak health systems. However, registered incidence rates are low, especially in developing countries, due to the disadvantages of current diagnostic methods: cell culture, smear microscopy, and molecular tests. These techniques are slow, expensive, insufficiently accurate, time-consuming, not portable, and require trained laboratory technicians.

For this reason, a major effort is directed to the development of a prompt and reliable point-of-care (POC) biosensor platform. These platforms have the potential to miniaturise complex laboratory procedures, integrating all the functionalities in a single device. Hence, they should include a microfluidic cartridge, a biosensor transducer, and the electronics to receive and process the transducer signal. The biosensor integrated into the POC platform allows the detection of specific analytes related to a particular disease thanks to selective biological receptors (antibodies, proteins, DNA, RNA, and enzymes) immobilised onto the transducer surface. Biosensors have been applied to a plethora of disciplines, ranging from clinical and food analysis over environmental monitoring to biochemical research. In particular, optical biosensors are promising candidates for early TB diagnosis due to their rapid, simple, and highly sensitive detection. Besides, compared to other biosensor technologies, they add label-free, real-time, and multiplexed capabilities. Therefore, POC platforms integrating optical biosensors can provide rapid and straightforward results, enabling early TB treatment, improving patient outcomes, and stopping TB from spreading.

In this Thesis, we propose a new tuberculosis POC optical biosensor platform, which was developed within the frame of a European FP7 Project (POCKET) for the non-invasive detection of TB in human urine, taking advantage of the benefits associated with optical biosensors. The photonic

sensor chip is based on a highly sensitive Mach-Zehnder Interferometer transducer combined with an on-chip spectral filter and is incorporated into a disposable plastic microfluidic cartridge. The required elements for light coupling and optical readout are mounted into a prototype instrument, allowing real-time monitoring, data processing, and controlling the injection of fluids into the microfluidic sensing cartridge. The diagnostic focus of the POC platform is a panel of *M. tuberculosis* biomarkers present in the urine of TB patients to significantly enhance the sensitivity and specificity of TB diagnosis far beyond current diagnostics techniques.

This Thesis aims to evaluate the performance of the novel POC biosensor platform and to demonstrate its feasibility for use in the direct detection of TB clinical biomarkers with the following specific objectives:

1) Characterisation of the performance of the photonic sensor chips and the complete prototype instrument from a photonics and biological point of view.

2) Study and implementation of the most suitable biofunctionalisation strategy to anchor the selected biological receptors on the sensor surface to enhance analytical performance in terms of sensitivity, selectivity and reproducibility.

3) Evaluation of the best strategy to immobilise multiple biological receptors able to analyse a panel of TB biomarkers simultaneously using the same patient sample.

4) Optimisation and analytical characterisation of the POC biosensor platform for the identification of the selected TB biomarkers.

5) Validation of the POC biosensor platform with real clinical samples.

Table of contents

Chapter 1
Introduction

This Chapter provides an overview of the epidemiological situation of Tuberculosis worldwide, focusing on the active infection stage. The diagnostics methodologies are compared, stating their advantages and limitations. The Chapter also includes the description of how mycobacterium biomarker discovery has opened the path to more accurate, sensitive, and rapid Tuberculosis diagnosis. Finally, optical biosensors, mainly evanescent wave sensors, are presented as ideal candidates for Tuberculosis point-of-care testing in different scenarios.

1. Introduction

1.1. Tuberculosis: A Global Epidemic

Tuberculosis (TB) is an airborne infectious disease caused by the bacteria *Mycobacterium tuberculosis* (Mtb). The bacillus Mtb has several unique features compared with other bacteria, such as its slow growth and its peculiar cell wall structure, among others. This unusual coating composed of peptidoglycan, mycolic acid and arabinogalactan differs both gram-negative and gram-positive cell envelope, provides innate resistance to many antimicrobial drugs, and plays a crucial role in virulence.[1–3] Since Robert Koch announced the discovery of TB's causative agent in 1882, much scientific progress has been made for the prevention, diagnosis, and treatment of the disease. Despite these efforts, TB is still a significant global risk, and according to the 2019 World Health Organisation (WHO) report, TB is considered the leading fatal infectious agent, surpassing human immunodeficiency virus (HIV) and acquired immune deficiency syndrome (AIDS). In 2018, TB infected 10 million people, resulting in 1.5 million deaths (including 251 000 people with HIV) with more than 95% of these cases occurring in developing countries.[4]

TB usually affects the lungs, but it can also affect other parts of the body, such as the kidneys, brain, or spine. From a clinical perspective, patients with TB can be classified as having active or latent TB infection (**Figure 1.1**), and in both cases, Mtb is present in the human body.[5,6] In **latent TB**, the bacteria remain quiescent without infecting other individuals and do not cause symptoms. However, in **active TB**, Mtb is constantly multiplying with high infective potential. Patients with active TB experience a chronic cough, fever, haemoptysis (coughing up blood), chest pains, fatigue, lack of appetite, and weight loss.[4] Moreover, diagnostic and therapeutic treatments vary for latent and active TB infection. Current TB diagnosis methods based on microbiological tests are not able to detect TB in people with latent TB infection. Also, the treatment recommended by WHO for latent TB patients include isoniazid,

rifapentine, and rifampicin to prevent the evolution of the infection into an active state. Treatment for people with active TB includes a multidrug therapy with rifampicin, isoniazid, pyrazinamide, and ethambutol in order to stop the disease progression.[7]

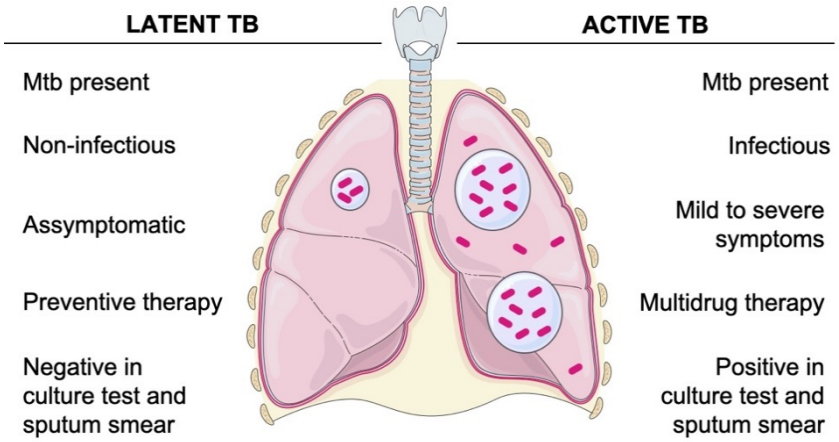

Figure 1.1. Schematic representation showing the main differences between latent and active TB.

WHO estimates that one-third of the world's population has latent TB infection, and 5–15% of those individuals will progress to an active TB state over months to a few years.[4] In contrast, the rest can eventually develop active TB during their lifetime.[8] Major risk factors to develop active TB include people with a weakened immune system, such as HIV, malnutrition, diabetes, tobacco smokers and alcohol use disorders.[4]

Mtb spreads from person to person through the air. Small droplets containing the bacilli are expelled by patients with active TB and enter other individuals via the respiratory tract. Detailed mechanisms involved in the immunology processes associated with TB infection can be found in the bibliography.[7,9–11] Briefly, as observed in **Figure 1.2**, once Mtb reaches the alveoli in the lungs, it is phagocytised by macrophages through the recognition and binding of different receptors. Automatically, other immune cells are recruited to the site of infection by cytokines secreted by

macrophages. All immune cells, in response to the microbial products, produce a reaction and generate small nodules called granulomas made up of bacteria, macrophages, dendritic cells, T cells, and human proteins that inhibit their intracellular growth. In the case of latent TB, the course of the disease stops at this stage, and Mtb only remains alive inside macrophages without further replication. However, in some cases with unclear causes, the infection process evolves into active TB. In these cases, the immune response is not enough to keep the bacteria under control, and they begin to replicate rapidly. In some specific cases, the bacterial load becomes too high, and the granuloma fails to contain the infection, disseminating the bacteria through the bloodstream to more distant tissues and/or organs.

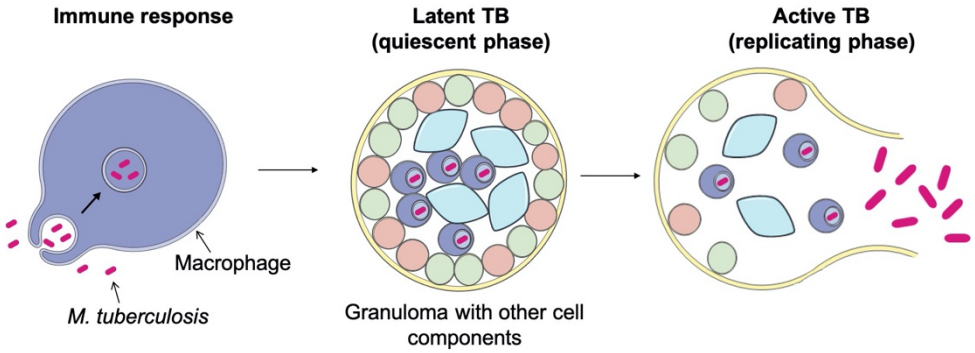

Figure 1.2. Schematic representation of TB infection progression.

1.1.1. Tuberculosis and HIV/AIDS interaction

Among the population, those with a major risk for the progression of latent TB infection into active TB disease are people having HIV. Indeed, WHO estimated that those with HIV infection are 19 times more likely to develop active TB than those without HIV.[4] Co-infection represents 12% of the total TB new cases worldwide (72% in developing countries, particularly in Africa), with mortality rates significantly higher than HIV-negative TB patients.[12,13] Several studies report that the higher mortality rates of TB and HIV co-infected patients are due to a combination of factors associated with: (i) the rapid progression of the infection because of the failure in Mtb growth inhibition, (ii) the delay in HIV/TB diagnosis

and treatment, and (iii) the higher reproducibility rates of multidrug-resistant bacteria due to the discontinued treatment rate.[14–17]

TB and HIV potentiate each other, accelerating the degeneration of immunological functions, resulting in rapid clinical deterioration and death.[18,19] One of the main features of HIV infection is the substantial reduction of CD4 (cluster of differentiation 4) T cells, which is a significant contributor in boosting 19-fold the risk of progression from latent TB infection to active TB disease and increasing susceptibility to Mtb re-infection (**Figure 1.3**).[17–21] This type of immune cell is also known to be essential for defence against Mtb infection. However, some studies indicate that the vulnerability of HIV patients to active TB increases 2–5-fold during the early phase of HIV infection when the number of CD4 T cells is that of healthy individuals (500 – 1 200 cells/μL).[21,22] These findings suggest that other immunological mechanisms, apart from CD4 T cells, are involved in TB and HIV co-infection and are not yet fully understood. Altogether, this is why WHO recommends antiretroviral therapy for all co-infected patients regardless of CD4 T cells counts in order to reduce mortality in this vulnerable group.

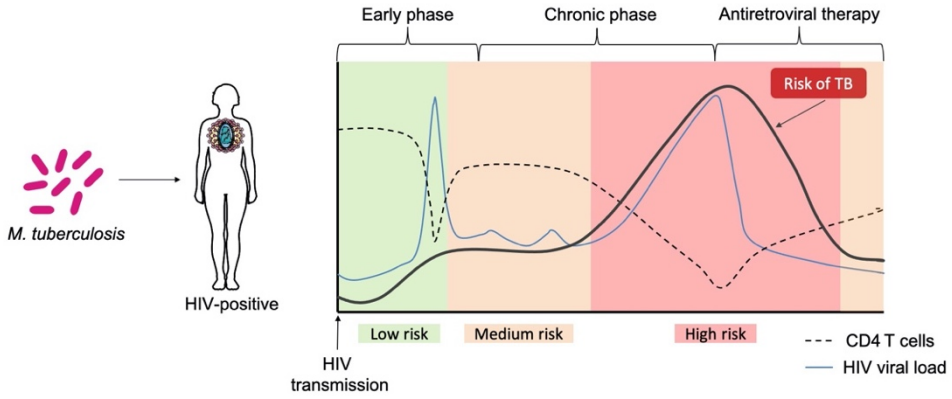

Figure 1.3. HIV patients increase the risk of developing active TB disease or re-infection with *Mycobacterium tuberculosis*. Adapted from [21].

1.1.2. Current diagnostics methods

Most TB patients can be cured with appropriate treatment, and hence, a rapid and precise diagnosis is one of the critical steps for a successful recovery. For this reason, early TB detection is one of the primary aims of WHO's End TB Strategy.[23] Because Mtb is only transmitted by individuals with active TB, the detection of the state of the disease is the priority of diverse programs for global epidemic eradication. Three principal methodologies for active TB diagnosis are used, supported, and recommended by WHO: culture-based methods, sputum smear microscopy, and rapid molecular tests (**Table 1.1**).[24]

The **culture-based method** is the gold standard technique. This test consists of the Mtb growth in a specific culture media using a sample of sputum, urine, blood, cerebrospinal fluid, or other tissues. This method provides the highest sensitivity and accuracy results compared with all other available TB diagnostic techniques. The minimum requirement is of 10 bacilli/mL in the sputum sample, allowing the detection of Mtb at an early stage.[25] However, the major drawback of this technique is the long incubation time for the growth of mycobacteria, taking up to 12 weeks to get results.[4] Consequently, additional understanding of Mtb growth factors need to be improved.[26]

Although the culture test is considered the gold standard, direct observation of stained Mtb microorganisms under the microscope (**sputum smear microscopy**) is still the most common diagnostic technique in developing countries.[27] *Mycobacterium tuberculosis* bacteria are difficult to stain because of its thick cell wall containing mycolic acids. However, they can be specifically stained by the Ziehl-Neelsen technique. Using this technique, the mycolic acids take on the colour fast and retain them inside the cell, looking like a bright red rod. The smear visualisation is more straightforward and less expensive than the culture test; however, its sensitivity and specificity are worse, requiring more than 5 000 bacilli/mL to detect the bacteria in stained sputum samples.[25]

In general, these two methodologies achieve sensitivities ranging from 32 to 94% and selectivity between 50 and more than 99%; however, they have some major drawbacks that include low precision, lengthy time to obtain the results and requirements for qualified personnel and laboratory equipment.[4,7,28]

Over the last years, advances in TB diagnosis have been achieved thanks to molecular assays. For this reason, since 2010, WHO began to recommend a new molecular test, **Xpert MTB/RIF** (Cepheid Inc., California, US), based on the polymerase chain reaction (PCR) amplification performed in a sputum sample.[29] This methodology allows the detection of Mtb and identifies mutations associated with rifampicin resistance, a common antibiotic employed to treat several infectious diseases.[30] Although Xpert MTB/RIF is more accurate than sputum smear microscopy with a time-to-result of 2 hours, it has not yet impacted in TB screening capabilities as compared with conventional tests.[31] Also, it incurs infrastructure limitations in resource-constrained settings, as it requires a very stable electricity supply, needs to be performed in a controlled temperature environment, with the addition of instrumentation, reagents, and cartridges costs and trained technicians.[4,31,32]

A faster methodology called **Loop-mediated Isothermal Amplification** (LAMP) has been extensively applied to several infectious diseases, including TB.[33] This simple technique consists of a temperature-independent method for amplifying DNA more rapidly than Xpert MTB/RIF and is easy to read under ultraviolet light.[34] The main advantage of this technique, in addition to those previously explained, is that it does not need sophisticated laboratories installations. However, the sensitivity is worse than for Xpert MTB/RIF, although better than for sputum smear microscopy.[34] Therefore, it is still necessary to perform more diagnostic accuracy studies on this methodology to determine its impact and effectiveness in TB diagnosis.[29]

Table 1.1. Comparison of the current diagnostics methods for active TB infection.

Test	Assay principle	Sensitivity (%)	Specificity (%)	Time to result	Cost[1]	Ref
Sputum smear microscopy	Direct visualisation of Mtb using a microscopy	32 – 94	50 – 99	Same day	+	[35]
Culture test	Mtb culture	73 – 89	>99	7 – 42 days	++	[36]
Xpert MTB/RIF	Nucleic acid amplification	67 – 98	99	2 hours	+++	[30]
LAMP	Nucleic acid amplification	76 – 80	97 – 98	<1 hour	++	[34]
LPA	Nucleic acid amplification	84 – 98	98 – 99	1 – 2 days	+++	[37,38]

[1]Including price/test, equipment and reagents

Another more complex molecular diagnostic test that can detect Mtb and isoniazid and rifampicin drug resistance is **Line Probe Assay** (LPA).[38] This test is based on a combination of multiplexed PCR amplification followed by a reverse hybridisation with specific oligonucleotides immobilised on a strip.[39] It takes longer than the Xpert MTB/RIF and can be performed directly on sputum samples or Mtb culture isolates.[40] The sensitivity for the direct detection of sputum specimens is equivalent to that obtained with Xpert MTB/RIF, but it takes one or two days to get results.[41,42]

In summary, all the above-described techniques are time-consuming, insensitive, or inaccurate. They can also be very costly and require complex procedures, sophisticated equipment, and skilled personnel. Taken together, these limitations make them unsuitable for placing them near to the patient or at the bedside (i.e., at point-of-care), leading to delays in initiating appropriate TB therapy and to an increase in ongoing Tuberculosis transmission. Consequently, there is an urgent need to develop rapid, highly sensitive, and specific devices to efficiently fight TB in resource-limited settings, which account for more than 95% of all TB cases and deaths.[43,44]

1.1.3. *M. tuberculosis*-derived biomarkers

A **biomarker** can be defined as a molecule or feature that is selectively measured as an indicator of normal biological processes, pathogenic processes, or pharmacological responses to a therapeutic intervention.[45,46] In the case of TB, biomarkers can be either specific from the host or the pathogen.[47] For instance, *M. tuberculosis* secretes specific antigens to survive and interact with host cells during the infection.[48] These secreted antigens can be present in body fluids from where they can reach the bloodstream and be eliminated in urine.[49] Thus, selecting specific TB biomarkers allows classifying patients as having active TB or no disease.

In the last few years, thanks to the advances in omics data analysis (genomics, proteomics, transcriptomics, and metabolomics), several antigens with diagnostic potential have been identified.[50] However, a recent review reveals that among 399 biomarkers candidates for TB diagnosis, only a few of them were confirmed in prospective studies (see **Table 1.2**).[51]

Table 1.2. Summary of main evaluated *M. tuberculosis*-derived biomarkers for TB diagnosis.

Biomarker	Acronym	Diagnostic evidence	Ref
Alanine proline rich secreted protein	Apa	Sputum and serum	52
Antigen 85 complex	Ag85	CSF, serum and sputum	53–55
6 kDa early secretory antigen target	ESAT-6	CSF, urine and serum	56–58
Heat shock protein X	HspX	Sputum and CSF	59,60
Lipoarabinomannan	LAM	Urine and sputum	61,62
Immunogenic protein MPT64	MPT64	Urine, sputum and serum	63–65
Phosphate-binding protein PstS1	PBP-1	CSF	52
Possible molybdopterin biosynthesis protein	MoeX	Urine	66
10 kDa culture filtrate antigen	CFP-10	Urine and sputum	63,67
Malate synthase G	GlcB	CSF	60

CSF: cerebrospinal fluid

Biomarker-based tests, which detect characteristic antigens of *M. tuberculosis* in biological fluids such as urine, sputum, and blood, have emerged as an alternative to current TB diagnosis methods. These promising tests are based on three main methodologies: Enzyme-Linked ImmunoSorbent Assay (ELISA), lateral flow tests, and biosensors.

ELISA is the gold standard of immunoassays. The methodology is a plate-based assay that allows the quantitative and qualitative detection of specific antigens present in a sample using antibodies labelled with alkaline phosphatase or horseradish peroxidase.[68] This methodology has been already used for TB diagnosis through the identification of LAM, ESAT-6, and CFP-10.[69,70] Despite the high sensitivity of ELISA, this technique presents several drawbacks (i.e., they are time consuming and require expensive reagents, the use of laboratory infrastructure and trained personnel), making them unsuitable for being translated to a POC device for in-field testing.

A faster methodology based on **lateral flow tests** is widely used in medical diagnostics. Briefly, lateral flow tests are paper-based devices in which the fluid sample migrates along the adsorbent pad with labelled antibodies and generates a visual result when an antibody recognises the specific analyte.[71] LAM, the most promising antigen detectable in the urine of patients with active TB and the one endorsed by WHO, is the only one with a commercially available POC test.[51,72] This test offers several advantages, such as rapid and direct detection of active TB disease in remote settings, where standard methods are challenging to be performed. However, some published studies suggest that the current commercially available tests are inaccurate for TB diagnosis.[73]

The implementation of TB diagnostic methods that overcome these limitations are still in demand. **Biosensors** are one of the preferred options, as these devices can offer straightforward, rapid, low-sample volume, and reagent consumption without the requirement of a laboratory or trained staff. Additionally, they can be integrated into a point-of-care (POC) platform allowing TB diagnosis in low-resource countries with weak health systems. Several biosensors have been already demonstrated their capabilities as a TB diagnostic tool.[28] However, they have not yet been transferred to clinical TB diagnosis.

1.1.4. Point-of-care platforms for Tuberculosis diagnosis

Over the past few years, there has been a trend to develop a low-cost, fully integrated, compact, easy-to-use, and portable **point-of-care** (POC) biosensor platforms. These platforms should provide a fast and accurate analysis near the patient site without the need for trained personnel and laboratory facilities.[74] These devices achieve these goals by miniaturising complex laboratory procedures and performing all the required diagnostic assay steps at the same device.[75–77] Furthermore, integrating all these procedures in a straightforward device allows the TB diagnosis to reach remote populations where TB burden is most significant, and the resources are scarce.

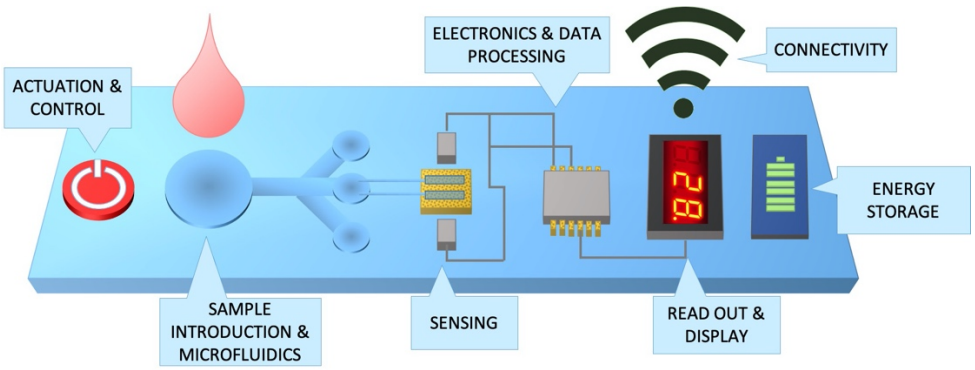

Figure 1.4. Ideal POC platform integrating microfluidics, sensing elements, electronic, data processing, among others. Additional features include low sample processing and real-time result display.

An ideal POC platform should contain on the same device all the required elements: (i) microfluidic, (ii) sensors with chemical or biological components, (iii) processing electronics, and (iv) the emitters and detectors for the read out. The results should also be displayed on a digital screen or sent to a remote display as smartphone or tablet (**Figure 1.4**). These platforms, commonly, use a disposable strip, chip or cartridge that incorporates microfluidics, guiding the sample to the sensing area and manipulating small volumes of fluids (micro to femtolitres). The main benefits of these devices include low sample and reagent volume consumption, fast turnaround time, portability, single-use, design

versatility, and potential for parallel operation.[75–80] All these benefits contribute to the reduction in analysis and manufacturing costs. In addition, POC platforms provide rapid results, enabling early treatment, stopping TB from spreading, and eventually improving the patient outcome.

According to WHO, the development of a successful POC platform in resource-limited environments should meet the ASSURED criteria[44]:

- Affordable: for those who need it.
- Sensitive: minimise or avoid false negatives.
- Specific: low false-positive rates.
- User-friendly: easy to perform by a non-trained person.
- Rapid and Robust: results should be available in less than 60 min after sample collection without requiring additional transport and storage (i.e., refrigeration).
- Equipment-free: no extra equipment required or small portable devices that use solar or battery power
- Deliverable to end-users

Beyond the ASSURED criteria, WHO consensus meeting for TB prevention, care, and control, additionally agreed on the target priority profiles (TPP) for the specific case of TB POC platforms. These devices should be cost-efficient, user-friendly, use non-sputum-based samples (i.e., urine, blood, or breath), and being performed at peripheral health centres and in community settings with limited laboratory infrastructures.[43,44] However, despite the enormous effort made in the last years towards integrated POC systems, very few complete working prototypes have emerged in the market for Tuberculosis diagnosis (see **Table 1.3**). Although, all of them exhibit some drawbacks, such as inaccurate TB diagnosis. Moreover, larger clinical studies should be performed to be recommended by WHO.

Table 1.3. List of current commercially available POC platforms for TB diagnosis.

TB Breathalyser (Rapid Biosensor Systems)

- Evanescent wave sensor
- Breath
- 2 min
- Sensitivity: 95%
- Specificity: 95%

Avisa BreathTest (Avisa Pharma Inc.)

- Mycobacterial urease activity
- Breath
- 10 min
- Sensitivity: N/A
- Specificity: N/A

INCLIX™ (Sugentech Inc.)

- Lateral flow test
- Blood
- 40 min
- Sensitivity: 95%
- Specificity: 60 – 85%

Alere Determine™ TB LAM Ag (Abbott)

- Lateral flow test
- Urine
- 25 min
- Sensitivity: 4 – 66.7%
- Specificity: > 98%

SILVAMP TB LAM (Fujifilm)

- Lateral flow test
- Urine
- 1 h
- Sensitivity: 70.4%
- Specificity: 90.8%

N/A: not available

1.2. Optical biosensors

The International Union of Pure and Applied Chemistry (IUPAC) defines a **biosensor** as an integrated analytical device capable of providing quantitative or semi-quantitative information using a biological receptor.[81] Biosensors consist of a biological receptor, a transducer, and an electronic system (**Figure 1.5**). Biological receptors usually include nucleic acids, antibodies, proteins, enzymes, or even whole cells. They are effective in biochemical recognition because they can selectively bind analytes through a wide range of affinity interactions. On the other side, the role of the transducer is the conversion of the specific biointeraction into a measurable signal proportional to the analyte concentration.[82]

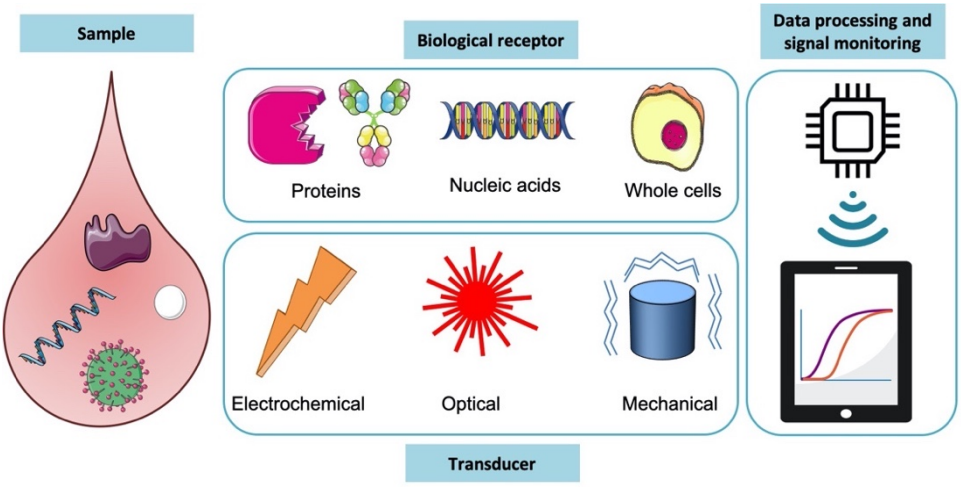

Figure 1.5. Schematic representation of a biosensor including the heterogeneous sample, the biological receptor, the transducer, and the data processing to achieve a signal.

Biosensors have been widely used because of their potential to perform tests rapidly with high sensitivity and specificity. Furthermore, a variety of biological receptor elements can be used to detect a wide range of different analytes. This confers biosensors with high versatility and the possibility to be employed in a broad range of applications ranging from medicine and food quality control to environmental management. Additionally, they can be integrated into low cost, portable, and easy-to-

use POC platforms, making them suitable for TB diagnosis in remote settings.

One of the most representative examples of biosensors is the glucose biosensor, which is widely used by millions of people who have diabetes. The device allows knowing the glucose concentration in a minimum blood sample amount in less than a minute, thanks to the interaction between the enzyme glucose oxidase and the glucose contained in the blood sample.[83]

Biosensors can generally be classified into electrochemical, mechanical, and optical sensors based on the physicochemical change experienced when the analyte binds to the bioreceptor. Amongst them, **optical sensors** are widely employed because they offer remarkable advantages such as excellent levels of sensitivity, direct, rapid, real-time sensing, and are highly suitable for being integrated onto a complete POC platform. The principle behind these transducers relies on the measurement of the variations of an optical property of the propagated light (i.e., intensity, wavelength, polarisation, or phase) produced by the interaction of the optical field with the biorecognition elements.[84] This results in a broad family of sensors that include absorption, fluorescence, luminescence, Raman spectroscopy, and refractive index-based techniques.

Optical biosensors can also be divided into label-based and label-free detection. In label-based sensors, a label is needed to generate a colourimetric, fluorescent, or luminescent signal. On the other hand, label-free transducers detect the interaction signal directly without the need of any tag.[85] These transducers are more advantageous because they do not need to modify the biomolecules to obtain the signal, which is more straightforward and cost-effective. Among optical label-free sensors, the most employed ones rely on the evanescent wave detection principle.

Evanescent wave sensors exploit the possibility of confining an electromagnetic field in a dielectric and/or metal structure, resulting in a

propagated or localised electromagnetic mode. Part of the confined light penetrates a few hundreds of nanometres into the external medium, generating an evanescent wave (**Figure 1.6**). The evanescent wave acts as a probe because it is extremely sensitive to refractive index (RI) changes of the external medium, which induce a change in the optical properties of the exciting electromagnetic mode through the evanescent wave tail. When a biological receptor is immobilised onto the surface of a waveguide, the exposure to the specific analyte produces a biological interaction, which in turn induces a RI change. This change directly affects the guiding properties of the light traveling in a waveguide through the evanescent wave. Furthermore, the RI variations can be quantitatively related to the concentration of the analyte and the kinetic parameters of the interaction.[86] Due to the exponential decay of the evanescent wave, only changes occurring close to the sensor surface will be sensed, thereby minimising the interferences with other substances present in the surrounding media.

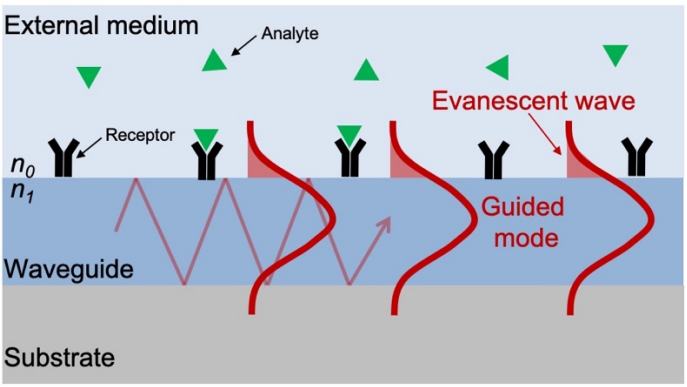

Figure 1.6. Schematic representation to illustrate the sensing principle of an evanescent wave biosensor.

Interferometers, resonators, and plasmonic biosensors are typical examples of evanescent wave biosensors.[87] These devices reach high sensitivity with a short response time. In addition, they do not suffer from electromagnetic interferences and have strong potential for miniaturisation, integration, and multiplexing.[88] Given all these advantages, the focus of this thesis was the study of the potential

application of evanescent wave biosensors in TB diagnosis. For this reason, in the next sections, we will describe in more detail plasmonic and interferometric sensors.

1.2.1. Analytical parameters for optical biosensors evaluation

The limit of detection (LOD) and sensitivity (S) are the most important parameters that define a sensor performance. **Sensitivity** is referred to as the strength of the light-matter interaction, representing the magnitude change in the transducer response to any change in the analyte concentration or refractive index. On the other hand, the **limit of detection** is defined as the minimum variation of the refractive index or analyte amount that can be accurately measured or quantified. This parameter depends on the system noise (i.e., light source, microfluidics, and temperature fluctuations) and is usually estimated as at least three times the standard deviation of the total system noise.

LOD is the most suitable parameter to compare the performance of different optical transducers. LOD can be estimated in two different ways: either employing the bulk sensitivity or the surface sensitivity (see **Figure 1.7**). In the case of evanescent wave sensors, the **bulk sensitivity** evaluates changes in the refractive index of the external medium in contact with the sensor surface (**Figure 1.7A**). This is carried out using solutions chemically inert to the material of the sensor surface and expressed in refractive index units (RIU). The **surface sensitivity** reflects the transducer intrinsic sensing capability where variations in the refractive index induced by molecular adsorptions or biomolecular interactions occur only in a thin layer in the proximity of the sensor surface (**Figure 1.7B**). This sensitivity can be calculated by De Feijter's formula[89] and is expressed as surface mass density in pg/mm^2. Another way to express the detection limit is by using the analyte concentration (i.e., ng/mL or molarity). In this case, LOD is referred to as the minimum amount of analyte detectable by the employed biosensor. However, this value is not comparable among different sensors because it is influenced by the analyte

molecule and the affinity constant of the biological receptors immobilised on the sensor surface with their corresponding analyte.

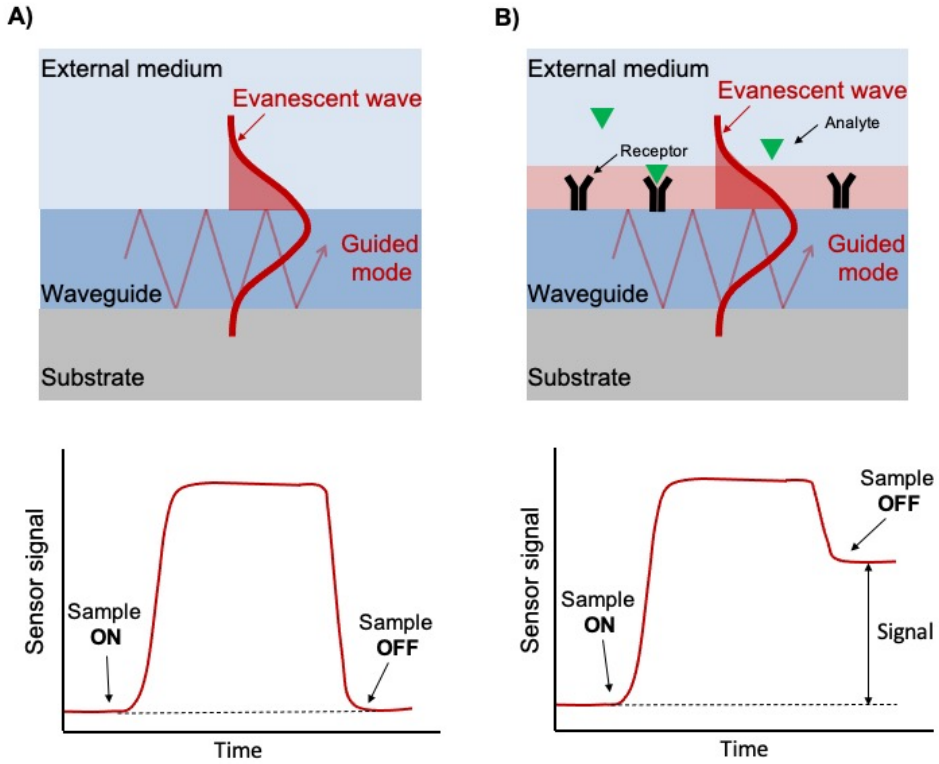

Figure 1.7. Schematic representation to illustrate the sensing principle and the obtained signals for **(A)** bulk sensitivity and **(B)** surface sensitivity

Table 1.4 shows a LOD comparison in RIU and pg/mm^2 for some optical sensors employed and described in this Thesis. LODs for plasmonic and interferometric sensors range from 10^{-4} to 10^{-8} RIU; however, depending on the immunoreagents and the transducer, a minimum analyte concentration of ng/mL or pg/mL can be obtained.[88]

Table 1.4. Comparison of the sensitivity in plasmonic and waveguide-based sensors.

Device	RI detection limit (RIU)	Mass detection limit (pg/mm^2)	Ref
Surface Plasmon Resonance	$10^{-5} – 10^{-7}$	1 – 5	90
Grating couplers	$10^{-4} – 10^{-6}$	0.3 – 5	91
Microring resonators	$10^{-5} – 10^{-7}$	1 – 3	92,93
Interferometers	$10^{-6} – 10^{-8}$	0.01 – 0.75	86,94

1.2.2. Plasmonic sensors

The field of plasmonics studies the interaction of light with noble metals. The most widely used plasmonic biosensor and the gold standard for characterisation of biomolecular interactions is the **Surface Plasmon Resonance** (SPR) sensor. It offers considerable advantages over conventional methods enabling analysis with excellent sensitivity and reproducibility with a time-to-result of a few minutes. SPR sensors have been used in a plethora of diverse applications, such as food quality, biomedicine, diagnostics, and environmental monitoring, among others.[95,96]

The SPR biosensor relies on the surface plasmon (referred to as propagating surface plasmon polaritons, SPP), which are free electrons that collectively oscillate at the interface between a thin metal film and a dielectric medium, generating an evanescent wave.[97,98] The most employed metal film is gold because it is an inert metal, can be interrogated with visible wavelengths of light, and can be functionalised through favourable gold-thiol interactions.

The excitation of the surface plasmon is achieved by coupling the light to the gold surface; however, it cannot be excited by direct illumination. Several techniques can be employed to couple the incoming light into the gold film, such as prism coupling, waveguide coupling, and grating coupling.[99] Prism coupler, called Kretschmann configuration, is

the most common method used to couple the incident light into the metal layer (**Figure 1.8**). The light passes through a high RI glass prism and is totally reflected at the prism base. The excitation of the surface plasmon generates an evanescent wave that penetrates the metal film and propagates along with the interface with a specific propagation vector. At some particular incidence angle (θ), the propagation vector will match the excitation of the surface plasmon, and at this point, a plasmon resonance occurs.

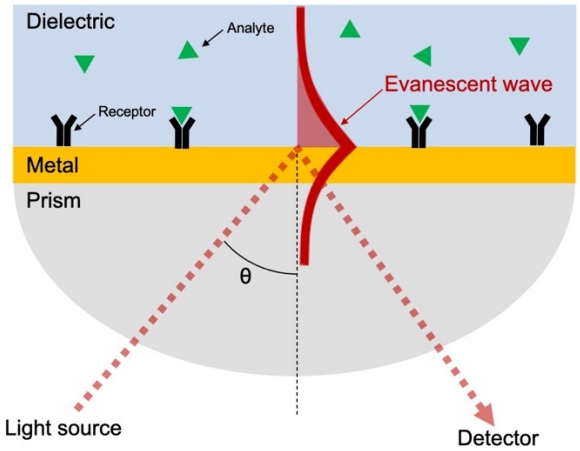

Figure 1.8. Schematic representation of a SPR biosensor employing a Kretschmann configuration to couple a monochromatic light into the thin metal layer.

Generally, an SPR biosensor employing a Kretschmann configuration consists of: (i) a light source (monochromatic or broadband) and a detector (intensity or phase-based) for excitation and interrogation of the propagating SPP, respectively; (ii) the plasmonic transducer, which usually consists of a thin layer of gold (≈ 50 nm) that incorporates the biological receptors on its surface; and (iii) a delivery system for injecting and running the liquid samples over the sensor surface (**Figure 1.8**).

SPR sensors can be classified according to the kind of light source, and the type of parameter monitored. Regarding the light source, they can

be polychromatic or broadband and monochromatic. The choice of the light source will also influence the measurement methodology of choice. There are three main measurement methodologies exist consisting of intensity modulation, angular or wavelength interrogation (see **Figure 1.9**). The working principle of intensity modulation is to detect the change of reflectivity at a fixed incident angle and a fixed wavelength (**Figure 1.9A**). On the other hand, angular or wavelength interrogation will define the shift of the plasmon resonance at a fixed wavelength or an incident angle, respectively (**Figure 1.9B**).[100] Despite the choice of the light or the measurement methodology, any RI change occurring at the dielectric interface will generate a shift in the signal that can be tracked at real-time. For instance, any biomolecular interaction occurring at the thin film gold surface will change the RI and produce a shift of the reflected light intensity. Besides, these RI changes are directly related to mass changes on the sensor surface, allowing label-free and real-time monitoring of any biomolecular interaction. The LOD of SPR sensors usually ranges between 10^{-5} and 10^{-7} RIU (see **Table 1.4**).

Despite the high sensitivity, the need for bulky prisms to achieve the surface plasmon excitations and the reduced multiplexing capabilities are some of the limitations for the integration of SPRs into a POC platform.[101] To overcome the limitations of the plasmonic sensors, photonic sensors based on integrated waveguides appear as an attractive solution for the development of a POC platform due to the higher sensitivity, multiplexing capabilities, and strong potential for mass fabrication using silicon-based technologies.[86]

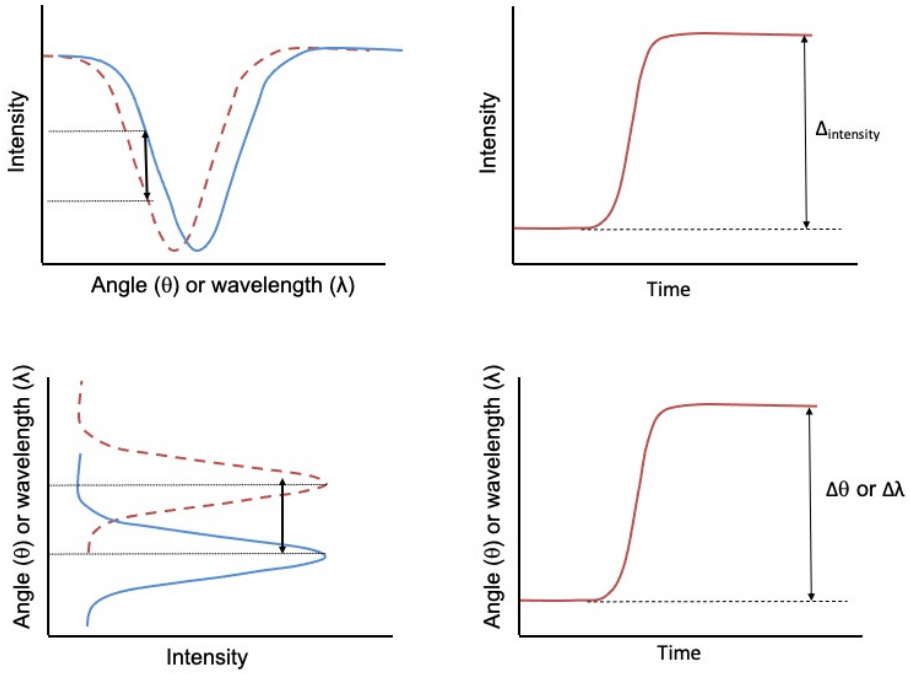

Figure 1.9. Sensorgram curve plot from the SPR measurement methodology by **(A)** intensity modulation, and **(B)** angular or wavelength shift interrogation.

1.2.3. Waveguide-based sensors

An optical waveguide is a geometrical structure usually made of dielectric material capable of propagating electromagnetic waves with minimal energy loss by total internal reflection. The simplest example of an optical waveguide is the so-called slab or planar waveguide, shown in **Figure 1.10**. This configuration consists of a high refractive index material (n_1) referred to as the core, surrounded by two lower refractive index materials (n_2 and n_3), corresponding to the bottom and top claddings. In such a structure, light propagates in the form of guided modes described by the electromagnetic field distribution and the velocity of propagation. These parameters depend on the waveguide structure (core thickness (d) and refractive index of the core and cladding materials (n_1, n_2, n_3)), and the working wavelength (λ). When the core of the waveguide is in contact with an external medium, any variation of refractive index at the surface will be translated into a change of the propagating wave mode,

due to the interaction through the evanescent wave, modifying the guided light characteristics.

Several technologies are available for the fabrication of waveguide-based sensors. In particular, the well-developed **silicon photonics** technology in the telecommunications field is opening a new era and revolutionising photonic industry. The fabrication of waveguide-based sensors is performed with silicon or silicon-related materials, which are compatible with complementary metal-oxide semiconductor (CMOS) processes and make feasible the mass production with high reproducibility. Moreover, the use of silicon and CMOS manufacturing allows the miniaturisation of the sensors into a compact device, enabling the fabrication of an array of sensors in the same chip, and thus, the analysis of several analytes simultaneously (multiplexing analysis).

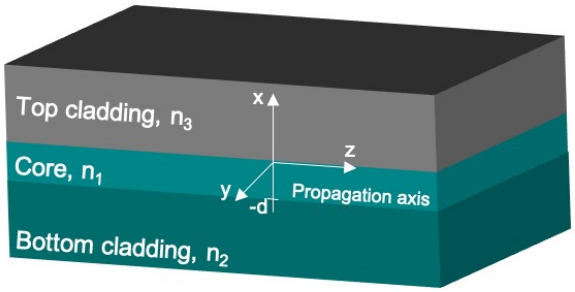

Figure 1.10. Scheme of an asymmetric slab waveguide.

The advantages of silicon-based sensors involve robustness, miniaturisation, excellent signal-to-noise ratio, low absorption losses of light, and high reproducibility in their fabrication and performance. Moreover, silicon-based sensors have already exhibited remarkable potential in multiple applications ranging from biomedical applications to environmental monitoring.

Several silicon-based sensors have been proposed as biosensors, including grating couplers, microring resonators, and interferometers.[102] Although all of them are based on the evanescent wave principle, each

configuration leads to a different sensitivity (see **Table 1.4**). Among all the waveguide-based sensors, interferometers have shown the best limit of detection.

1.2.3.1. Interferometric sensors

The working principle of interferometric sensors relies on the interference of two light beams that travel through different optical paths.[89] For biosensing applications, one of the optical paths has a portion of the core waveguide exposed to the external medium, the so-called sensing area, while the other acts as a reference. Any refractive index change or biomolecular interaction which occurs in the sensing area will introduce a phase change in the interference pattern, resulting in a sinusoidal signal with an amplitude and number of fringes proportional to the concentration of the analyte producing the phase variation. This variation is proportional to the interaction length of the evanescent field with the sample and, therefore, the sensitivity can be improved by enlarging the path in the sensor area. The most common interferometric sensors are the Mach-Zehnder Interferometer and the Young Interferometer.

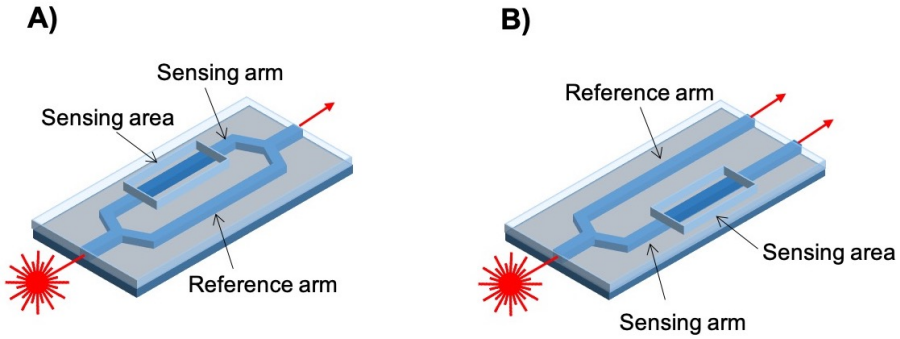

Figure 1.11. Schematic representation comparing a **(A)** Mach-Zehnder and **(B)** Young Interferometers.

In a **Mach-Zehnder Interferometer** (MZI), the two arms are recombined into a single output waveguide through a second Y-junction

before arriving at a photodetector or CCD camera, which collects the interferometric signal (see **Figure 1.11A**). In the case of **Young Interferometer** (YI; **Figure 1.11B**), the two arms are not recombined before the output. The output light from the two waveguides is projected onto a screen, creating an interference pattern.

MZI has been the most common interferometric configuration employed in the biosensor field with a wide variety of applications. However, just a few research groups and an industrial company have demonstrated an in-depth experience with this technology. The involved groups include Lionix International (Netherlands), Microelectronics Department at the National Centre for Scientific Research "Demokritos" (Greece), and our research group at ICN2. Each of them has developed their own MZI design following the working principle of a MZI interferometric sensor.

In 2014, Misiakos et.al. developed an integrated silicon chip (4 x 9 mm^2) that contained ten light emitting diodes as the light source of ten individual MZI sensors. Then, the light output from the MZI was monitored by a unique external spectrometer shared by all transducers (see **Figure 1.12A**). An appropriate fluidic cell was attached on top of the sensor at the wafer level (see **Figure 1.12B**) to deliver the sample over the sensing area. In this way, multiple analytes could be evaluated with a delay of a few ms in between.[103] A final validation of the device for multiplexing analysis achieved a LOD in the pM range, demonstrating the biosensing capability of these interferometric sensors.[104]

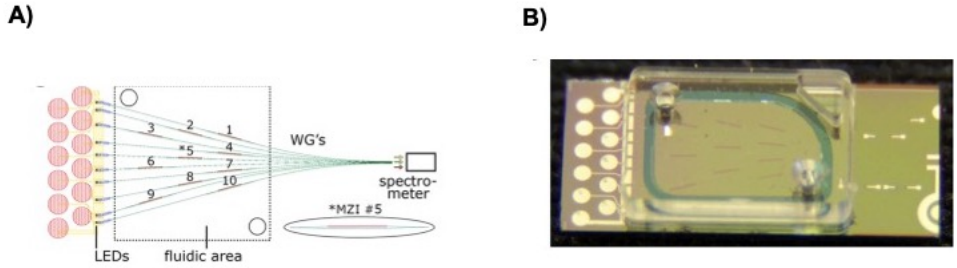

Figure 1.12. **(A)** Layout of the ten MZI transducers showing the sensor routes as well as the diodes positions and external spectrometer. **(B)** Photograph of the silicon chip carrying the microfluidic. The ten MZI transducers are visible under the cover.

More recently, Lionix International developed an integrated asymmetric MZI containing six transducers (**Figure 1.13A**). A polymer flow cell with four independent microchannels was implemented in a cartridge. The optical connection of the sensor cartridge was facilitated by a 12-channel fiber array attached to the edge of the chip (see **Figure 1.13B**). The full integration was tested by our research group and applied to the detection of Tetracyclin and Irgarol 1051, achieving a LOD in the pg/mL range.[105] This device was employed within the European Union BRAAVO Project aimed to allocate this biosensor device in stand-alone buoys in the ocean.

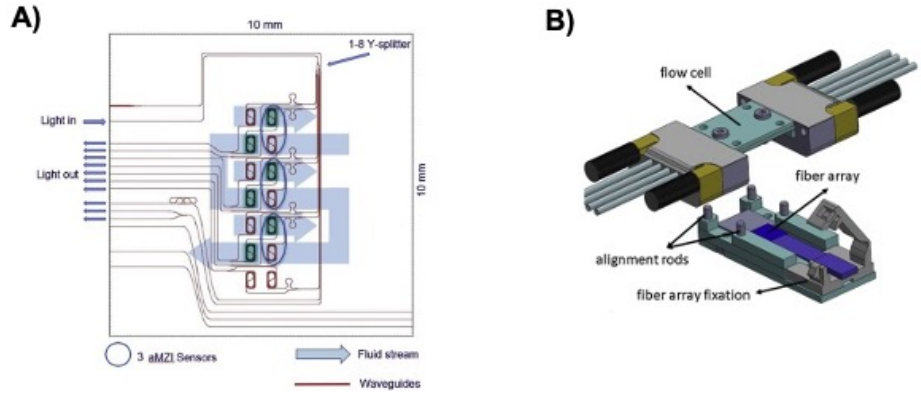

Figure 1.13. (A) Layout of the sensor chip and flow paths over the different sensors. **(B)** 3D scheme of the flow cell assembly.

Additionally, our research group developed a MZI sensor chip (1 x 3.2 cm) containing nine transducers and twenty-four waveguides. Grating couplers were employed to couple the light in order to improve the integration into a POC platform.[106] A bulk sensitivity of 10^{-7} RIU was achieved, and a proof-of-concept for the detection of human serum albumin was described.[107]

A different interferometric concept, the **Bimodal Waveguide Interferometer** (BiMW), was proposed by our group as an elegant alternative which can avoid the light beam splitting and recombination, while keeping an interferometric behavious.[108] The working principle of the BiMW sensors relies on the behaviour of light propagating through a specific design of a waveguide, which allows only the propagation of the fundamental and first propagating modes of a polarised monochromatic light (**Figure 1.14**). In brief, a monochromatic and polarised light is first confined through the waveguide core in a single (fundamental) mode. This fundamental mode is coupled into a bimodal section after a certain distance through a step junction that allows the first propagating mode appearance. These two modes travel across the sensing area and exit the waveguide. A sensing window is opened along the waveguide bimodal section, where the bioreceptors are immobilised, and the detection occurs. Therefore, any refractive index change in this area affects the propagating modes and results in an interferometric phase shift between the two modes, which is collected by a two-sectional photodetector at the end of the sensor device. The sensitivity level of BiMW is comparable to other interferometers, with a LOD of 10^{-7} – 10^{-8} RIU.[108,109]

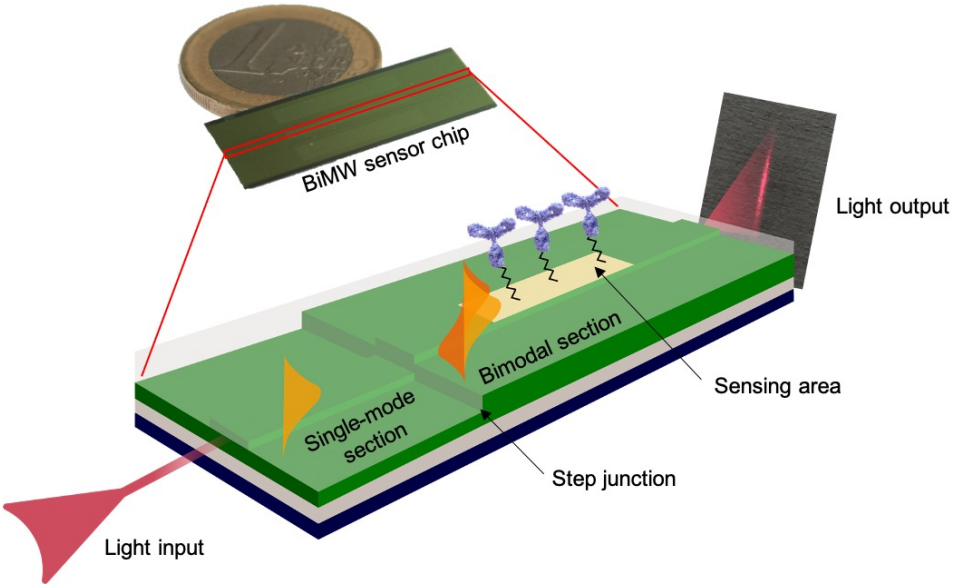

Figure 1.14. Photograph of a BiMW sensor chip. Zoom in one of the bimodal waveguides shows a schematic representation of the working principle.

1.3. The bioreceptor layer

The development of a highly sensitive and reliable POC biosensor relies upon the successful development of biofunctionalisation strategies anchoring specific biological receptors to the sensor surface. The strategy must be reproducible and provide a controlled bioreceptor immobilisation that ensures high interaction efficiency with the analyte and reduces non-specific adsorptions from sample components.

A wide variety of biological receptors can be employed in biosensor devices, and they can be categorised in accordance with the nature and its biochemical interaction with the analyte into catalytic and affinity bioreceptors.

The interaction of the substrate (analyte) with the catalytic bioreceptor transforms the analyte into a product, modifying chemically their structure. **Enzymes** are proteins commonly used as catalytic receptors

(**Figure 1.15**). These proteins reduce the activation energy needed for a certain chemical reaction to transform a substrate into a product. In biosensors, these kinds of reactions are monitored by the reduction of the substrate or by detecting the final product of the reaction.

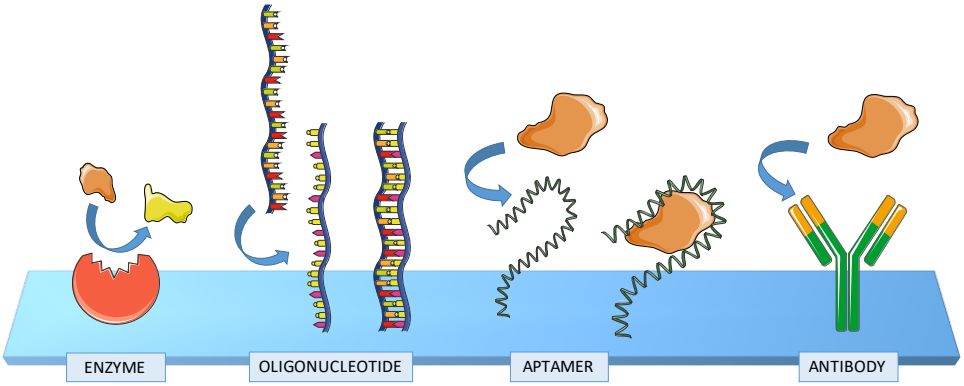

Figure 1.15. Summary of some biological receptors used in biosensors.

On the other hand, there are affinity bioreceptors that recognises specifically the analyte. The binding pairs (receptor – analyte) can be broadly classified into three classes: nucleic acids – DNA/RNA, aptamers - antigens and antibodies – antigen. **Nucleic acid** sequences can be used as receptor probes because they can bind with high affinity to complementary DNA or RNA strands. The binding affinity will depend on the sequence composition and the length of the complementary region. In addition, the buffer composition used during the hybridisation can modify the affinities, preventing also the binding of non-specific sequences that share some similarity.

Aptamers are also single stranded oligonucleotide sequences (DNA or RNA) that are folded in such a way that form secondary structures that recognise analytes (e.g. proteins) with high affinity. These sequences are identified by a procedure known as SELEX (Systematic Evolution of Ligands by Exponential Enrichment). The procedure begins using a large sequence library that is exposed to the analyte of interest under stringent conditions. Then, the bound sequences are eluted, amplified and

sequenced. After several cycles of selection, only the sequences with the highest affinity are kept and can be used as bioreceptors.

Finally, **antibodies** are widely used as biological receptors due to their extraordinary affinity and specificity against their specific target molecule.

1.3.1. Antibodies as biological receptors

Antibodies, or immunoglobulins (Ig), are proteins produced by the immune system in response to foreign molecules in the body, known as antigens. An antibody is a Y-shaped molecule composed of four polypeptide chains, two heavy (H) chains, and two smaller light (L) chains with a molecular weight of 50 and 25 kDa, respectively, linked by disulfide bonding (**Figure 1.16**). Each chain contains a variable (V) and a constant (C) region. Antigen recognition is mediated by the variable light and heavy domains, also known as fragment antigen-binding (Fab) region and situated at the Y arm ends. This Fab region differs in sequence and structure among different antibodies because it is the region involved in recognizing the specific antigen. The Y-shape base is composed of the H chain constant domains, known as the Fragment crystallizable (Fc) region. This region plays a key role in activating the immune system, ensuring that each antibody generates an appropriate response for a given antigen. Furthermore, this region can also bind to cell receptors and complement proteins.

There are five antibody isotypes in mammalian cells denoted by their different structure of H chains: IgA, IgD, IgE, IgG, and IgM. IgG is the predominant antibody class produced during an immune response and the most employed in immunoassays as a biological receptor. The antibody recognition ability is due to the simultaneous formation of several non-covalent bonds with the specific antigen (e.g., electrostatic and hydrophobic interactions, ionic and hydrogen bonds, and van der Waals forces). These weak bonds are only possible if the antigen structure closely matches with the Fab region of the antibody, and the association can persist for an extended period.

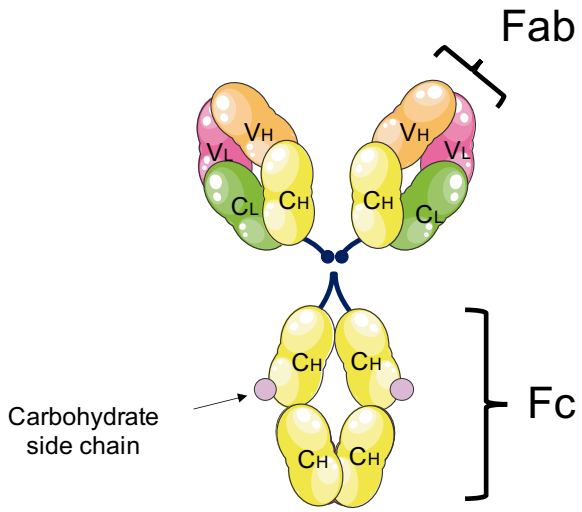

Figure 1.16. Basic structure of an antibody.

Antibodies are produced in laboratories for a wide range of applications. According to the production process, antibodies can be classified into two primary types: monoclonal and polyclonal antibodies. The production of **polyclonal antibodies** (pAb) involves the repeated immunisation of an animal (e.g., rabbit, goat, and sheep) with the desired antigen. The host immune system reacts to the specific antigen, and its B lymphocytes start producing antibodies. These antibodies directly obtained from the animal serum are a heterogeneous mixture of polyclonal antibodies produced by different B lymphocytes clones. This mixture recognises different binding sites of a single antigen, showing different affinity and specificity.

The obtention of **monoclonal antibodies** (mAb) begins in the same manner as pAb production, generating an immune response from the immunised animal. However, rather than collecting serum, mAb production requires collecting the antibody-producing spleen or lymph nodes cells from the host animal, the B lymphocytes. These B lymphocytes are fused with immortal myeloma cells, resulting in a hybrid

cell known as hybridoma. The resulting hybridoma, generated by identical B lymphocytes, is used to create an immortal cell culture line that produces antibodies that recognise explicitly only one binding site of the antigen with high affinity.

Thanks to their capabilities to recognise specific antigens, antibodies play a crucial role in developing immunoassays. Their unique combination and diversity make them not only indispensable for clinical diagnosis but also in environmental monitoring, and food analysis, among other fields.

1.4. Tuberculosis diagnosis in the frame of FP7 POCKET Project

TB is a major global health issue. While most TB cases occur in developing countries, this disease is also re-emerging as a threat to the largest urban European populations due to the increase in global travel and movement. The early treatment of TB is currently hindered by the lack of rapid and accurate diagnostics tools, especially those that can be applied as POC platforms in resource-constrained settings. Alternative testing methodologies do exist, but they either come at a high cost or lack sensitivity. Given these issues, developing a POC platform for the early TB diagnosis was proposed within the frame of European FP7 POCKET Project.

The POCKET Project aimed to integrate several novel technologies into a POC platform to provide a low-cost and sensitive TB diagnosis by combining nanophotonics and novel selective antibodies. The novel tool was designed to detect specific TB biomarkers in urine, filling the gap between current high-end, sensitive, but expensive tests plagued by limited accuracy. The specific objectives and activities of the EU Project included:

- Development of a highly sensitive Mach-Zehnder Interferometer array able to analyse several TB biomarkers at the same time.

- Integration of the novel nanophotonic transducer in a disposable microfluidic cartridge to avoid sample manipulation and reduce the required sample volume.
- Producing a novel TB detection system based on a unique combination of high-quality antibodies for different biomarkers.
- Construction of the first POC prototype instrument for the read out that integrates all the required elements for the label-free, real-time, rapid, and sensitive TB diagnosis.

The complete POC platform achieved in the project is reviewed in more detail in Chapter 2. The overall objective was the development of a novel POC urine test for the detection of Tuberculosis, achieving low-cost (5 to 10 € end-user cost per test), and high accuracy at the same time. Reaching this milestone would help patients to start with the corresponding treatment earlier and reduce TB spreading. **Figure 1.17** shows all the partners involved in the Project.

Figure 1.17. Logo of the partners involved in the POCKET Project.

The **Nanobiosensors and Bioanalytical Applications** group at the ICN2 and CSIC participated in the project with its expertise in the field of surface biofunctionalisation for biosensors development. The main tasks assigned within the Project were:

- Optimisation of the biofunctionalisation protocol for each TB biomarker proposed in the Project for its final evaluation in human urine.

- Obtaining calibration curves with the novel POC platform for each TB biomarker using spiked urine.
- Evaluation of the diagnostic performance of the novel POC platform using clinical samples from TB patients.

In this doctoral thesis, we have included the main results achieved during and after the Project in order to fully demonstrate the capabilities of the new POC optical biosensor platform for the projected application in TB diagnostics.

Chapter 2
Novel point-of-care biosensor device based on silicon photonics technology

In this Chapter, the point-of-care biosensor platform implemented in the European project is thoroughly described. First, the photonic sensor chip is detailed, including the working principle and the fabrication process at Clean Room facilities. Then, its integration in a disposable microfluidic cartridge and the assembly of the complete prototype instrument are described. Finally, the device optical characterisation was carried out to study its performance and its ability to be employed for sensing applications.

2. Novel point-of-care sensor device based on silicon photonics technology

2.1. Nanophotonic sensor chip: design and fabrication

The transducer employed in this Thesis is an integrated Mach-Zehnder Interferometer based on silicon photonics technology. In the frame of the European POCKET Project, a novel configuration of an MZI transducer was developed, combining an on-chip spectral filter for the signal readout (see **Figure 2.1** for details).

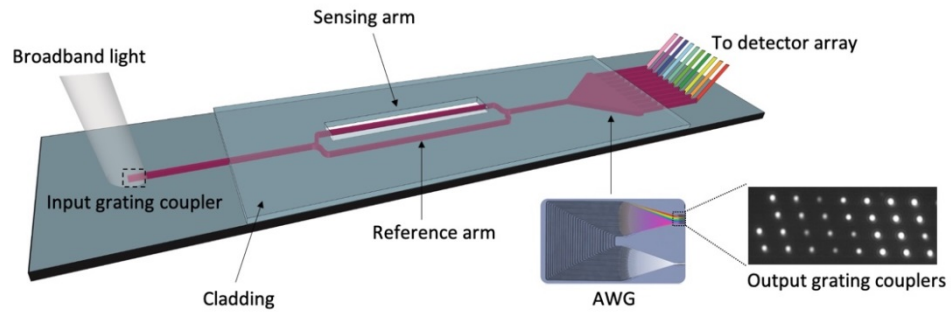

Figure 2.0.1. Layout of the photonic sensor chip based on Mach-Zehnder Interferometer transducer and readout by an on-chip spectral filter.

In this transducer, a broadband light emitted from a superluminescent diode (SLED, 850 nm) is coupled into a single-mode silicon nitride waveguide by means of a grating coupler. After passing through a Y-junction, the light is divided into two equal beams that are coupled in two single-mode waveguides, one being the sensing arm and the other one the reference arm. The light traveling along the two waveguides merges in a second Y-junction. Afterwards, the MZI light output that carries all the wavelengths is connected to a thirty-channel Arrayed Waveguide Grating (AWG), selected as an on-chip spectral filter. Briefly, an AWG works as a prism: it diffracts and splits incoming light into an array of thirty waveguides with a fixed difference in the optical path length between the adjacent waveguides.[110,111] As a result, there are thirty output grating couplers, each of them carrying an unique light wavelength between 800-

900 nm, which are taken as output signals with a complementary metal-oxide-semiconductor (CMOS) image sensor. Both input and output grating couplers are specifically designed to work at 850 nm.

As shown in **Figure 2.1**, the top cladding layer covers the Y-junction and the reference arm, only allowing the sensing arm to be in contact with the sample. Due to the evanescent wave mechanism (explained in detail in the Introduction section) the refractive index variations of the external medium (i.e., biomolecular interactions or bulk refractive index) cause a change in the optical properties of the light traveling in the waveguide, due to the effective refractive index difference of the MZI sensing arm as compared to the reference one. Consecutively, this change results in a light phase shift in the sensing arm, and, therefore, a wavelength shift of the whole spectrum of the MZI output. This shift is tracked by monitoring the locations of the MZI spectral peaks. The location of these peaks can be analysed by using the algorithm created by *Martens et al.*[112] from Ghent University (Belgium). This algorithm precisely extracts the output power of each output grating coupler from the CMOS sensor, as shown in **Figure 2.2A,B**. The tracked shift (**Figure 2.2C**) is directly proportional to the specific analyte mass involved in a given biomolecular interaction on the sensor surface, providing quantitative and qualitative information in real-time.

Within the EU project, the **photonic sensor chips** were designed by Ghent University and were fabricated at wafer-scale in the cleanroom facility of IMEC (Belgium) using a 200 mm silicon wafer. The fabrication process is based on the well-established CMOS-compatible technology for large-scale production, including photolithography and etching processes over a standard silicon wafer substrate.

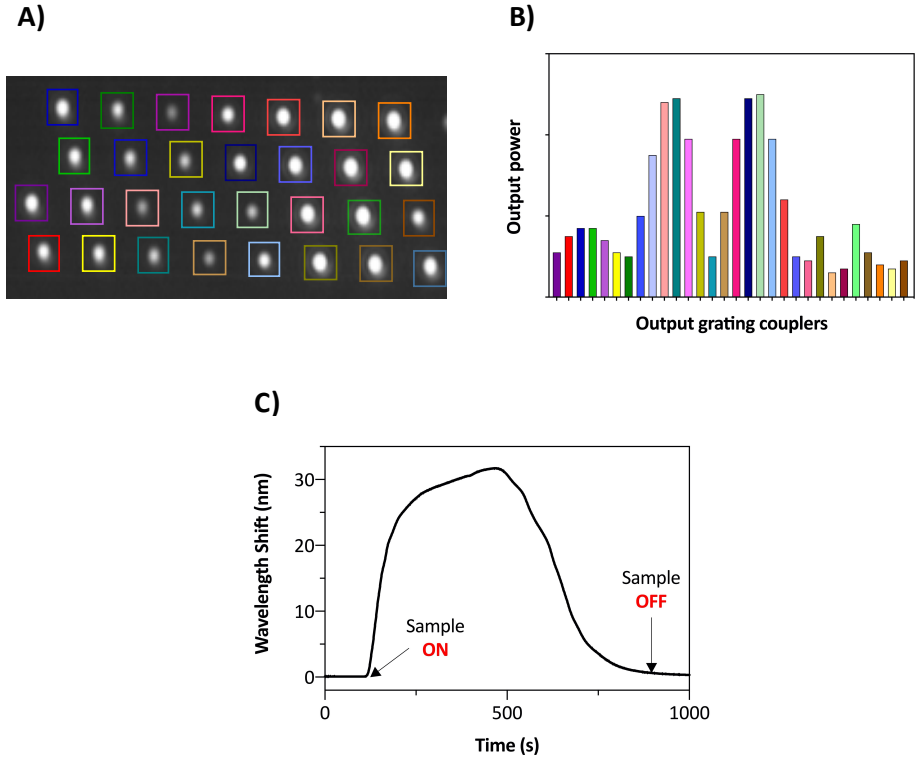

Figure 2.0.2. (A) CMOS image of the output grating couplers of one MZI biosensor. **(B)** Output power of each output grating coupler extracted with the algorithm. **(C)** Bulk refractive index change monitored in real-time with the algorithm for one MZI sensor.

A schematic representation of the photonic sensor chip fabrication process is shown in **Figure 2.3**. The procedure starts by depositing a 70 nm thick layer of anti-reflective silicon nitride (Si_3N_4) onto a standard silicon wafer by plasma-enhanced chemical vapour deposition (PECVD). The main goal of this layer is to decrease the back-reflections and increase the light coupling efficiency of the grating couplers. After, a 2.3 µm thick layer of silicon oxide (SiO_2) is deposited by PECVD. The roughness of this layer is reduced by a gentle chemical-mechanical polishing (CMP) step. Afterwards, a 220 nm thick layer of Si_3N_4 is deposited on top by PECVD to minimise light propagation losses.

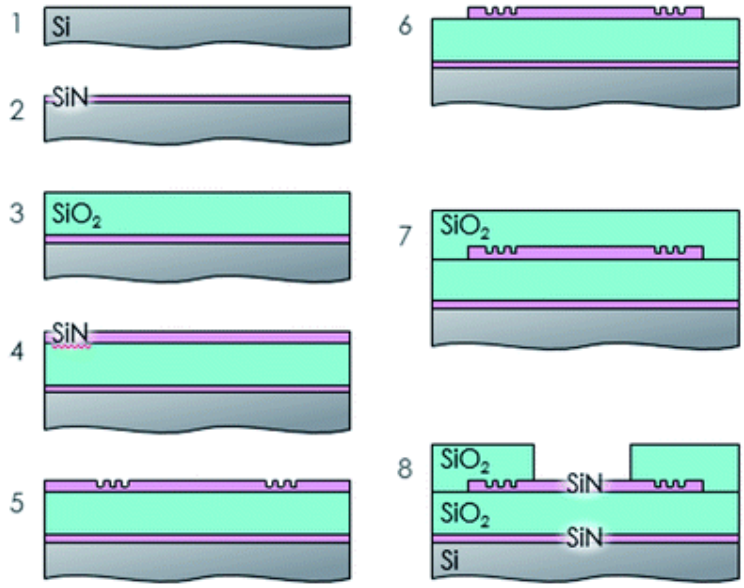

Figure 2.0.3. Scheme of the fabrication process flow for the photonic sensor chip at cleanroom facilities. (1) Si substrate, (2) deposition of the anti-reflective coating, (3) deposition and chemical-mechanical polishing of the bottom clad, (4) deposition of the silicon nitride (SiN) waveguide layer, (5) shallow etch of the grating couplers, (6) deep etch of the waveguides, (7) deposition and chemical-mechanical polishing of the top clad, and (8) clad-open etch.

Subsequently, grating couplers and waveguide structures are patterned. First, two individual photoresist masks are implemented using a deep ultraviolet (DUV) lithography to optimise the critical dimensions separately. Then, fluorine-based inductively coupled plasma reactive ion etching (ICP-RIE) is employed to minimise roughness and achieve the required sidewall slope. The waveguides are then produced by etching the full thickness of the Si_3N_4 layer, while the grating couplers are shallowly etched down to 110 nm depth into the Si_3N_4 layer, to maximise light coupling into the waveguide. Later, a 2 μm layer of SiO_2 is deposited via PECVD and flattened by CMP. Finally, sensing regions are opened by lithography using mercury lamp at 365 nm followed by a selective removal of the SiO_2 that covers the Si_3N_4 waveguides using a dry etching process and a wet etching step.

This fabrication allows a wafer-level manufacturing, producing a total of 232 photonic sensor chips in the same process, each of them containing six MZI sensors and a reference sensor (**Figure 2.4**). This procedure enables a reduction in time and fabrication costs, as well as the decrease of the analysis costs and the miniaturisation of the sensor chip size.

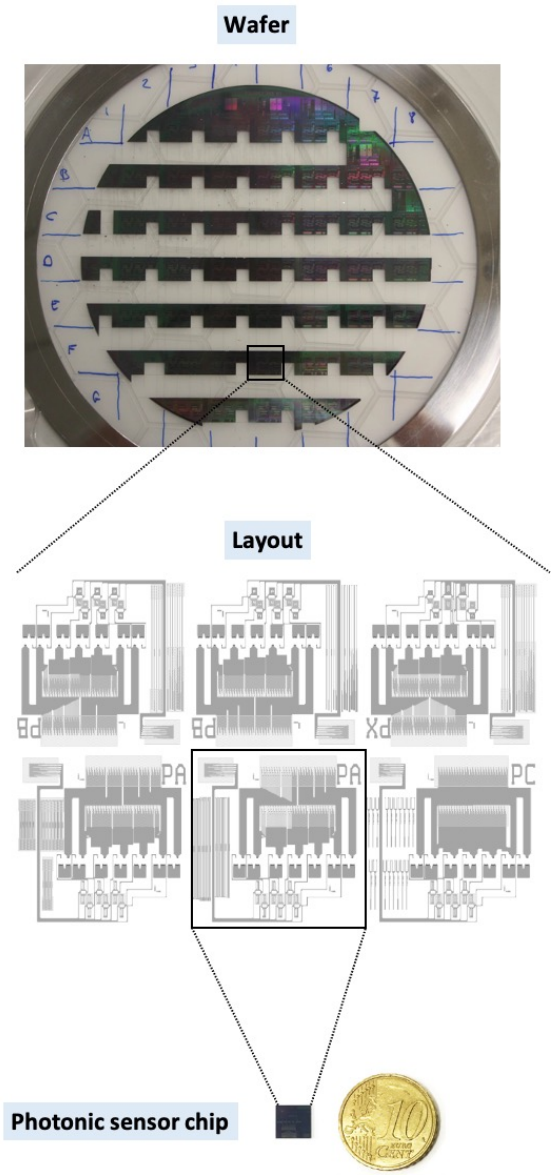

Figure 2.0.4. Wafer containing 232 photonic sensor chips with six MZI and one reference each one.

Figure 2.5 shows a photograph of a photonic sensor chip (7.16 x 6.76 mm) with all the integrated elements. As mentioned previously, the photonic sensor chip contains six MZI sensors and a reference sensor (**Figure 2.5B**). This layout allows for the simultaneous detection of multiple analytes and increases the performance and accuracy of the analysis. The reference sensor is used to compensate for the slight dispersion of the grating couplers, the light source, and the on-chip spectral filter. Therefore, it further increases the accuracy of the read-out. Each sensor is supplied in parallel with the light coming from a SLED broadband source, through the separated input grating couplers (**Figure 2.5A**) (20 x 20 μm; pitch: 100 μm). These input gratings are stacked tightly together to allow the SLED to supply power to all of them simultaneously. The sensors are placed linearly and rolled up with the sensing arm folded inwards (180 x 270 μm for each sensing and reference arm area) ensuring optimal usage of the available space. The output of each sensor, including the reference one, is connected to a thirty-channel AWG (channel bandwidth: 2 to 5 nm; channel pitch: 2 to 5 nm), which works as an on-chip spectral filter (**Figure 2.5D**). Other separated output grating couplers are stacked in two separate sets, each one with rows of four in a staircase configuration (**Figure 2.5C**). These couplers are used to confine the light from the AWG into a CMOS sensor that monitors the intensity of the different spectral channels simultaneously. In this way, a high number of grating couplers fit within the CMOS window, while still maintaining the requirements in terms of wavelength length and spatial separation.

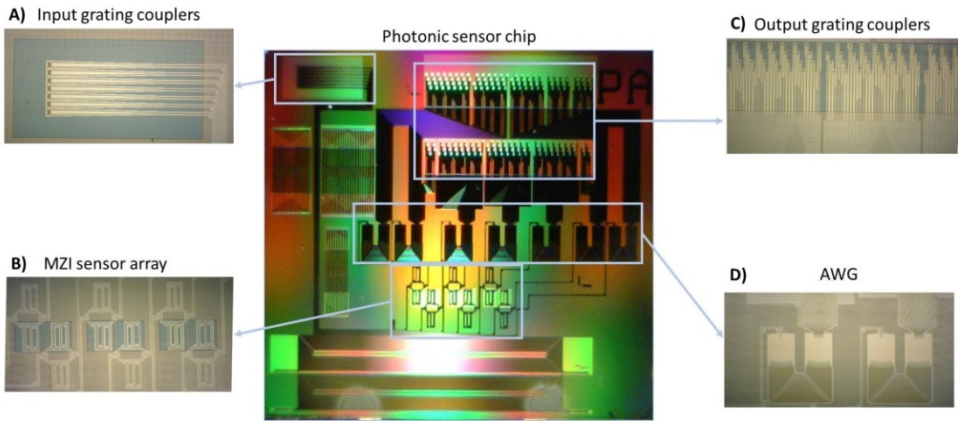

Figure 2.0.5. (A) Input grating couplers. **(B)** Six MZI sensor contained in the photonic sensor chip. **(C)** Output grating couplers. **(D)** Arrayed Waveguide Grating (AWG).

2.2. Disposable microfluidic cartridge

The **microfluidic cartridge** employed in this thesis was designed and manufactured by microfluidic ChipShop (Germany), a partner participating in the EU Project POCKET. The final design adopted is shown in **Figure 2.6**. The cartridge has a microscope slide dimension (25.5 x 75.5 mm) and was made of cyclic olefin copolymer (COC) via milling. COC is an amorphous thermoplastic synthetic copolymer which possesses unique properties compared with conventional polymers (e.g., poly(dimethylsiloxane) (PDMS), poly(methyl methacrylate) (PMMA), and polycarbonate (PC)) used to fabricate microfluidic devices.[113,114] The main advantages conferred by this novel material are resistance to hydrolysis by acid, bases, and most organic polar solvents, low water absorption (<0.01%), high heat resistance, increased transparency, and low autofluorescence.[113,115,116] Furthermore, it allows cost-effective large-scale microfluidic cartridge production, cheap enough to be disposable, and thus, a promising material to be used for POC biosensor systems.[114]

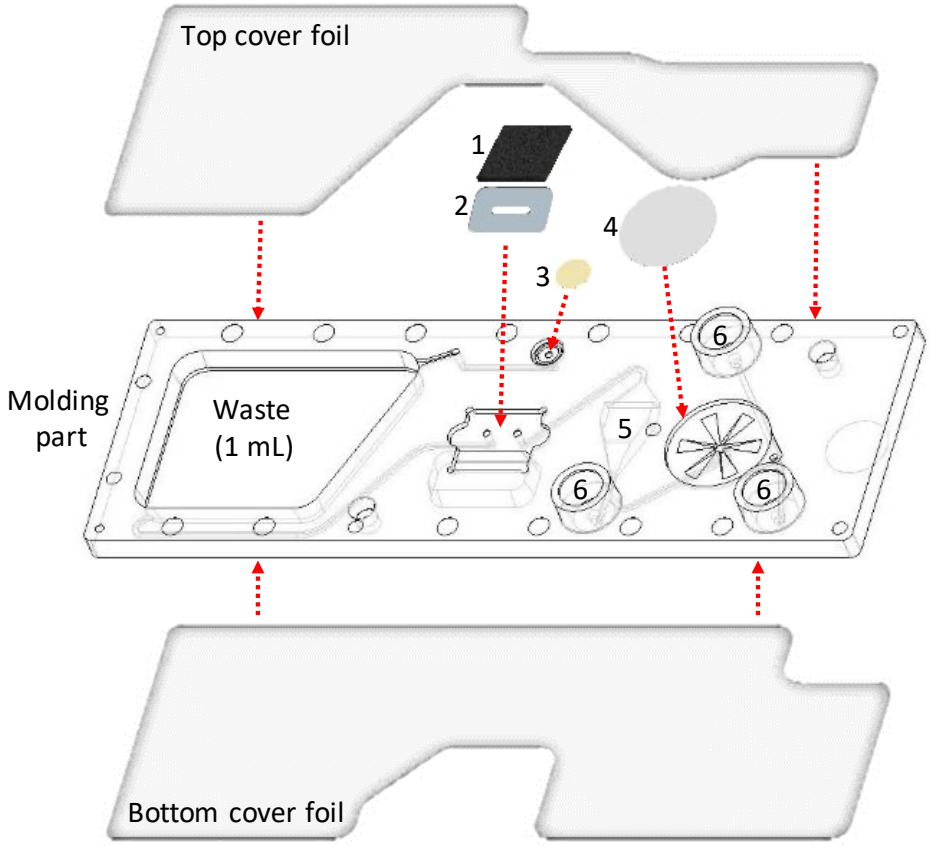

Figure 2.0.6. Scheme of the microfluidic cartridge integrated with the photonic sensor chip. (1) Photonic sensor chip, (2) Adhesive tape, (3) venting membrane, (4) urine filter (optional), (5) bubble trap, and (6) female Luer interface.

The photonic sensor chip is incorporated in the cartridge using a double adhesive tape to form the channel and deliver the sample onto the MZI sensing arms. On the other hand, the input and output grating couplers are left exposed for easy optical access (see **Figure 2.7**). The fluidic attachment includes three female Luer interfaces to facilitate the connection with standard 2 mL syringes, which will be carrying the sample and the required assay reagents (see **Figure 2.8**). An air bubble trap is incorporated to avoid undesired air bubbles on the photonic sensor chip. Additionally, a membrane (5 µm pore size) can be included on-cartridge for a previous filtering of the biofluid samples when required.

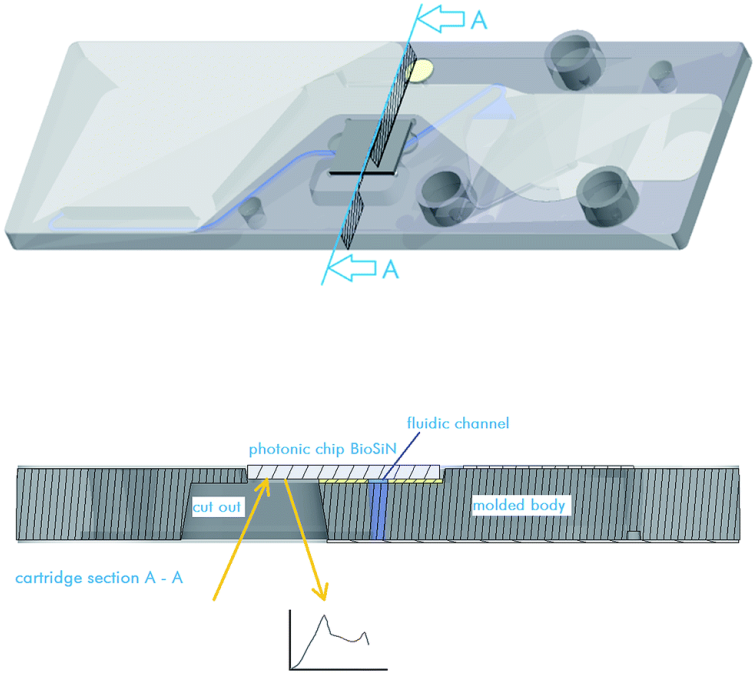

Figure 2.0.7. Cross section through the microfluidic cartridge along section A-A (indicated in the top figure)

For waste handling, a reservoir of 1 mL volume is included at the end of the fluidic path to prevent any risk of contamination due to the manipulation, the system, and the environment. This reservoir is followed by a venting membrane that allows air to escape from the microfluidic cartridge when the reservoir fills up.

Figure 2.0.8. Microfluidic cartridge with three-syringe.

2.3. Prototype instrument

The complete **prototype instrument** incorporates an optical readout, the pumping unit interfacing with the cartridge, and a touch computer with user interface (details shown in **Figure 2.9A**). The instrument size (22 x 22 x 49.30 cm) is determined by the vertically oriented syringe approach selected for the microfluidic cartridge (see **Figure 2.9B**).

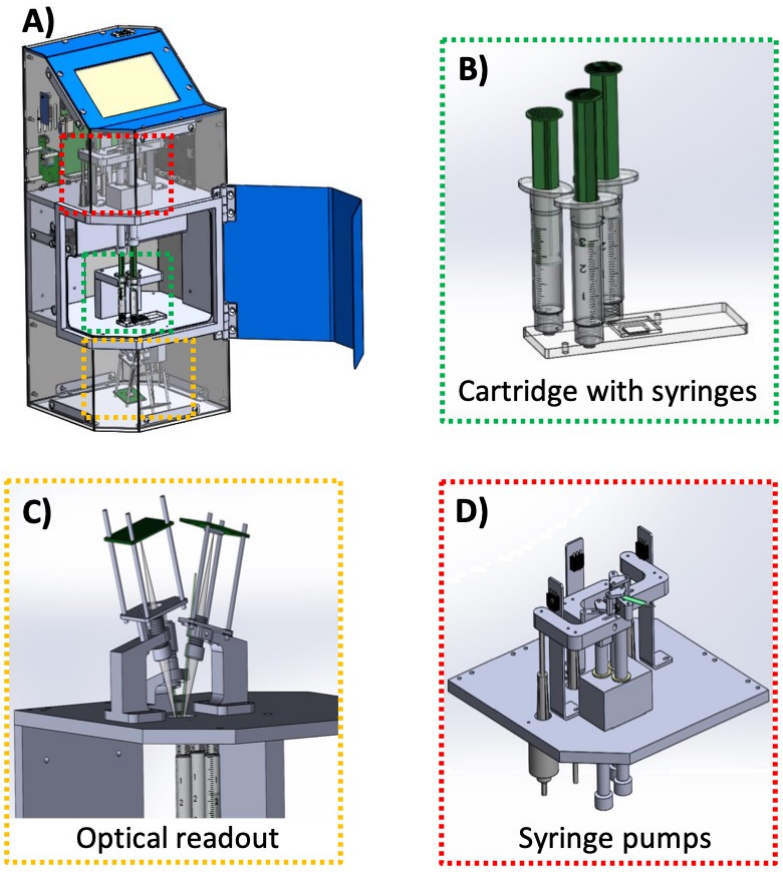

Figure 2.0.9. (A) General overview of the prototype instrument, **(B)** microfluidic cartridge with three-syringes, **(C)** optical readout, and **(D)** syringe pumps.

The optical readout unit, as shown in **Figure 2.9C**, is mounted upside down in the bottom part of the prototype instrument and contains the

SLED light source and the photodetector. A commercial SLED (SLD-340-HP-850; λ = 850 nm and Power = 30 mW; Superlum (Ireland)) is used as a light source, and a camera system is employed as a photodetector, which consists of an off-the-shelf CMOS image (UI-1242LE; Resolution = 1280 x 1024, Optical area = 6.784 x 5.427 mm, Pixel size = 5.30 μm; IDS Imaging Development Systems GmbH (Germany)) and a lens system with a magnification factor of 1.5x.

The biosensor platform requires controlled pumping of the sample and the buffers through the microfluidic channels, and for this reason, three syringe pumps are integrated into the prototype instrument (**Figure 2.9D**). Each pump has a stepper motor directly driving a piston up and down, including a pressure sensor to detect mechanical contact between the piston head and the syringe plunger. From this position, the cylinder pushes the plunger of the syringe downwards, transferring the sample from the syringe to the microfluidic cartridge. This movement takes into account the pump time and the speed previously defined by the pump controller software. In order to check that every syringe contains enough liquid to finish the required pump program, a verification step is added to each measurement.

A potential failure risk in the system is the effect of air bubbles on the photonic sensor readout. The readout system contains an integrated camera that takes real-time images of the microfluidic channel where the photonic sensor chip is located (**Figure 2.10**), allowing the monitoring of air bubbles movement. **Figure 2.10A** shows a photograph of the microfluidic channel taken with the integrated camera. An air bubble is visible in **Figure 2.10B**. This information is used only for quality control purposes to inform the user about possible interfering air bubbles.

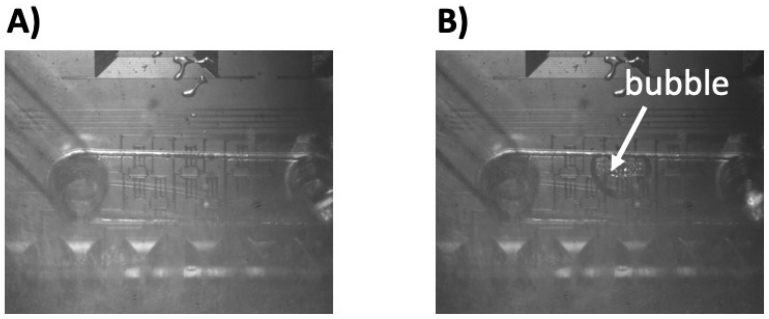

Figure 2.0.10. Real-time image from the air bubble camera **(A)** without and **(B)** with a bubble in the microfluidic channel.

A full Windows computer was integrated, including a high-resolution touch screen with a graphical user interface, to operate with this prototype instrument on-site. The custom-made software was developed in LabVIEW 2011 (National Instruments, US) by Trinean NV (Belgium), another of the partners of the EU project, including the algorithm for the wavelength shift calculation developed by Ghent University. The starting point for the algorithm is the image of the light spots emitted by the photonic sensor chip (already shown in **Figure 2.2A**).

The integrated user interface enables automatic light coupling and light spot detection, pump speed control, and injection time of each syringe. Furthermore, it contains an option to visualise the sensorgram of each biosensor in real-time during the evaluations, giving immediate feedback to the user. In addition, the system design includes a validation approach that allows users to check the instrument operation and quality of the sensor readout, guaranteeing the test reliability.

Figure 2.11 shows a real photograph of all the **POC biosensor platform** elements previously described in this Chapter. It should be noted that all the components were selected to be low-cost and user-friendly, making feasible its use as a whole POC biosensor platform, especially in low- and middle-income countries.

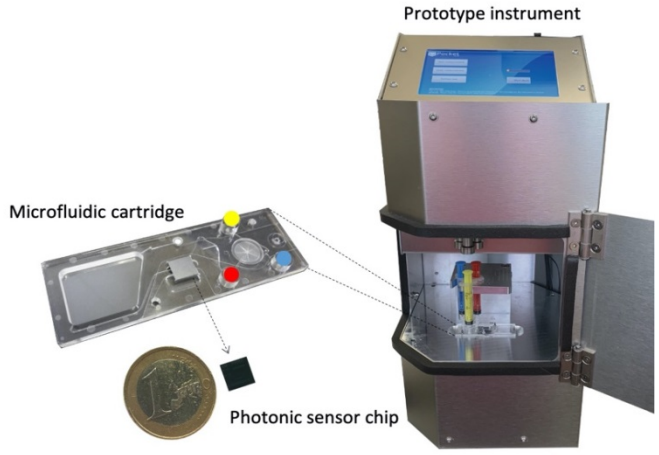

Figure 2.0.11. Prototype POC biosensor instrument (right) and main components of the cartridge (photonic sensor chip and microfluidics cartridge) for the analysis of human urine samples.

As a previous step before the evaluation of the complete POC biosensor instrument, we decided to add an external in-flow system to perform a complete analytical characterisation of the biosensor at the laboratory level due to the limitations of the microfluidic cartridge waste reservoir (capacity of 1 mL) and the three-syringe configuration (**Figure 2.8**). **Figure 2.12** shows the elements employed for this in-flow system: (i) a syringe pump (New Era, US) with adjustable pumping flow rate usually in the range 5 – 30 µL/min; (ii) a two-position valve (VICI, US) which allows sequential loading of the sample loop and injection into the microfluidic sensing cartridge at constant flow; and (iii) three Teflon caps which provide connections to the microfluidic cartridge female Luer interfaces. One of these caps allows the flow of the sample in the microfluidic sensing cartridge, and the other two form a vacuum and avoid air bubbles. The evaluation of the POC biosensor instrument of this Thesis was performed using both configurations, the in-flow, and the three-syringe configuration.

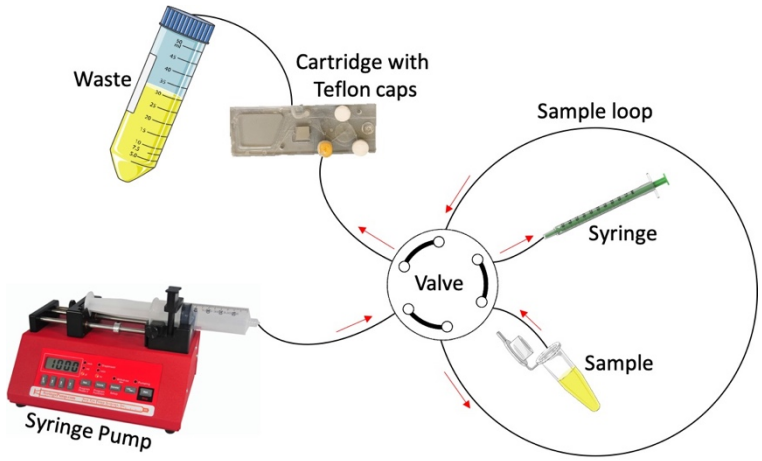

Figure 2.0.12. Detailed scheme of the in-flow delivery system employed.

2.4. Optical characterisation

As explained in the Introduction section, the bulk sensitivity evaluation is a standard analytical parameter employed to compare the performance between different sensor types regardless of surface biofunctionalisation. This estimation was carried out in the photonic sensor chip by evaluating the response to refractive index changes of the medium in contact with the sensing MZI arm. These changes are induced by using solutions that do not chemically modify the photonic sensor chip surface, such as low hydrochloric acid (HCl), glycerol, or phosphate buffer saline (PBS) concentrations.

In order to evaluate the photonic sensor performance, six different PBS solutions (5, 10, 25, 50, 75, and 100 mM) were sequentially injected, providing small refractive index changes compared with the milli-Q water employed as running buffer. The sensor signal measured in wavelength shift is shown in **Table 2.1** *versus* their respective refractive index difference change with respect to water (Δn). The PBS dilution refractive indexes were determined with a digital refractometer (Rudolph Research Analytical, US).

Table 2.1. Refractive index change induced by a set of PBS solutions and corresponding wavelength shift evaluated on a photonic sensor chip.

PBS concentrations (mM)	Δn (RIU)	Wavelength Shift (nm)
5	1.00×10^{-3}	1.76 ± 0.17
10	1.70×10^{-3}	3.57 ± 0.17
25	4.50×10^{-3}	8.58 ± 0.37
50	8.20×10^{-3}	16.45 ± 0.74
75	1.21×10^{-2}	23.85 ± 0.65
100	1.56×10^{-2}	31.28 ± 1.06

An example of a real-time sensorgram, where the six MZI sensors contained in the same photonic sensor chip are responding simultaneously to increasing PBS concentrations, is shown in **Figure 2.13A**. In this figure, a reference sensor (red line) can be observed with a distinct origin compared with the change in the other six sensors. As explained previously, it is a good evaluation of the drift on the SLED spectrum with the transmission spectrum of the input and output grating couplers; therefore, it is useful to compensate for this effect in the software.

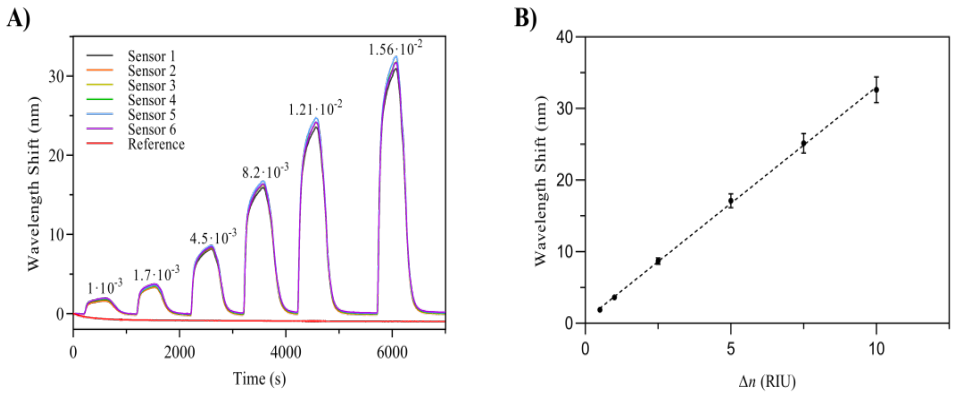

Figure 2.0.13. Calibration curve of the photonic sensor chip. **(A)** Real-time sensorgram by flowing different solutions of PBS with increasing refractive indices. The top of each bulk change specifies the Δn that is evaluated ($n_{[PBS]} - n_{H2O}$). **(B)** Calibration curve for the

evaluation of the photonic sensor chip sensitivity. Solid line corresponds to linear fitting. All data represents the mean ± SD between sensors.

A linear dependence is observed (coefficient of determination (R^2) = 0.99, **Figure 2.13B**) when plotting the wavelength shift variation *versus* the refractive index change (Δn). Then, the LOD (Δn_{min}) is estimated according to the following equation:

$$\text{LOD} = \frac{3\sigma}{S_{bulk}}, \quad \textbf{(3.1)}$$

where σ is the standard deviation of a blank signal and S_{bulk} is the slope of the linear regression.

The evaluation shown in **Figure 2.13** had an experimental sensitivity of $S_{bulk} = 3 \times 10^4$ RIU/nm and a system noise of 0.003 nm, resulting in a LOD of 3×10^{-6} RIU. This evaluation was repeated using different photonic sensor chips, and it resulted in the same LOD $(3.25 \pm 0.58) \times 10^{-6}$ RIU.

A one-way analysis of variance (ANOVA) was conducted to compare the obtained LOD. There were no statistically significant differences (p-value > 0.999) between sensor chips contained in the same photonic sensor chip and between different photonic sensor chips. These results are in the range of the reported MZI biosensors,[117] demonstrating the excellent performance and reproducibility of the fabricated photonic sensor chips and the POC platform.

Chapter 3
Sensor surface biofunctionalisation

The following Chapter deals with the diverse methodologies to immobilise bioreceptors on the sensor surface. The Chapter is divided into two sections devoted to each of the proposed methodologies, covalent and non-covalent. After a rigorous study, the optimal biofunctionalisation strategy was selected to immobilise the bioreceptors in the photonic MZI sensors. This strategy will be exploit further in the next Chapters for the detection of the Tuberculosis biomarkers.

3. Sensor surface biofunctionalisation

3.1. Introduction

The final sensitivity of a biosensor platform is directly related to the transducer sensing principle as well as the properties of the immobilised biological receptor and the surface functionalisation chemistry employed. Reliable functionalisation associated with the attachment of biological receptors to the sensor surface is the most crucial step for achieving high-performance, selective and sensitive biosensors able to analyse human bodily fluids (i.e., urine, plasma, and sputum) directly without sample pre-treatment. The key factors to take into account for an optimum biosensor functionalisation include:

(i) proper packing density and orientation of the bioreceptors over the sensor surface while leaving the receptor with active sites accessible for the analyte recognition

(ii) preservation of the bioreceptor conformation and functionality during the analysis

(iii) avoidance of undesired adsorptions of other molecules from the biological fluids that can hinder the analyte recognition.[118,119]

A wide variety of biofunctionalisation strategies have been developed to attach biomolecules to the sensor surface, aiming to provide the best analytical performance. Moreover, many research lines are still being undertaken at international level to investigate and improve this specific area.

Physical adsorption is the most straightforward strategy, consisting of the biological receptor direct adsorption onto the sensor surface *via* intermolecular forces, such as electrostatic and hydrophobic interactions, ionic and hydrogen bonds, van der Waals forces, or a combination of them (**Figure 3.1A**).[118–120] The intermolecular forces in the interaction will mainly rely on the biomolecule and the surface involved, being highly

sensitive to environmental changes such as pH, ionic strength, and temperature.[119–121] Bioreceptors can be immobilised through multiple binding sites to minimise repulsive interactions with the surface and with previously adsorbed biomolecules. Therefore, the resulting biofunctionalised surface will be heterogeneous with randomly oriented biomolecules, and with the possibility of protein activity reduction and affinity loss for their specific analyte. Moreover, additional steps for blocking the uncoated surface should be performed after receptor immobilisation to avoid non-specific adsorptions.[119]

An alternative strategy that has been used to avoid direct contact of the biological receptor with the sensor surface, while keeping its natural conformation and preventing denaturation, is **physical entrapment** (**Figure 3.1B**). Based on a simple one-step method, a uniform polymer matrix is formed, which allows the enclosure of the biomolecules. The most common polymers employed are polyaniline, dextran-based polymers, polythiophene and polypyrrole. This strategy does not involve any bioreceptor modification during immobilisation, guaranteeing its biological activity, and providing a better environment for prolonged storage. However, it can suffer from critical diffusion and limiting mass transport that make analyte accessibility to the bioreceptor difficult due to the polymer layer.[122]

To solve some drawbacks of the above strategies, another route based on **bioaffinity interaction** exploits specific binding molecules existing in nature, such as the biotin-avidin system (**Figure 3.1C**). This strategy is based on the sensor surface coverage with streptavidin by physical adsorption, and the subsequent addition of the biotinylated bioreceptor. This approach offers a homogeneous and oriented bioreceptor immobilisation, leaving better analyte accessibility to the binding sites.[119] The main drawbacks of this strategy are the need to modify the bioreceptors for attachment (e.g., biotinylation), and the dependence of an intermediate binding molecule between the surface and the bioreceptors.[120,123]

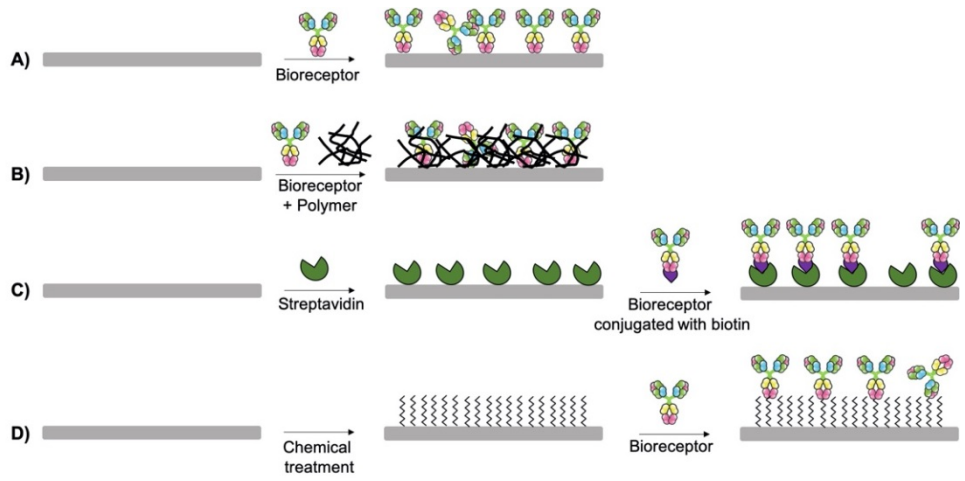

Figure 3.1. Main types of biofunctionalisation strategies to immobilise bioreceptors to a solid surface: **(A)** physical adsorption, **(B)** physical entrapment, **(C)** bioaffinity interaction, and **(D)** covalent binding.

Due to the above-described limitations, biofunctionalisation is usually done *via* **covalent binding** through chemical functional groups placed on the sensor surface and exposed functional groups on the bioreceptor, generating an irreversible bond (**Figure 3.1D**).[124] Covalent immobilisation provides the best longevity, reproducibility, and sensitivity. These advantages added to the enormous variety of functional groups (i.e., $–NH_2$, –COOH, –SH, $–N_3$), convert this strategy in the most widely used in biosensing applications. In this strategy, a previous chemical activation is required to generate enough functional groups on the sensor surface. In addition, a covalent bond can be formed on active sites of bioreceptors, reducing their biological activity.

A study evaluating three different biofunctionalisation strategies for the immobilisation of antibodies over the photonic sensor surface was performed.

3.2. Materials and methods

3.2.1. Chemical reagents and buffer composition

Organic solvents (acetone, ethanol, 2-propanol, methanol (MeOH), and ethanol absolute) and hydrochloric acid (HCl, 37%) were purchased from Panreac (Spain). Reagents for biofunctionalisation (N,N-dimethylformamide anhydrous (DMF), pyridine anhydrous, p-phenylene diisothiocynate (PDITC), 3-Aminopropyltriethoxy silane (APTES) and N-N-diisopropylethylamine (DIPEA), tris hydrochloride (Tris-HCl), dimethyl sulfoxide (DMSO)), sodium dodecyl sulfate (SDS), and all reagents used for buffer preparation were provided by Sigma-Aldrich (Germany). The 11-Azidoundecyltrimethoxysilane (N_3-silane) was purchased from abcr GmbH (Germany). Crosslinking molecule dibenzylcyclooctyne polyethylene glycol N-hydroccinimide ester (DBCO-PEG_4-NHS) was purchased from Jena Bioscience (Germany). Azide-PEG-Thiol (N_3-PEG-SH, 2000 Da) was supplied by Nanocs (US). The buffers employed were phosphate buffer saline (PBS: 10 mM Na_2HPO_4, 1.8 mM KH_2PO_4, 2.7 mM KCl, and 137 mM NaCl, pH 7.4), and 0.1 M carbonate buffer (Na_2CO_3, pH 9.5) Milli-Q water was employed for buffer preparation.

3.2.2. Biological compounds

Bovine Serum Albumin (BSA) was purchased from Sigma-Aldrich (Germany). Human C-Reactive Protein (CRP) and monoclonal IgG antibody against CRP C7 (anti-CRP) were acquired from BBI Solutions (UK) and HyTest (Finland), respectively. Recombinant protein Ag85B was provided by LIONEX GmbH (Germany).

3.2.3. Si_3N_4 surface biofunctionalisation

3.2.3.1. Vapour-phase silanisation with N_3-silane

Vapour-phase silanisation was performed by IMEC (Belgium) using a home-built stainless-steel vacuum chamber large enough to hold a 200 mm wafer. The entire vacuum chamber was heated in an oven for one

hour at 145°C or 24 h at 60°C with the required amount of N_3-silane (100 µL for 1 h and 200 µL for longer deposition times) and the pressure was lowered to 25 mbar. Then, before unloading the samples, the chamber was purged three times with N_2.

After vapour-phase functionalisation, the N_3-modified sensor surface was incorporated onto the microfluidic cartridge and placed on the POC platform for *in-situ* immobilisation of anti-CRP through covalent binding of the azide groups ($–N_3$) introduced on the sensor surface using a crosslinker. Azide groups were reacted with a solution of DBCO-PEG_4-NHS (2 mM in ethanol absolute/water 1:1 (v/v)) flowed over the sensor surface at 20 µL/min. Subsequently, a solution of anti-CRP (50 µg/mL in PBS) was injected at a flow rate of 10 µL/min. The remaining unreacted groups were deactivated with a Tris-HCl solution (100 mM) at 20 µL/min. Milli-Q water was used as the running buffer during the immobilisation step and was then switched to PBS.

3.2.3.2. In-flow silanisation with APTES

After placing the microfluidic sensor cartridge in the POC platform, a layer of active silanol groups was generated by flowing a solution of MeOH:HCl 1:1 (v/v) over the sensor surface. Immediately, a 1% APTES solution (v/v) with 0.3% DIPEA (v/v) prepared in absolute ethanol was injected. The amine groups were activated with 20 mM PDITC in a solution of 10% of pyridine (v/v) and diluted in DMF. Finally, a solution of anti-CRP (50 µg/mL in Na_2CO_3 buffer) was covalently attached to the sensor chip. A constant flow rate of 4 µL/min was employed during the whole procedure. Milli-Q water was used as the running buffer during the immobilisation step and was then switched to PBS.

3.2.4. Physical adsorption

A solution of anti-CRP (50 µg/mL in PBS) was immobilised by physical adsorption onto the photonic sensor chip surface, followed by a blocking step with 10 mg/mL of BSA to avoid non-specific adsorptions.

Milli-Q water was used as the running buffer during the immobilisation step at a flow rate of 10 µL/min and was then switched to PBS.

3.2.5. SPR platform and gold surface biofunctionalisation

3.2.5.1. SPR platform

The plasmonic biosensor is a homemade-designed and fabricated platform, incorporating the optical setup, the biosensor chip, and the microfluidic system. Briefly, a gold sensor chip is held between a trapezoidal prism and a custom-made flow cell. The flow cell is connected to a microfluidics system consisting of a syringe pump (New Era, US) with adjustable flow rate, and a two-position valve (VICI, US) which allows sequential loading of the sample loop and injection into the flow cell. The sensor surface is illuminated using a collimated halogen light source (Thorlabs, US) set in transverse-magnetic (TM) polarisation mode at a fixed incidence angle of 70°. The reflected light is collected by a fiber-coupled to a CCD spectrometer (Ocean Optics, US), which is controlled by an in-house software program that allows the tracking of the resonance peak ($\Delta\lambda$) in real-time. Biological interactions occurring in the gold sensor surface generate variations of the refractive index (RI) and are directly related to a mass change.

3.2.5.2. Gold sensor chip fabrication

Glass substrates purchased from Thermo Scientific (US) were cleaned by scrubbing their surface with SDS 0.5 M and successively rinsing with HCl 0.1 M, milli-Q water, and 2-propanol. After drying with N_2 gas, glass substrates were placed in O_2 plasma (Diener Electronic GmbH, Germany) for 1 minute to increase the hydrophilicity of their surface. Once the cleaning process was completed, glass surfaces were coated using electron-beam deposition with 1 nm of titanium (Ti) and 49 nm of gold (Au).

3.2.5.3. N_3-PEG-SH surface functionalisation

Gold sensor chips were cleaned by consecutive heating and one-minute sonication cycles in acetone, ethanol, and milli-Q water. The sensor chips were then dried with N_2 gas, and the sensor surface was activated by using a UV/O_3 generator (BioForce Nonosciences, US) for 20 min. Finally, the sensor chips were rinsed with ethanol, dried with N_2 flow, and immediately immersed overnight at room temperature in an N_3-PEG-SH (1 M) solution diluted in absolute ethanol.

3.2.5.4. Antibody-crosslinker conjugation

Antibodies against CRP (50 µg/mL) were diluted in PBS. A 10 mM of DBCO-PEG_4-NHS solution in DMSO was immediately added to the antibody solution to conjugate the antibody amino group with the crosslinker NHS ester. The reaction was incubated on ice for 2 hours or overnight. The reaction was stopped by adding Tris-HCl to a final concentration of 50 mM for 15 min on ice. The unreacted and excessive reagent was removed with a centrifugal filter (Amicon Ultra 30K device; Merck Millipore, US). The antibody-DBCO conjugation was finally resuspended in PBS and injected over an N_3-modified surface at 20 µL/min.

3.2.5.5. Direct immunoassay

Once the surface biofunctionalisation was carried out, a solution with 1 µg/mL of CRP diluted in PBS was injected into the system at 20 µL/min.

3.2.5.6. Data analysis

Data were analysed using OriginPro 8.0 (OriginLab, US) and Prism 8 (GraphPad Software, US).

3.3. Biofunctionalisation strategies: optimisation for the biosensor development

Integrated photonic sensor devices commonly use silicon-based materials due to their excellent optical properties, robustness, and easy fabrication process using conventional technologies. Additionally, these materials have excellent properties as an optimal sensing surface because of their high density and chemical inertness. These properties make them resistant to ion species, oxygen and moisture permeation as well as providing high stability at different temperatures, low surface roughness, and versatile chemical functionalisation.

As previously mentioned in Chapter 3, the photonic sensor chip has an open window in the sensing regions (MZI sensing arm) at the SiO_2 upper cladding, where the Si_3N_4 core layer is in contact with the external medium. The attachment of biomolecules to the Si_3N_4 sensing region is one of the most critical steps for developing a successful biosensor. For the development of our POC platform, we tested covalent immobilisation and physical adsorption among all the available immobilisation strategies to attach the specific antibodies onto the sensor surface. For the initial optimisation, we decided to focus on a widely studied model system, anti-CRP/CRP, and then translate these conditions to future applications for TB diagnosis.

3.3.1. Covalent biofunctionalisation

Covalent immobilisation is preferred in comparison with other procedures, as explained before. However, the covalent strategy is more complex, implying the previous modification of the Si_3N_4 surface by incorporating functional groups that can react with some chemical groups of the biomolecules.

Surface modification with organosilanes, especially alkylsilanes, has been extensively used due to their stability and rapid covalent linkage.[125]

Alkylsilane monolayers are formed in a silanisation process**,** which consists of a silane reaction with hydroxyl groups of the oxidised Si_3N_4 surface. The general structure of an alkylsilane presents a dual behaviour with an organic and inorganic part. The core consists of a silicon atom (Si) bonded to an organic functional group (R_n^-), which allows the covalent immobilisation of the biological receptor, while the inorganic part reacts with the hydroxyl-terminated silicon nitride surface providing the anchorage. This reaction involves two steps (**Figure 3.2**). In the first step, alkylsilanes establish hydrogen bonds with the free hydroxyl groups or with adsorbed water molecules on the surface. In the second step, covalent bonds are carried out by condensation and release of water molecules, leading to thermally and relatively chemically stable siloxane bonds (Si–O–Si). The presence of water molecules has a catalytic effect and should be controlled in order to ensure reproducibility.

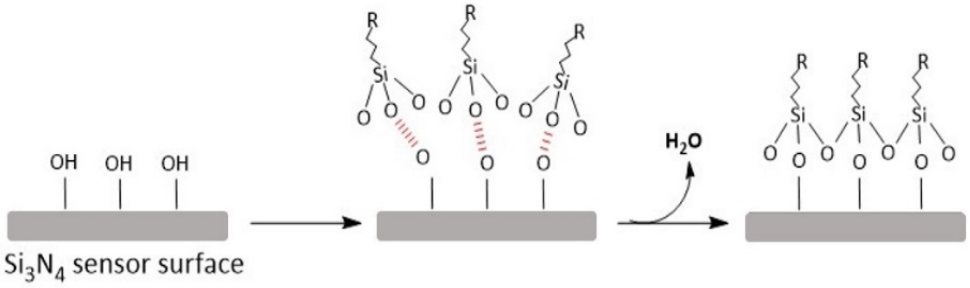

Figure 3.2. Scheme of the reaction of an organosilane with silicon-based surfaces.

In general, the silanisation process can be performed in liquid-phase or vapour-phase deposition. **Liquid-phase silanisation** is widely established and reported in the literature.[126,127] However, uncontrolled polymerisation and multilayer formation are some of the main drawbacks due to their high tendency to absorb water and humidity from the environment.[128–130] The use of vacuum equipment in **vapour-phase silanisation** allows better control in the environmental conditions, resulting in better reproducibility and quality of the silane layer than the solvent phase.[131] Furthermore, vapour-phase silanisation can be easily

used at wafer-scale, significantly reducing chemical reagents and production costs.

The most common organosilanes employed for liquid-phase silanisation include 3-aminopropyltriethoxy silane (APTES, with an amino-ended surface (–NH2)),[109,132] carboxyethylsilanetriol sodium salt (CTES, with a carboxylic-ended surface (–COOH)),[133] and (3-mercaptopropyl)trimethoxysilane (MPTMS, with a thiol-ended surface (–SH)).[134] However, only APTES and MPTMS are suitable for vapour-phase deposition.

The choice of silane and the silanisation conditions are relevant parameters to control for the subsequent antibody immobilisation at the sensor surface. Therefore, we evaluated vapour-phase and solvent-phase silanisations for the covalent attachment of antibodies.

3.3.1.1. Vapour-phase silanisation of N_3-Silane

A vapour-phase silanisation process was developed by IMEC (Belgium), enabling silane coating directly at full-wafer scale and facilitating cost-effective mass production.[131,135] During vapour-phase silanisation, high temperature and low vacuum pressure are used to volatilise the silane molecules in an enclosed chamber, allowing them to be transported and reacted with all the silicon-wafer area. Consequently, only silanes with suitable boiling points and with sufficient thermal stability can be used in this approach. From the different organosilanes that are desirable for vapour-phase deposition, 11-Azidoundecyltrimethoxysilane (**N_3-silane**) is an ideal candidate, as it provides a terminal azide group (–N_3) that can be used for antibody immobilisation. Moreover, N_3-silane gives good uniformity, wafer-to-wafer reproducibility, and the coating can be preserved for several months.[135] Having several-month stability was crucial for the POC platform development because silanised sensor chips had to be first shipped from IMEC to microfluidic ChipShop (Germany) for the

microfluidic cartridge enclosing, and then sent to ICN2 for antibody immobilisation.

In this scenario, the reaction between an azide and an alkyne rapidly forms a covalent bond. This reaction is known as **click chemistry**. Since proposed in 2001 by Sharpless et al.,[136] it has been extensively used to synthesise a variety of conjugates in drug discovery,[137,138] bioscience,[139,140] and material science.[141] The main features of click chemistry are high efficiency, selectivity, and fast kinetics for coupling molecules under mild conditions in aqueous solution. Click chemistry reactions can be categorised into two separate groups: copper (I)-catalysed (CuAAC) and strain-promoted (SPAAC) reactions. CuAAC reactions rely on the presence of copper ions; thus, they are not suitable to use with biological molecules as they can be denaturalised.[142,143] To avoid this issue, SPAAC reactions efficiently proceed without metal catalysis, but they need to employ a cyclooctyne derivative, such as dibenzocyclooctyne (DBCO) or dibenzocyclooctyne (DIBO), among others.[144–147] Therefore, copper-free click chemistry is the best-reported option to immobilise antibodies when there is an azide end group in the sensor surface (see **Figure 3.3**).

DBCO reacts specifically and efficiently with the azide ending groups on the sensor surface, resulting in a stable triazole linkage. For this reason, we employed a commercial DBCO-PEG_4-NHS ester as a crosslinker, which allows the formation of triazole linkage with the sensor surface, whereas the incorporation of the NHS group forms a stable amide bond with primary amines on the N-terminal or side chain lysine residues of the antibodies (**Figure 3.3**). The four-polyethylene glycol (PEG) spacer molecules enhance solubility in water and general organic solvents (i.e., DMSO and DMF). Furthermore, it reduces non-specific adsorptions from unspecific components in biological fluid samples.

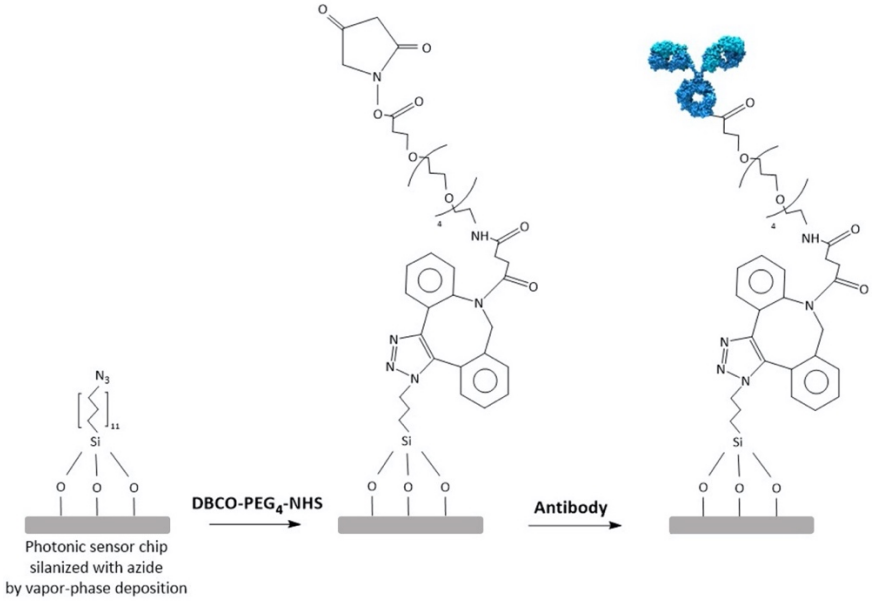

Figure 3.3. Scheme of the biofunctionalisation strategy using copper-free click chemistry in sensor chips previously silanised with N_3-silane at IMEC.

In these experiments, the microfluidic cartridges with N_3-silanised sensor chips were directly placed on the POC platform and an in-flow immobilisation of anti-CRP (50 μg/mL) was performed using 2 mM of DBCO-PEG$_4$-NHS. Antibody immobilisation was monitored in real-time, as can be observed in **Figure 3.4**. The triazole bond formation can be observed with the flow of DBCO-PEG$_4$-NHS, obtaining a sensor response of 8.46 ± 0.32 nm. However, it resulted in low anti-CRP immobilisation yields that led to a low density of bioreceptors immobilised on the sensor surface ($\Delta\lambda$ = 1.24 ± 0.30 nm). This phenomenon could be explained as a consequence of the NHS esters hydrolysis with the continuous flow of milli-Q water over the sensor surface, which generally constrains amide bond formation. Finally, a solution of 100 mM Tris-HCl was used to deactivate unreacted groups.

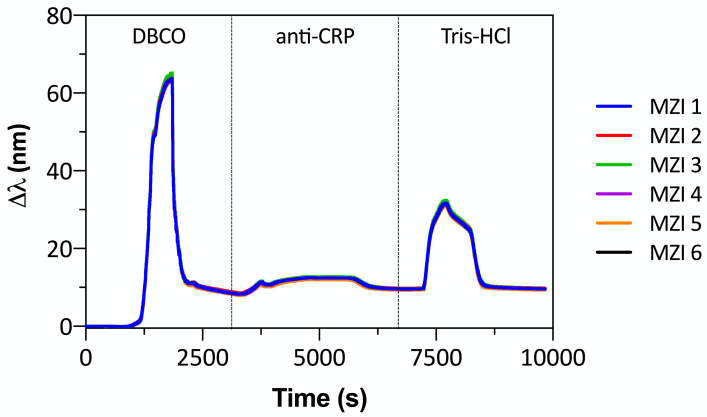

Figure 3.4. Real-time monitoring showing the click chemistry reaction between 2 mM of DBCO-PEG$_4$-NHS and N_3-coated sensor surface, the covalent attachment of anti-CRP (50 µg/mL in PBS) and the deactivation of unreacted groups with Tris-HCl (100 mM).

Then, 1 µg/mL of CRP was injected onto the biofunctionalised sensor surface. As expected, due to the low amount of covalently attached bioreceptors, the observed signal was very feeble ($\Delta\lambda$ = 0.37 ± 0.07 nm; **Figure 3.5A**) regarding the high analyte concentration employed. Despite the low sensitivity, this biorecognition signal was specific for CRP protein, as the injection of unspecific protein (1 µg/mL of Ag85B) resulted in a negligible signal (see **Figure 3.5B**).

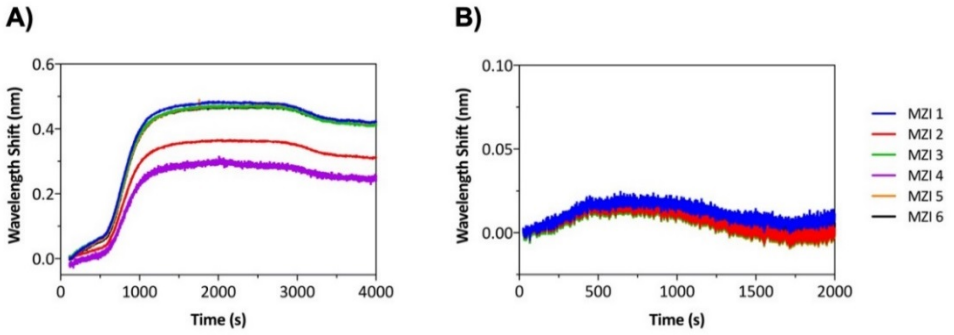

Figure 3.5. (A) Real-time sensorgram showing the detection of 1 µg/mL of CRP in PBS and **(B)** 1 µg/mL of Ag85B in PBS (control).

To test if NHS ester was hydrolysed during the in-flow immobilisation, an *ex-situ* conjugation between the antibody and DBCO-PEG$_4$-NHS was tested. Following previous reported studies and recommendations from the company that provided the DBCO-PEG$_4$-NHS, incubating both reagents for two hours on ice was enough to obtain a covalent bond between the anti-CRP and the DBCO-PEG$_4$-NHS. Unreacted DBCO-PEG4-NHS was removed with a centrifuge filter. The final solution with antibody-DBCO conjugate was immediately flowed over the sensor surface, reaching a 10-fold increased immobilisation signal ($\Delta\lambda$ = 18.64 ± 0.98 nm; see **Figure 3.6A**) compared with the previous strategy ($\Delta\lambda$ (DBCO + Antibody) = 9.71 ± 0.30 nm). Nevertheless, the problem with the target detection persisted, as can be observed in **Figure 3.6B**, and we were not able to detect higher concentrations of CRP (1 µg/mL tested).

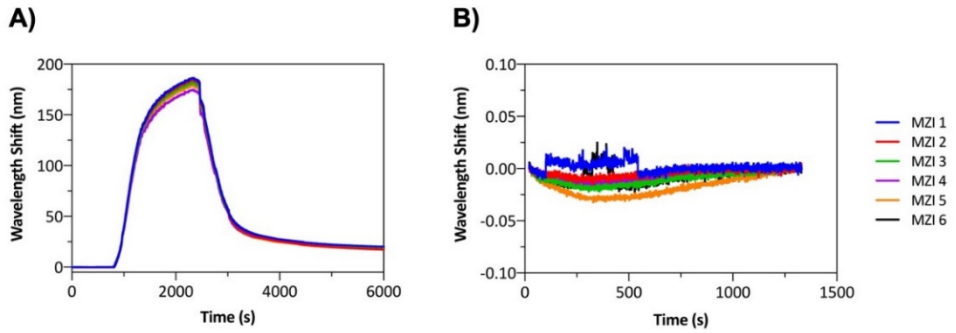

Figure 3.6. (A) Real-time sensorgram showing the immobilisation of antibody-DBCO conjugate in PBS and **(B)** the corresponding signal obtained for the detection of 1 µg/mL of CRP in buffer.

During the trials to improve and optimise both immobilisation strategies, we observed, in several experiment repetitions, that reproducibility was not good enough when using different microfluidic cartridges. The antibody immobilisation and the target were not reproducible, and when observed, the employed CRP concentration was too high.

In order to investigate if the origin of the problem was due to the silane vapour-phase deposition of the silane, we decided to employ our home-made SPR biosensor platform to assess the same copper-free click chemistry for the anti-CRP immobilisation (**Figure 3.3**). SPR sensors can be considered as a reference standard because they have been extensively reported in the biosensor field literature and our group account with a vast experience in the SPR biosensing field.[99,148,149] Moreover, complex silanisation processes are reduced to the well-studied and strong interactions between thiols groups and the gold sensor surface.[150,151] In order to study the immobilisation, gold sensor chips were coated overnight at room temperature with a molecule containing a thiol group in one end and an azide group in the other one. After the thiol assembly, the strategies tested before in the Si_3N_4 sensors chips were also examined with the plasmonic technology. However, the addition of DBCO-PEG_4-NHS and then the antibody in-flow resulted in an insignificant immobilisation yield ($\Delta\lambda$ = 0 nm). The best immobilisation signal was obtained after the injection of the conjugate antibody-DBCO ($\Delta\lambda$ = 2.04 nm; **Figure 3.7A**). In this case, a very weak signal was also observed for the detection of 1 μg/mL of CRP ($\Delta\lambda$ = 0.13 nm; **Figure 3.7B**). When using other biofunctionalisation protocols (not based on azide) for the anti-CRP/CRP system in the SPR biosensor, signals of around 1 nm for the detection of 1 μg/mL of CRP were reported.[152]

Therefore, we conclude that the azide chemistry was not working adequately enough, independently of the biosensor technology employed. We have not found the origin of such behaviour yet, because other reported papers successfully employed this chemistry to immobilise biomolecules onto solid surfaces.[131,135,153–155] In consequence, we decided to discard this strategy for the final development of the POC biosensor platform.

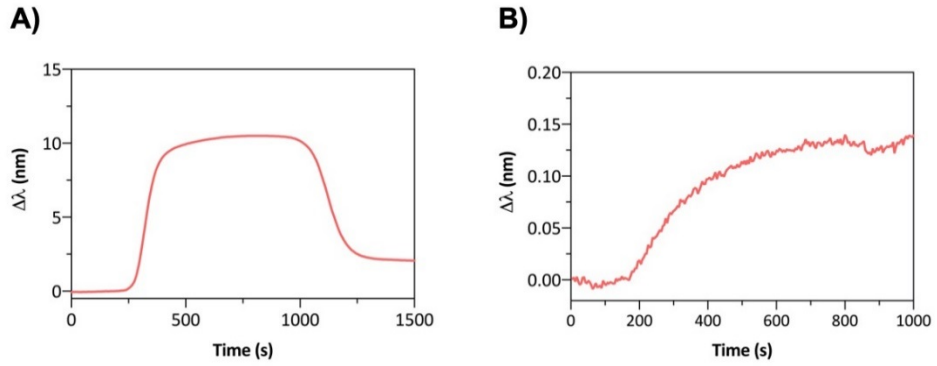

Figure 3.7. (A) Real-time sensorgram obtained in the SPR platform for the immobilisation of antibody-DBCO conjugate in PBS and **(B)** the signal obtained for the detection of 1 µg/mL of CRP in buffer.

3.3.1.2. In-flow APTES silanisation

One of the most widely used silanes for chemical functionalisation of silicon nitride surfaces is **APTES**.[156] This silane provides surfaces with amino groups (–NH_2), which can be employed for the covalent bonding of biomolecules through several crosslinkers, such as p-Phenylene diisothiocyanate (PDITC), bissulfosuccinimidyl suberate (BS3), glutaraldehyde, or succinic anhydride, among others.[125,157,158] PDITC has been extensively used in bioconjugation chemistry to activate amino groups,[159] and using this strategy low unspecific adsorption in real samples evaluations has already been demonstrated.[160] PDITC crosslinker carries two identical isothiocyanate (–NCS) groups that react with either amino groups incorporated during silanisation or primary amine groups from antibodies, forming a covalent thiourea bond (**Figure 3.8**).

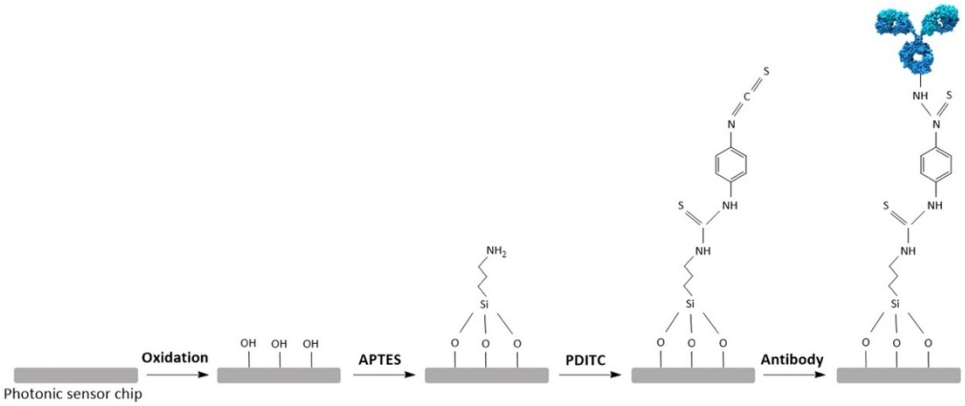

Figure 3.8. Scheme of the covalent antibody functionalisation using in-flow APTES silanisation and PDITC surface activation.

Taking advantage of the PDITC crosslinker, previously reported liquid-phase APTES silanisation under controlled conditions, involved the prior activation of the sensor surface by oxygen plasma in order to generate a layer of active hydroxyl groups. Additionally, subsequent immersion in 15% nitric acid (HNO_3) at 75°C for 25 min was required to reveal the silanol groups on the silicon nitrate surface (**Figure 3.8**).[109,161] However, this procedure could not be done because the photonic sensor chips were already integrated into the microfluidic cartridge. An alternative for solving this challenge was **in-flow silanisation**, monitoring all the steps in real-time with the POC platform. The polymer employed for the microfluidic cartridge production is highly resistant to acid solutions; thus, a 15% HNO_3 solution at room temperature was flowed over the sensor surface without damaging the microfluidics. However, when flowing the solution, the sensor signals became unusual, complicating the understanding of what was occurring at the sensor surface. Moreover, it seemed that the acid had damaged the sensor surface because, afterwards, it was not possible to work with this photonic sensor chip.

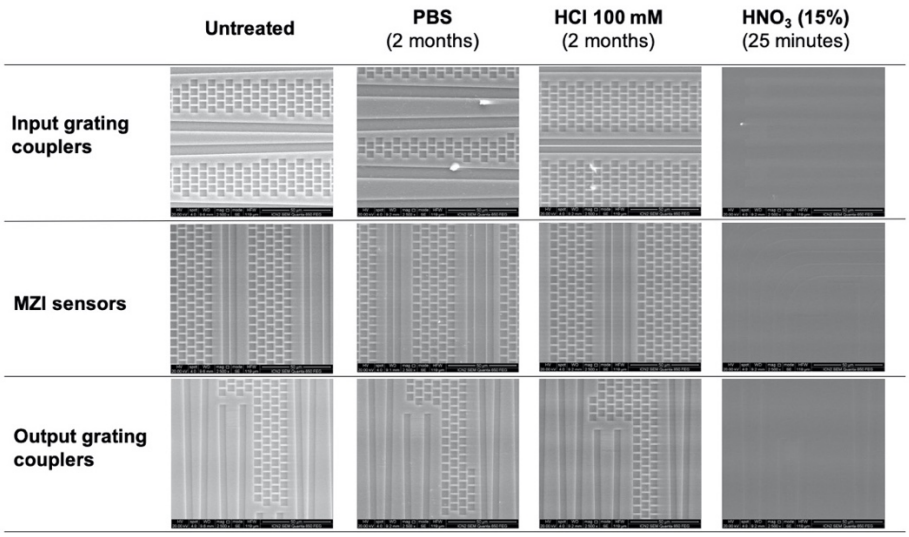

Figure 3.9. SEM image for different regions of the photonic sensor chips (input and output grating couplers, and MZI sensors) untreated and immersed in different solutions (PBS, HCl 100 mM and diluted HNO_3.

To discover the reasons for this failure, a stability study of the photonic sensor chips was carried out by submerging them in PBS and 100 mM HCl for two months, and in 15% HNO_3 for 25 min. After these times, chip surface evaluation was first performed using an optical microscope. Since we could not see any difference between the sensor chips, we decided to evaluate them with a Scanning Electron Microscope (SEM; Quanta 650 FEG). As can be observed in **Figure 3.9,** the most remarkable difference appears just when we used HNO_3, after which the **sensor structure disappears**. One of the possible reasons is that the photonic sensor chips were fabricated by plasma-enhanced chemical vapour deposition (PECVD), and the surface presented more porosity than the one obtained by low-pressure chemical vapour deposition (LPCVD), which is the preferred technique employed in the fabrication of the Si_3N_4 waveguides. However, IMEC cleanroom facilities do not produce LPCVD Si_3N_4, and therefore, it was not possible to shift to LPCVD technology.

As the photonic chips were not resistant to HNO_3, the layer of active hydroxyl groups on the silicon sensor surface was generated by flowing a

MeOH:HCl (1:1) solution.[162] Immediately after, we flowed 1% APTES solution with 0.3% DIPEA prepared in dry ethanol. **Figure 3.10A** shows this in-flow silanisation process, where it can be observed that APTES is covalently attached to the sensor surface. We do not know if this value is enough to obtain a homogenous layer, as there are no literature reports for comparision. **Figure 3.10B** shows the activation of silane amino groups through the injection of 20 mM PDITC, followed by the attachment of 50 µg/mL anti-CRP in Na_2CO_3 buffer at pH 9.5. This basic pH promotes the reaction with the –NCS group, reactivating antibody primary amines. In this case, the covalent immobilisation exhibited a sensor response of 8.65 ± 0.28 nm, significantly higher than those obtained previously with N_3-silane.

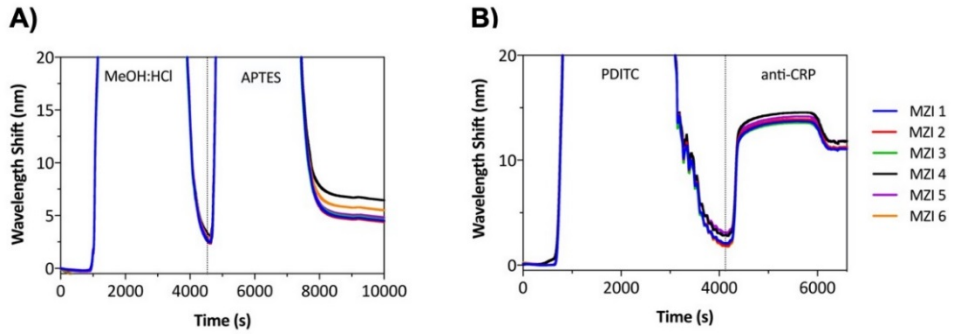

Figure 3.10. (A) Real-time monitoring for APTES in-flow silanisation starting with oxidation step (MeOH:HCl, 1:1) and the subsequent flow of 1% APTES. **(B)** Surface activation with PDITC crosslinker (20 mM) and the covalent immobilisation of 50 µg/mL of anti-CRP.

To finally determine the biofunctionalised sensor ability to recognise its antigen specifically, 1 µg/mL of unspecific protein (the recombinant protein Ag85B) was first flowed. As it can be observed in **Figure 3.11A**, this protein leads to a negligible sensor signal. On the other side, a clear signal (0.35 ± 0.06 nm) was obtained for the same concentration of the specific protein (CRP), as shown in **Figure 3.11B**. Therefore, this procedure represents promising preliminary results with an optimised protocol for in-flow silanisation based on *ex-situ* liquid-phase silanisation. However, if this APTES-PDITC protocol is finally selected for the final

POC platform, further optimisations are required to increase antibody immobilisation and the total immunoassay performance.

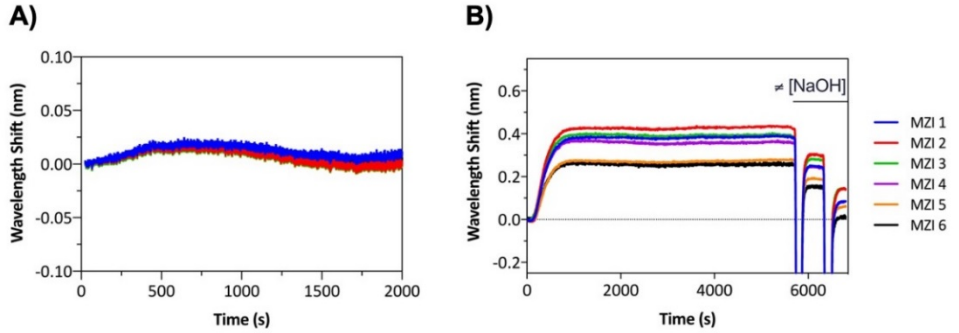

Figure 3.11. (A) Real-time sensorgram comparing the obtained signals for 1 µg/mL of Ag85B (control) and **(B)** 1 µg/mL of CRP including regeneration step with different pulses of NaOH 5 mM.

One of the advantages of covalent binding is the reusability of the biofunctionalised sensor surface several times. Sensor reusability will depend on the ability to disrupt the anti-CRP/CRP interaction entirely while maintaining the biorecognition layer intact. Surface regeneration can be achieved with changes in the pH of the media. In our case, different pulses of NaOH 5 mM were tested. It seems that NaOH 5 mM for 1 min was enough to accomplish the regeneration in MZI 6. As can be observed in **Figure 3.11B** (black line), the sensor signal returns to the baseline, indicating that interaction between the antibody and the protein was disrupted. However, the same effect was not observed for the other MZI sensors, where different regeneration effects were observed. As the sample flows simultaneously over the six MZI sensors, if we continue flowing NaOH over the sensor surface, the antibody could lose its functionality in those cases where regeneration was accomplished. Due to the microfluidic cartridge design, it is complicated to determine a solution to regenerate all MZI sensors simultaneously.

3.3.2. Non-covalent biofunctionalisation

3.3.2.1. Physical adsorption

The most-straightforward methodology to immobilise antibodies *via* electrostatic interactions is **physical adsorption**. The corresponding anti-CRP antibody (50 µg/mL) was first physically immobilised on the sensor surface, and then a blocking step of the free areas was done with 10 mg/mL of BSA to prevent non-specific adsorptions (**Figure 3.12**).

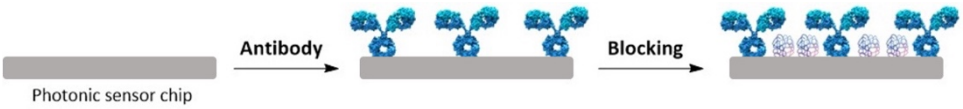

Figure 3.12. Scheme of the physical adsorption of the antibody and the blocking step.

The immobilisation monitoring in real-time is shown in **Figure 3.13**. The antibody adsorbed onto the sensor surface resulted in an immobilisation signal of 10.72 ± 0.43 nm, which clearly illustrates a high binding efficiency of the antibodies to the sensor surface.

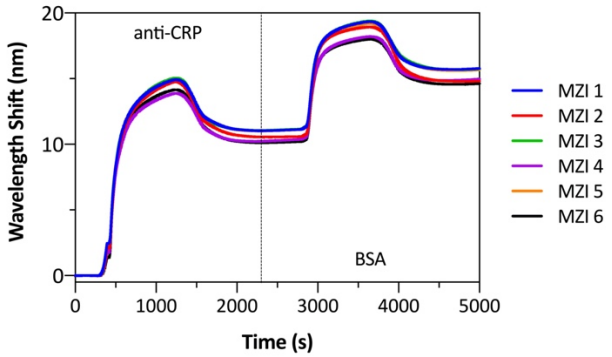

Figure 3.13. Physical adsorption of 50 µg/mL of anti-CRP and blocking step with BSA (10 mg/mL).

We firstly flowed 1 µg/mL of Ag85B protein (control) over the sensor surface due to the incompatibilities with regeneration strategies. As shown in **Figure 3.14A**, a slight sensor response of 0.03 ± 0.02 was obtained.

This signal can be considered as negligible as it could be associated with experimental noise.

Finally, when evaluating the response to 1 µg/mL of CRP, a clear signal was observed (0.79 ± 0.09 nm; **Figure 3.14B**). This was the best signal obtained for the antibody immobilisation and detection of CRP protein compared with previous biofunctionalisation procedures tested.

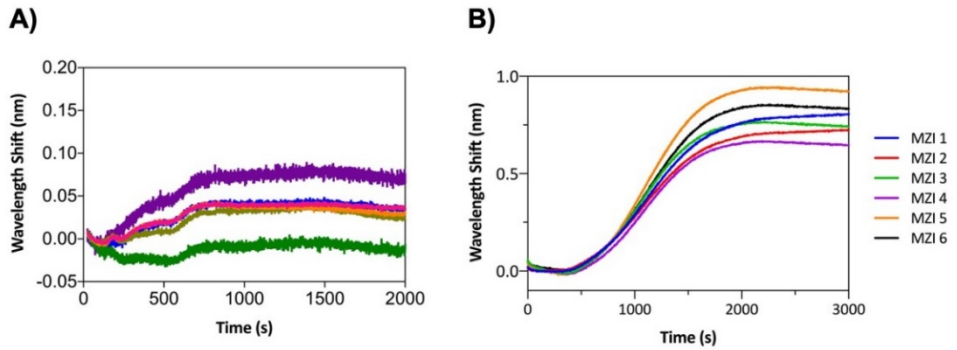

Figure 3.14. (A) Real-time sensorgram showing the obtained signals for 1 µg/mL of Ag85B (control) and **(B)** 1 µg/mL of CRP.

We are aware that physical adsorption is not the optimal immobilisation method of choice, due to the possibility of desorption of the biological receptors and the incompatibility with regeneration strategies. However, due to the regeneration incompatibilities observed with covalent binding through APTES-PDITC chemistry and the impossibility of moving to LPCVD silicon nitrate waveguides, there is no advantage of using covalent binding instead of physical adsorption. Therefore, physical adsorption was our preferred option as it is a simple and reliable methodology when we require demonstrating a proof-of-concept of the photonic sensor performance and the prototype instrument.

3.4. Conclusions

The selection of the most appropriate surface chemistry to attach a bioreceptor guaranteeing its integrity, native conformation, and biological

function, is the most critical step for developing a biosensor device. In this Chapter, an extensive exploration of different biofunctionalisation strategies was performed for antibody immobilisation and analyte detection.

The covalent attachment of the antibody is mainly the preferred option; for this reason, two different silanes (N_3-silane and APTES) were tested. Different immobilisation strategies were evaluated for the specific case of N_3-silane, using copper-free click chemistry for the covalent antibody immobilisation using DBCO-PEG_4-NHS ester as a crosslinker. However, a low yield in antibody immobilised onto the sensor surface was observed, causing a weak sensor response for a high analyte concentration. These negative results were corroborated using a conventional SPR platform, and the same results were obtained. For this reason, together with a lack of reproducibility, we discarded this strategy for implementation in the POC biosensor platform.

Preliminary results using APTES and PDITC as the crosslinker were obtained. Given the incorporation of the sensor chips inside the microfluidic cartridge and the sensitivity to diluted HNO_3, an in-flow APTES silanisation was carried out. Higher immobilisation signals than with click chemistry were obtained, but the sensor response to the analyte remained low, although some incompatibilities with regeneration strategies were observed. In order to employ this silanisation protocol for the final POC platform, further optimisations of APTES-chemistry will need to be performed.

Finally, the optimal methodology tested and the one that offered the highest immobilisation and analyte detection was physical adsorption. Thus, this strategy was selected for the development of a biosensor for TB diagnosis.

Chapter 4
Evaluation of LAM biomarker for Tuberculosis diagnosis

This Chapter presents the optimisation and validation of the point-of-care platform for the direct and non-invasive lipoarabinomannan (LAM) detection in human urine. This biomarker allows the identification of patients with active Tuberculosis. First, the optimal conditions for the monoclonal antibody immobilisation are assessed, including blocking the free sensor areas. Then, the detection of LAM in buffer and in undiluted urine is described, providing a limit of detection within the clinical range. Finally, the immunoassay validation is carried out with urine samples from Tuberculosis patients, showing the potential of the novel device as an effective point-of-care platform.

4. Evaluation of LAM biomarker for Tuberculosis diagnosis

4.1. Introduction

Despite adequate treatment regimens, the effective global control of TB infection has been hampered due to the absence of a rapid and reliable diagnostic test. As detailed in Chapter 1, current diagnostic methods are costly, time-consuming, insensitive, or inaccurate. Given the dire situation, there is an urgent need to develop a highly sensitive and specific POC platform for the rapid diagnosis of a non-sputum sample in low-resource countries.

Several Mtb cell wall components and secreted antigens seem to be attractive biomarkers for diagnosis purposes in different biofluids such as sputum, urine, and plasma.[47,163] Among the explored biomarkers, lipoarabinomannan (LAM) is potentially the best candidate for a POC platform for a rapid diagnosis of TB.[49]

LAM is a widely known 17.5 KDa lipopolysaccharide found in the mycobacterial cell wall, representing up to 15% of the bacterial mass.[72,73,164,165] As shown in **Figure 4.1**, it consists of three primary structural domains: (i) the phospholipid anchor, which links the Mtb cell wall to the mannan core, (ii) the mannan core, which is a highly conserved carbohydrate skeleton across mycobacterial species, and (iii) a few variable arabinan side chains capped with variable mannose residues.[72,166,167] Several studies have found that LAM molecules play a crucial role in phagocyte evasion,[168] host response modulation during infection,[169] mycobacterial antigen processing inhibition,[168] tumour necrosis factor production,[168] and growth and pathogenesis of *M. tuberculosis*.[170]

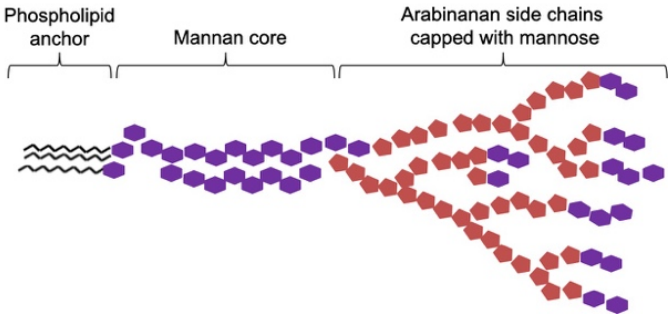

Figure 4.1. Schematic representation of the structure of the LAM antigen.

There are no known human glycosidases for the degradation of LAM, an antigen with glycosidic linkages. Hence, after Mtb lysis by the immune system and filtration by the kidneys, the molecules arrive intact to TB patient urine, making them a potential candidate for TB diagnosis.[165,171] Several studies have confirmed the presence of LAM antigens in the urine of patients with active TB[164,168] and have also found that the amount of LAM in urine is correlated with bacterial metabolic activity and degradation rate, allowing for a semi-quantitative assessment of the infection.[171,172]

Using urine for LAM detection has two main advantages. First, urine can be readily obtained from children and adults without generating hazardous aerosols during sample collection. Secondly, it can be easily stored and does not require a laboratory with a high biosafety level.

There are already two commercial lateral flow tests able to detect this biomarker in urine. Briefly, lateral flow tests are paper-based devices in which the fluid sample migrates along the adsorbent pad with labelled antibodies and generates a visual result when an antibody recognises the specific analyte.[71] One of the available tests is Alere Determine™ TB LAM Ag (AlereLAM; Abbott, US). This lateral flow assay uses polyclonal antibodies for the detection of LAM in urine in 25 minutes with an adequate diagnostic specificity of >98%. However, its sensitivity is unsatisfactory for TB patients without HIV co-infection.[173,174] This technique achieves higher sensitivity (66.7%) for people with less than 50

CD4 cells/μL, who are seriously ill HIV-positive patients, than for patients only infected with TB (4%).[173] On this basis, since 2015, WHO has recommended the use of AlereLAM for the diagnosis of active TB just in HIV-positive patients who are seriously ill or have a CD4 cell count lower than 200 cells/μL.[174]

Another lateral flow test for LAM detection was developed by Fujifilm SILVAMP TB LAM (FujiLAM; Fujifilm, Japan) in 2017, employing high-affinity monoclonal antibodies and providing results in 1 hour.[175] Since then, only one study has described the diagnostic accuracy of FujiLAM, estimating the sensitivity and specificity in patients, with a median of 86 CD4 cells, in 70.4% and 90.8%, respectively.[176] In comparison with the sensitivity (51.7%) obtained with AlereLAM in patients with <100 CD4 counts,[173] FujiLAM offers a higher sensitivity and specificity. Nevertheless, despite its superior performance, the applicability of FujiLAM for TB diagnosis requires more assessments before being recommended by WHO.

Therefore, the sensitivity of existing LAM urine-based tests in HIV-negative patients remains unsatisfactory and are no competitive enough to be able to replace conventional TB diagnostic tests. Recent studies have suggested three hypotheses to explain the problem with the sensitivity of LAM in urine. The first hypothesis states that LAM molecules are released into the urine of active TB patients only when HIV infection causes a glomerular dysfunction.[177,178] The second hypothesis is that LAM is excreted into patient urine with active TB only when the renal tract allows the direct entry to urine of the infected tissue.[179] The third hypothesis holds that LAM concentration in patients with active TB is below the limit of detection of current urine-based tests.[180] Furthermore, another study supports the proposition that the higher sensitivity of these tests in HIV-positive may be related to TB propagation to the kidneys, resulting in an increase of LAM concentration in urine.[178]

For this reason, LIONEX GmbH (Germany) company, which is a partner in the EU project POCKET has developed novel monoclonal antibodies with high affinity, sensitivity, and specificity for LAM antigens, which could improve the performance of LAM tests. These unique antibodies can be used in combination with the previously described sensing platform to create a POC with the ability to detect LAM directly in patient urine samples.

4.2. Materials and methods

4.2.1. Chemical reagents and buffer composition

The following chemical reagents and salts used for buffer preparation and biofunctionalisation were purchased from Sigma-Aldrich (Germany): phosphate buffer saline (PBS: 10 mM Na_2HPO_4, 1.8 mM KH_2PO_4, 2.7 mM KCl, and 137 mM NaCl, pH 7.4), PBST (PBS 10 mM with 0.5% Tween 20, pH 7.4), HEPES (10 mM 4-(2-hydroxyethyl)piperazine-1-ethanesulfonic acid, 150 mM NaCl, pH 7.4). Poly(L-lysine)-graft-poly(ethylene glycol) co-polymer (PLL-g-PEG) was acquired from SuSoS (Switzerland). Milli-Q water from Millipore (US) was always employed.

4.2.2. Biological compounds

A monoclonal IgG antibody against LAM (anti-LAM) and LAM were developed and provided by LIONEX GmbH (Germany). Bovine serum albumin (BSA) was obtained from Sigma-Aldrich (Germany).

4.2.3. Antibody immobilisation and direct immunoassay

The antibody was immobilised by physical adsorption onto the surface of the photonic sensor chip, followed by a blocking step to avoid non-specific adsorptions. Milli-Q water was used as the running buffer at a flow rate of 10 µL/min.

Once the immobilisation process was completed, an immunoassay was performed allowing direct detection of LAM from the sample. The

running buffer was changed to PBS. In order to obtain a complete calibration curve, different LAM concentrations (1, 10, 50, 100, 250, 500, 750 and 1000 ng/mL) were evaluated. An additive assay was performed by flowing successive dilutions of increasing LAM concentrations.

4.2.4. Urine samples

Stored patient urine samples from Tanzania were used for the validation of the TB diagnosis technique. Twenty urine samples were used for this study, including 10 healthy donors, five TB patients with HIV, and five TB patients without HIV. All samples were previously analysed using GeneXpert and sputum smear microscopy.

All patients and healthy volunteers participating in the study gave informed consent for sample donation, and the collection of urine samples from Tanzania was approved by the local ethical committee of the Ministry of Health and Social Welfare, Dar es Salaam, Tanzania (ref. NIMR/HQ/R.8a/Vol.IX/1814).

4.2.5. Data analysis

Data were analysed using OriginPro 8.0 (OriginLab, US) and Prism 8 (GraphPad Software, US). The accumulated response signals were plotted as a function of the accumulated LAM concentrations in order to obtain the calibration curves, which were fitted to a one-site specific binding model (**Equation 4.1**):

$$y = \frac{Ax}{B+x}, \qquad \textbf{(4.1)}$$

where x is the concentration, y is the wavelength shift signal, A is the equilibrium binding constant, and B is the maximum number of binding sites. The experimental LOD was determined as three times the SD of the wavelength shift obtained from a blank signal using only the running buffer.

MedCalc software (Belgium) was used to create a Receiver Operating Characteristic (ROC) curve to show the capability of our POC platform for classifying healthy or TB infected patients. In addition, specificity and sensitivity were calculated using the same software.

4.3. Optimisation and analytical evaluation in buffer

According to the results obtained in Chapter 3, the strategy based on physical adsorption of the antibody onto the sensor surface offered the best results. This strategy consists of the physical adsorption of the anti-LAM antibody onto the sensor surface and a blocking step of the free areas to prevent non-specific adsorptions (see **Figure 4.2**). The evaluation in buffer allows studying the POC platform performance for the specific TB biomarker without the interference of other proteins or compounds that are also present in urine.

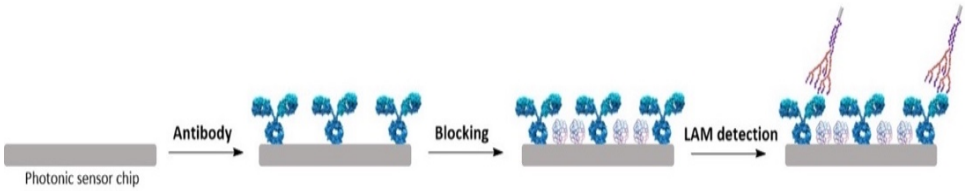

Figure 4.2. Schematic representation of the two main steps involved in physical adsorption and the direct LAM detection.

In accordance with the conditions described in Chapter 3 for this strategy as a starting point, different immobilisation parameters had to be optimised to provide an excellent anti-LAM density with enough accessibility to LAM antigen and to guarantee a suitable surface coverage for minimising non-specific adsorptions. The pH of the buffer used to prepare the antibody solution can play a decisive role, especially in in-flow dynamic reactions as it can favour the local pre-concentration of the receptor on the sensor surface, therefore increasing the yield of the immobilisation. Modulating the pH to a value slightly below the isoelectric point (pI) of the antibody, it can be electrostatically attracted to the photonic sensor surface.[181] First, we studied this influence by injecting

several solutions of 50 µg/mL of anti-LAM prepared in different immobilisation buffers adjusted at various pHs ranging from 4.0 to 7.4 (see **Figure 4.3**). PBS at pH 7.4 was the one resulting in a higher accumulation of the antibody on the sensor surface and was then selected for the immobilisation.

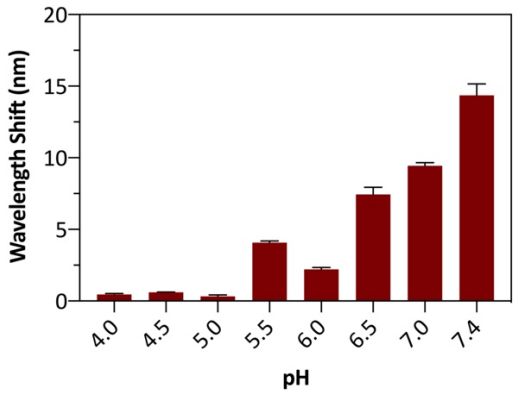

Figure 4.3. Preconcentration signals for anti-LAM (50 µg/mL) prepared in several buffers adjusted at different pHs (4.0 – 7.4).

The appropriate concentration of antibody was then tested flowing different anti-LAM concentrations (10, 20, 50 and 100 µg/mL) at a fixed flow speed (10 µL/min). As expected, immobilisation signals gradually increased with increasing antibody concentration (**Figure 4.4A**). For each case, 1 µg/mL of LAM was injected into the photonic sensor surface. As shown in **Figure 4.4B**, decreasing detection signals can be observed when a higher amount of antibody was immobilised, suggesting that elevated anti-LAM molecules led to steric hindrance effects. Following these results, further experiments were performed with 50 µg/mL of anti-LAM diluted in PBS 10 mM.

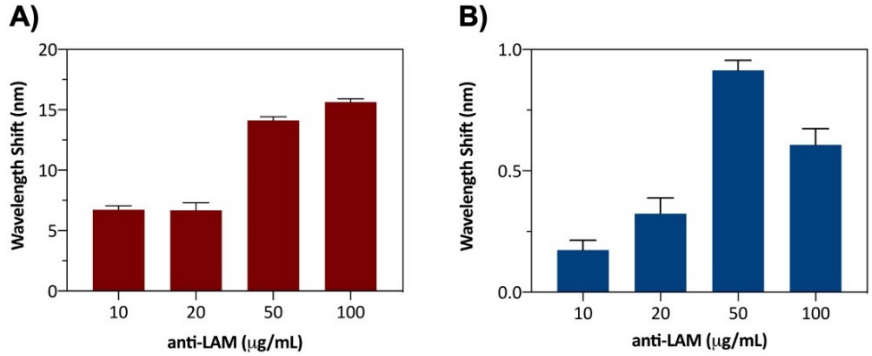

Figure 4.4. (A) Immobilisation signals for different anti-LAM concentrations (10, 20, 50 and 100 μg/mL). **(B)** Sensor responses for the detection of 1 μg/mL in surfaces with different anti-LAM concentrations (10, 20, 50 and 100 μg/mL).

Secondly, the assay was optimised to remove non-specific interactions while maintaining LAM sensitivity and specificity. Different BSA concentrations (from 1 to 10 mg/mL) were immobilised following the antibody functionalisation and after, the binding signal of a non-specific protein was analysed. The role of the BSA was to block the remaining free areas of the sensor surface to avoid non-specific adsorptions. As can be observed in **Figure 4.5A**, a solution with 10 mg/mL of BSA was enough to prevent non-specific adsorptions. Furthermore, it can be seen in **Figure 4.5B** the comparison between the detection of 1 μg/mL of a non-specific protein (control) and the specific response for LAM (500 ng/mL) when 10 mg/mL BSA was employed. This confirmed that positive signals corresponded exclusively to LAM and 10 mg/mL BSA was enough to prevent non-specific interactions.

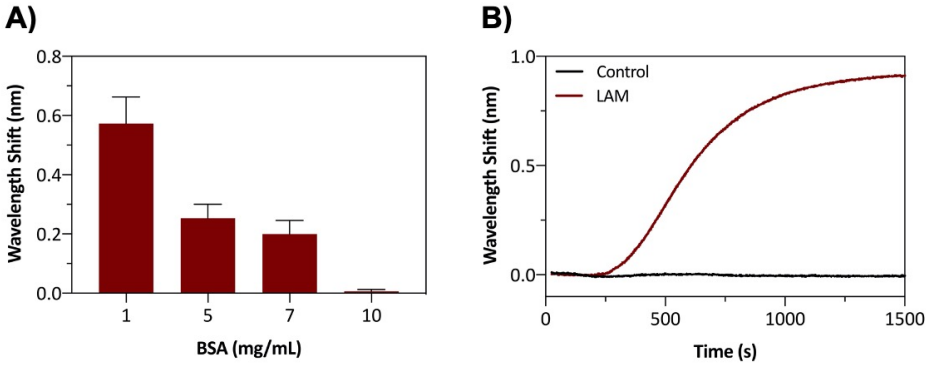

Figure 4.5. (A) Non-specific adsorption of 1 µg/mL of unspecific protein over sensor surfaces with different BSA concentrations (1, 5, 7 and 10 mg/mL). **(B)** Real-time sensorgram comparing the obtained signals for the detection of LAM (500 ng/mL) and for a non-specific.

Once the immobilisation process was optimised for non-specific binding, LAM detection reproducibility was carried out. An example of real-time LAM detection (250 ng/mL) in PBS with the POC biosensor platform is shown in **Figure 4.6A**. An appropriate simultaneous response for all sensors contained in the same photonic sensor chip was observed. The coefficient of variation (CV) of both intra- and inter-assays for the immobilisation procedure and for a specific LAM concentration (250 ng/mL) were lower than 10% (see **Table 4.1**), which is an acceptable value for bioanalytical methods.[182] These results corroborate the excellent reproducibility and low variability for LAM detection. Furthermore, these results strengthen those obtained in Chapter 2, in which no statistically significant difference was observed regardless of the sensors contained in the same photonic sensor chip.

As anti-LAM antibodies are not covalently attached to the sensor surface, it was not possible to regenerate the surface, disrupting the antibody-antigen interaction entirely while maintaining the biorecognition layer intact. For this reason, an additive immunoassay was performed in which different LAM concentrations were sequentially injected to the sensor surface without removing the already bound analytes.

Table 4.1. Intra-assay and inter-assay coefficients of variation (CV) for anti-LAM immobilisation, BSA blocking and LAM detection.

	Intra-assay[a]		Inter-assay[b]	
	Mean ± SD	%CV	Mean ± SD	%CV
anti-LAM (50 μg/mL)	14.14 ± 0.29	2.10	13.72 ± 0.99	7.21
BSA blocking (10 mg/mL)	2.24 ± 0.12	5.30	2.46 ± 0.19	7.86
LAM detection (250 ng/mL)	0.86 ± 0.07	8.08	0.94 ± 0.09	9.10

[a]Triplicates within the same biofunctionalised sensor chip.

[b]Triplicates with three different biofunctionalised sensor chips.

Once the biofunctionalisation protocol appeared to be specific and reproducible for LAM detection, successive dilutions of increasing LAM concentrations ranging from 1 to 1000 ng/mL were flowed over the sensor surface, as shown in **Figure 4.6B**. For all evaluated concentrations, a clear sensor response was obtained. As expected with an additive assay, the antibody reached a saturation level and lost its ability to detect more LAM, explaining the reduced sensor signal for higher LAM concentrations. For example, **Figure 4.6B** shows a higher LAM signal response for 250 ng/mL than for the higher evaluated concentration (1000 ng/mL).

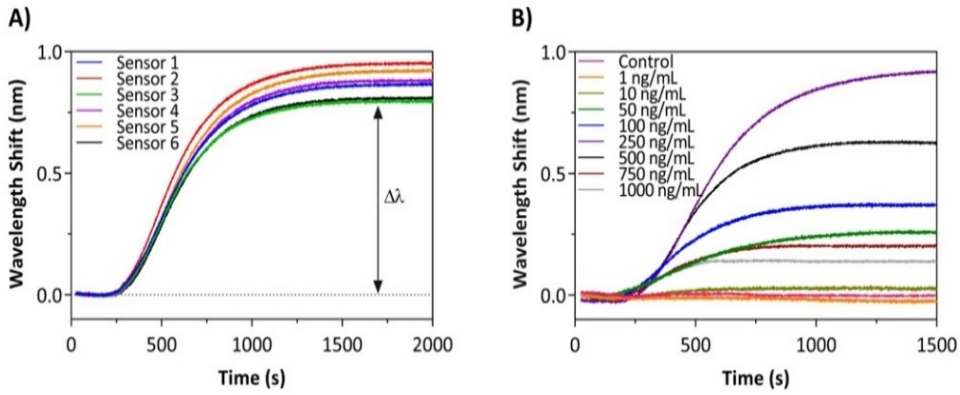

Figure 4.6. (A) Real-time sensorgram showing the detection of 250 ng/mL of LAM in buffer. **(B)** Sensorgrams showing the LAM detection at different concentrations (from 1 to 1000 ng/mL of LAM) in buffer.

A calibration curve for LAM detection in buffer with three replicates for each concentration was plotted, as shown in **Figure 5.7**. The obtained calibration curve showed a liner concentration-dependent region before reaching saturation at 500 ng/mL. A **LOD of 956 pg/mL** equivalent to 54.63 pM (R^2 = 0.98) was estimated, revealing the excellent sensitivity of the sensor and the selectivity of the antibodies against LAM, indicating the excellent performance of the photonic sensor chips and the prototype instrument.

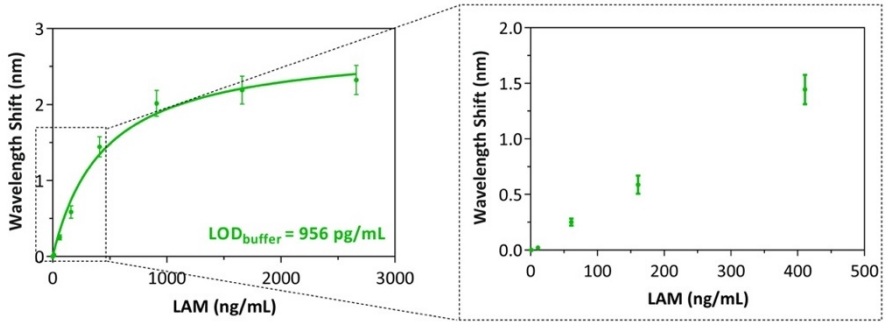

Figure 4.7. Calibration curve obtained for different LAM concentrations in buffer. Solid line corresponds to the one-site specific binding fit. All data show mean ± SD of triplicate measurements.

4.4. Optimisation and direct detection of LAM in urine

The main goal of a sensor applied to clinical diagnosis is to detect a biomarker or a biomarker panel associated with the disease directly in human biological fluids, such as urine, plasma, or sputum. Of these fluids, urine is potentially the ideal candidate for a POC biosensor platform as it can be obtained in large quantities using non-invasive procedures. It can also be easily processed and stored, has no need of trained personnel for its collection, and it has a low risk of infection during sample manipulation.[47,164,171]

Human urine consists primarily of water (91 – 95%), with organic compounds, inorganic ions and to a much lesser extent, enzymes, proteins,

and peptides, among other substances.[183] Urine analysis may become extraordinarily complex due to the high composition variability among patients. For instance, a high salt content can interfere in antibody-antigen interaction and undesired non-specific adsorptions can be produced by other urine interferent components. Therefore, direct evaluation of undiluted urine with an optical sensor, where signals are directly related to mass change, remains a challenge where non-specific adsorptions must be reduced as much as possible or completely eliminated.

Non-specific adsorptions mainly occur when urine components are adsorbed onto the sensor surface by electrostatic and hydrophobic interactions. These non-specific adsorptions can be significantly reduced or removed by diluting the sample, changing buffer composition or chemically modifying the sensor surface. Buffer composition can be modified by adjusting the pH, adding blocking agents (e.g., BSA or dextran derivatives) or surfactants (e.g., Tween 20).[184–186] Another option is to cover the remaining free areas on the sensor surface with BSA, casein, fish gelatin, skim milk, dextran, or PEG derivatives in order to block non-specific binding coming from urine compounds.[152,186–188]

Accordingly, we studied the behaviour of undiluted urine from a healthy patient onto a biofunctionalised surface for the direct detection of LAM. Our biofunctionalised surface already contained a blocking layer with 10 mg/mL of BSA covering the remaining free areas of the sensor chip after anti-LAM immobilisation. This layer was firstly employed to check if BSA was efficient enough as blocking agent for urine analysis. The undiluted urine injection from a healthy patient resulted in a background signal of 1.27 ± 0.21 nm (**Figure 4.8**), suggesting that 10 mg/mL of BSA was not enough to prevent non-specific adsorptions.

Previous studies have demonstrated that coating the sensor surface with PLL-g-PEG and adding Tween 20 (surfactant agent) in the detection buffer minimise the background signal produced by undiluted

urine.[152,187,189] Based on these results, the effect of different blocking agent concentrations to reduce non-specific adsorptions when flowing urine was studied. The anti-LAM antibody was previously immobilised, and several blocking strategies were tested with PBST (PBS 10 mM with 0.5% Tween 20) as running buffer. Firstly, using 0.5 mg/mL of PLL-g-PEG for the surface blocking, a strong reduction of non-specific binding compared with BSA blocking could be observed ($\Delta\lambda = 0.24 \pm 0.05$ nm; **Figure 4.8**), although the result could not be considered as a negligible signal. In order to avoid this tiny signal, a combination of 0.75 mg/mL of PLL-g-PEG and 10 mg/mL of BSA was used to minimise non-specific adsorptions ($\Delta\lambda = 0.08 \pm 0.03$ nm; **Figure 4.8**), obtaining am almost negligible signal. Thus, this strategy was adopted for the evaluation of real urine samples and taking into account this small background signal, a positive TB patient was considered when the sensor response was higher than 80 pm.

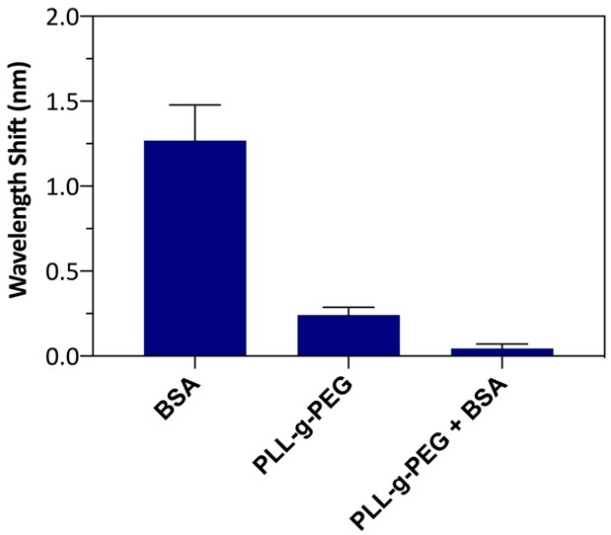

Figure 4.8. Non-specific adsorption of urine from a healthy patient over different blocking agents: 10 mg/mL BSA, 0.75 mg/mL PLL-g-PEG and a combination of both.

4.4.1. Diluted urine

Experiments with diluted urine samples were performed to evaluate the urine interference in the additive assay before the evaluation with undiluted urine samples. Healthy urine samples were spiked with different LAM concentrations ranging from 1 to 1000 ng/mL and diluted 1:1 in PBST 1% (PBS 20 mM with 1% Tween 20). **Figure 4.9A** illustrates the different concentrations of LAM in diluted urine (1:1) and it can also be observed how the baseline remains at the same level after the injection of urine from a healthy individual.

A calibration curve of triplicates for LAM-spiked diluted urine is plotted in **Figure 4.9B**, resulting in a LOD of 731 pg/mL (41.77 pM; R^2 = 0.97). Contrary to what we were expecting, the calibration curve in diluted urine showed higher sensitivity than those obtained in buffer conditions (LOD = 956 pg/mL). These results suggest that urine components create a more favourable environment for the antibody-antigen interaction than the buffer solution. This hypothesis was corroborated by performing the same analysis in undiluted urine.

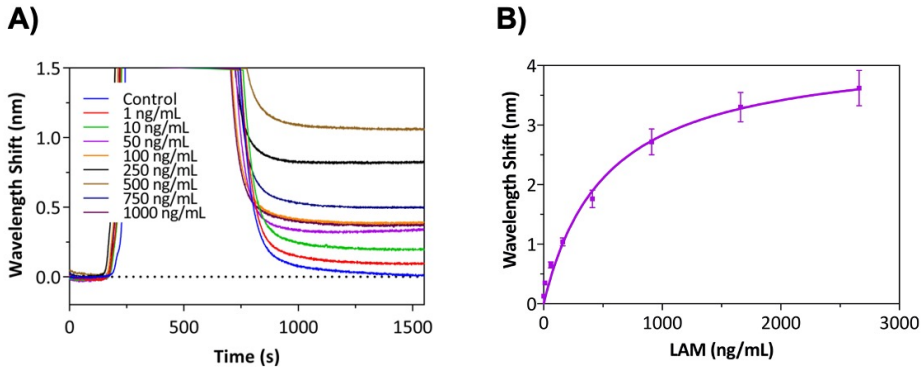

Figure 4.9. (A) Sensorgram showing the LAM detection at different concentrations (from 1 to 1000 ng/mL) in diluted urine (1:1). **(B)** Calibration curve obtained for LAM detection performed in diluted urine (1:1). Solid line corresponds to the one-site specific binding fit. All data show mean ± SD of triplicate measurements.

4.4.2. Undiluted urine

An analogous set of experiments were performed with LAM in undiluted urine. Healthy urine samples were spiked with different LAM concentrations (from 1 to 1000 ng/mL), and injected directly into the sensor. **Figure 4.10A** illustrates the response of different LAM concentrations in undiluted urine. Injection from a healthy donor was performed, resulting in no background signal and confirming the absence of non-specific adsorptions of urine components. When monitoring pure urine in real-time, a peak can be observed when the sample starts to flow in the sensing area, as shown in **Figure 4.10A**. This shift is attributed to a refractive index change between the undiluted urine and the running buffer, as with diluted urine was not observed.

A calibration curve of triplicates for LAM-spiked undiluted urine was plotted as in **Figure 4.10B**, achieving a **LOD of 475 pg/mL** (27.14 pM; R^2 = 0.92). The calibration curve of LAM-spiked undiluted urine with reproducible and repetitive results showed higher sensitivity than in buffer and diluted urine (see **Figure 4.7** and **Figure 4.9B**). Some studies demonstrate that urine components may change the conformation of either antibodies or LAM epitopes in the assay, increasing the sensitivity and accuracy of the immunoassay, which is what can be observed in our experiments.[72]

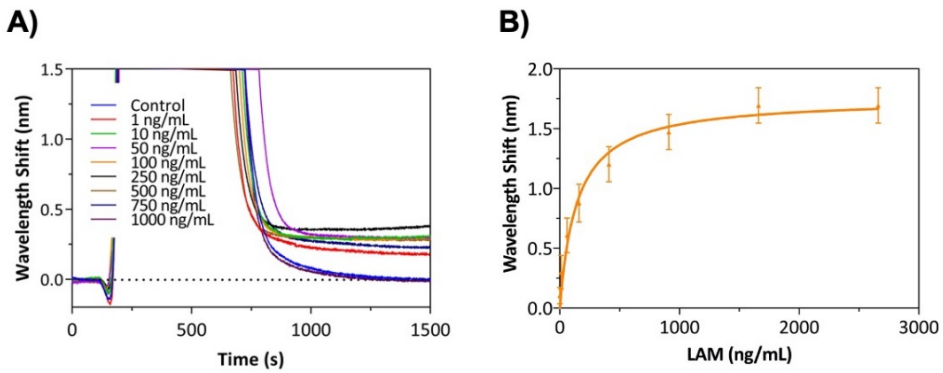

Figure 4.10. (A) Sensorgram showing the LAM detection at different concentrations (from 1 to 1000 ng/mL) and blank urine control. **(B)** Calibration curve obtained for LAM

detection in undiluted urine. The solid line corresponds to the one-site specific binding fit. All data show the mean ± SD of triplicate measurements.

The LOD in undiluted urine obtained with our POC biosensor platform was better than those achieved using lateral flow tests (LOD 10^5 – 10^6 pM) and conventional ELISAs (LOD 7.8×10^4 pM), using different antibodies and immunoassay formats.[58,190,191]

These results confirmed the high sensitivity and specificity of our methodology as well as the robustness of the monoclonal antibodies, the photonic sensor chips, and the complete prototype instrument. In case where a positive signal is observed with this methodology, it would presumably represent the specific recognition of LAM by the antibodies immobilised on the sensor surface.

However, despite the high sensitivity obtained in undiluted urine, there is no definitive information available in the literature or in clinical studies about which one is the minimum concentration of LAM in the urine of TB patients. Some studies have reported minimum values in the range of 15 to 200 pg/mL, but the evaluation was carried out on a limited number of samples of TB patients (with and without HIV).[58,72,171] In the case that such low concentrations have to be reached, they cannot be achieved with a direct immunoassay. For this reason, the use of a secondary antibody for the signal amplification was foreseen in our POC platform and a third syringe was included in the microfluidic cartridge design (see **Figure 2.6**), which can be employed for the injection of the required secondary antibody.

4.5. Validation with clinical urine samples

Given the promising results obtained in spiked urine, we were able to validate the POC biosensor platform using a direct immunoassay in real human urine samples without the need for any sample pre-treatment. There are some parameters, such as pH and the concentration of different urine components, which can enormously vary between patients. An

image of some of the analysed urine samples is shown in **Figure 4.11** to illustrate the variability among samples, which could affect the evaluation.

Figure 4.11. Picture of some of the urine samples employed in the validation of the POC platform.

With the optimal conditions previously selected from the evaluation of spiked urine, the POC platform was applied to study the presence of LAM in the urine of 10 patients from Tanzania with confirmed TB and 10 healthy patients from Tanzania and Spain. The Tanzania samples were collected from hospitals and DOTS (directly observed treatment, short-course) centers,[192] while those from Spain were donated by volunteers. The real status regarding TB diagnosis in urine samples was unknown during the evaluation with the POC biosensor platform.

Non-treated and undiluted urine samples (150 μL) were directly flowed over the sensor surface using the in-flow system (one of the available systems for the fluid injection in the POC platform). Signals were monitored in real-time and classified into positive or negative TB diagnosis depending on the LAM signal, as shown in **Figure 4.12A**. Based on the results obtained during the optimisation process, patients were determined to be TB positive if the LAM signal was higher than 80 pm. Since LAM is a *M. tuberculosis* cell wall component and can only be present in the urine of those patients with active TB, it was not necessary to quantify LAM concentration. Taking into account this threshold, only a single false positive was observed (see **Figure 4.13**).

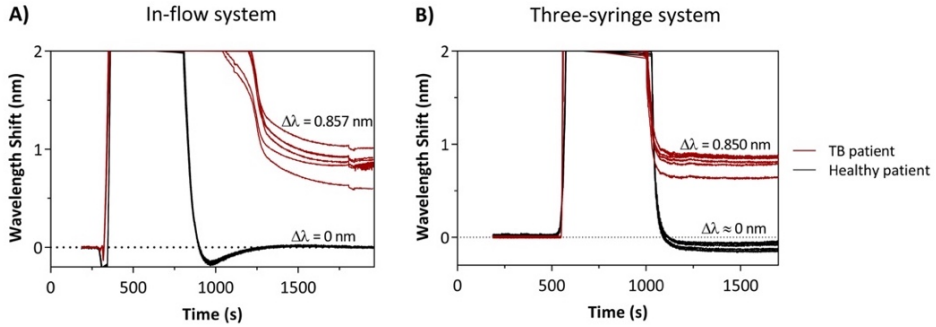

Figure 4.12. Real-time sensorgrams for the comparison of two real urine samples using two different systems for the fluid injection: **(A)** in-flown system and **(B)** three-syringe system.

Positive results with the in-flow system allowed, for the first time, the evaluation and comparison of the same urine samples using the fluid injection component of the POC platform comprising the three-syringe system. This configuration did not use external pumps but a three-syringe system, in which two of the syringes contained PBST and the other one the urine sample (150 μL). A real-time response for the analysis of the same urine sample as for the in-flow system is shown in **Figure 4.12B**. Moreover, in both cases, the healthy urine sample returned to the baseline (**Figure 4.12**). According to both systems results, we did not observe any significant difference in the absolute value of the wavelength shift variation. This can also be observed in a boxplot represented in **Figure 4.13** for the twenty urine samples analysed. The main difference between both systems was observed for Patient 4 (see **Figure 4.13**), who was the only false positive observed when using the in-flow system. Taking into account all these results, we can corroborate the high reproducibility and diagnostics capacity of our novel POC biosensor platform.

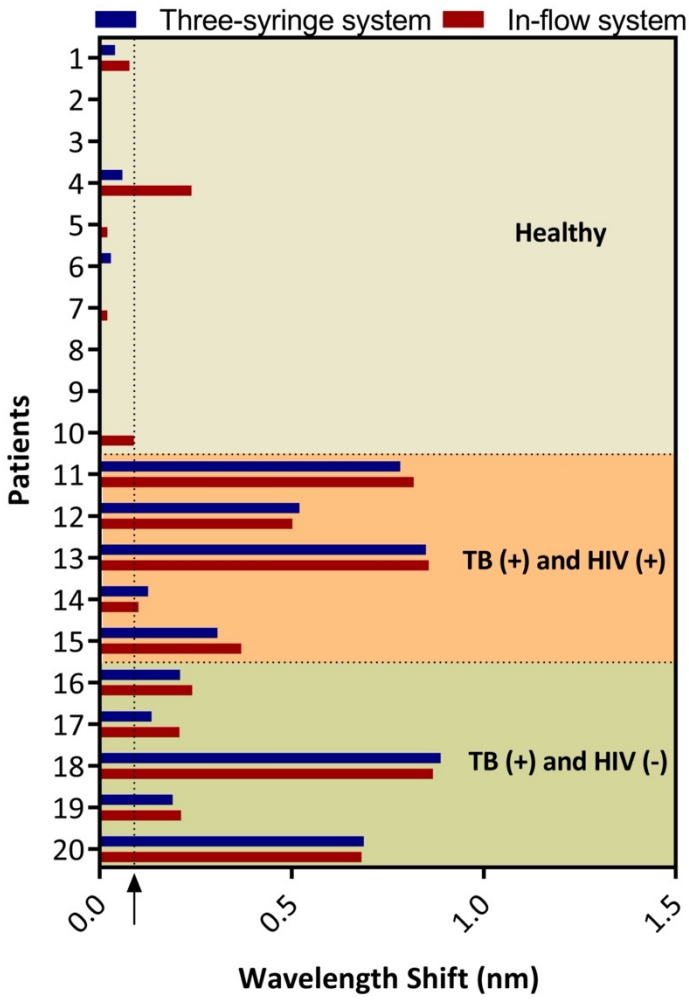

Figure 4.13. Bar plot of the obtained signals from the analysis of twenty urine samples, including healthy and TB patients (with and without HIV) and using two different systems for the fluid injection. The black arrow shows the threshold (80 pm) to classify patients as healthy of TB positive.

As previously explained, one of the disadvantages of the current urine-based LAM detection methods is that they have unsatisfactory sensitivity for TB patients without HIV co-infection, limiting the ability to detect TB in this specific group, which represents the 88% of the total TB new cases worldwide.[4] However, with our novel POC biosensor platform, the classification of patients as healthy or active TB infection, regardless

of HIV co-infection, could be done with a time-to-result of only 15 minutes, as shown in **Figure 4.13**.

Table 4.2 and **Table 4.3** list and compare the results obtained for the evaluation of the twenty real samples with the POC platform and with current active TB diagnosis techniques, such as GeneXpert and sputum smear microscopy. For each patient, the values of pH, HIV status, and current TB diagnosis are reported. Results obtained with our POC platform show an excellent correlation to those obtained with the current TB diagnosis methods. Furthermore, the results suggest that urine pH is not a critical parameter affecting TB diagnosis because the pH level of the analysed samples ranged from 6 to 9.

Table 4.2. Evaluation of urine samples from healthy volunteers with the POC biosensor platform.

		TB diagnosis	
		POC platform	
Healthy donor	**pH**	**Three-syringe**	**In-flow**
1	8	-	-
2	9	-	-
3	9	-	-
4	7	-	+
5	7	-	-
6	7	-	-
7	8	-	-
8	9	-	-
9	8	-	-
10	6	-	-

(+): positive; (-): negative

Table 4.3. Evaluation of urine samples from patients with confirmed TB using current methodologies (GeneXpert and sputum smear microscopy) in comparison to the POC biosensor platform.

			TB diagnosis			
			Current methods		POC platform	
Patient	**HIV**	**pH**	**GeneXpert**	**Sputum Smear Microscopy**	**Three-syringe**	**In-flow**
11	-	8	N/A	N/A	+	+
12	+	8	N/A	N/A	+	+
13	+	8	N/A	N/A	+	+
14	+	7	+	-	+	+
15	-	7	+	+	+	+
16	-	7	+	+	+	+
17	-	8	+	+	+	+
18	+	9	+	+	+	+
19	+	8	+	+	+	+
20	-	6	N/A	N/A	+	+

HIV: HIV status; (+): positive; (-): negative; N/A: not available

The sensitivity and specificity of the POC biosensor platform were evaluated by ROC analysis (**Figure 5.14**). The area under the curve (AUC) was calculated to be 0.983 (95% confidence interval (CI), 0.946 to 1.000) as an overall ROC performance [n = 20 cases, n = 20 control]. This ROC analysis yielded a **sensitivity** of **100%** and a **specificity** of **95%**. Therefore, our novel methodology surpassed the limitations of the rapid tests commercially available for TB diagnosis, making our POC biosensor platform a potential candidate for *in-situ* use in the primary general practitioner's office and patient's bedside.

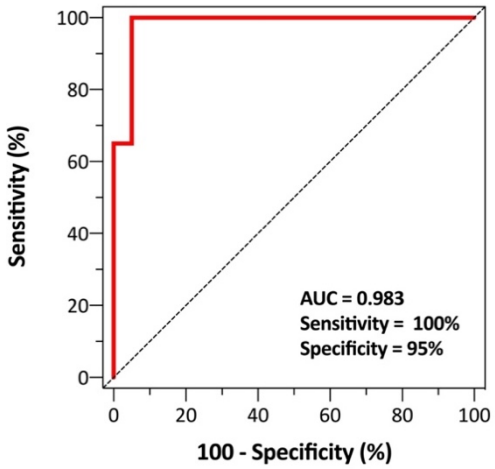

Figure 4.14. ROC curve for the ability of our novel POC platform to identify patients with active TB from undiluted urine samples.

4.6. Conclusions

Much effort has been made in clinical research to overcome the current limitations of rapid tests for TB diagnosis, particularly when applied to HIV-positive patients. In this Chapter, we have fully developed a novel POC biosensor platform for TB diagnosis in urine, employing highly sensitive MZI sensor chips integrated into a microfluidic cartridge. The strategy is based on the direct and label-free LAM detection in unprocessed urine previously immobilising a high-affinity monoclonal antibody by physical adsorption. An in-depth optimisation of several parameters directly affecting the performance of the immunoassay allowed to achieve a LOD as low as 475 pg/mL (27.14 pM) for the direct detection in spiked urine samples.

The methodology was validated with twenty clinical samples from Tanzania TB patients and healthy volunteers and then, for the first time, successfully applied to the detection of TB regardless of HIV co-infection. The results showed an excellent correlation with those obtained with the standard methods currently used for TB diagnosis, including sputum smear microscopy and GeneXpert. Furthermore, the biosensor platform showed high sensitivity (100%) and specificity (95%) and the capacity to

diagnose TB in HIV-negative patients, which is not possible with commercially available urine-based LAM tests.

These promising results together with other advantages such as low-cost, single-use, user-friendliness, results in 15 minutes, no requirement for qualified personnel for operation, and no need for special laboratory infrastructure, make this novel POC biosensor platform an outstanding candidate for *in-situ* use during routine check-ups in developing countries.

As regards future research, the platform would benefit from more validation studies with a higher number of patient urine samples. Additionally, in order to improve the LOD and overcome some of the drawbacks of the additive immunoassay, further experiments are required to find and optimise a compatible biofunctionalisation protocol for the covalent binding of the antibodies.

Chapter 5
Evaluation of complementary biomarkers for Tuberculosis diagnosis

Given the promising results obtained for the rapid diagnosis of LAM in real samples, this Chapter addresses the analysis of four highly specific additional biomarkers for Tuberculosis detection. This panel of biomarkers would allow highly specific discrimination of patients with active Tuberculosis from healthy ones. First, we look for the optimal immobilisation conditions for each selective antibody and surface blocking. Then, each of the biomarkers is quantified in buffer and in undiluted urine. Further experiments will involve the analysis of clinical samples to prove the effectivity of the immunoassays.

5. Evaluation of complementary biomarkers for Tuberculosis diagnosis

5.1. Introduction

During the last few years, potential biomarkers have been identified for TB diagnosis.[51] Unfortunately, despite the numerous reports on new biomarker candidates, only a few *M. tuberculosis* antigens have been evaluated independently for diagnosis.[50,51] One of the reasons is that the vast majority of studies are focused on the improvements of current LAM diagnosis tests, the unique biomarker endorsed by WHO. Moreover, the newly identified biomarkers have not led to a diagnostic test that meets TPP requirements.[43] This suggests that antigen detection is difficult and the assessment of a unique biomarker cannot discriminate between infected and non-infected patients. An alternative to overcome these hurdles and translate biomarker research into a useful TB diagnosis approach could be the simultaneous evaluation of multiple biomarkers. Many efforts are being made in clinical research to stablish a reliable panel of biomarkers for the detection of active TB. For this reason, our clinical partner LIONEX GmbH (Germany), experts in TB and with more than 15 years focused in the evaluation of several TB-biomarkers, have proposed the identification of a biomarker panel that includes antigen 85B (Ag85B), culture filtrate protein 10 (CFP-10), early secretory antigenic target 6 (ESAT-6), and immunogenic protein MPT64.

CFP-10 (10 kDa) and **ESAT-6** (6 kDa) (**Figure 5.1A**) are abundantly secreted proteins at the early growth stage of *M. tuberculosis*.[193] They are encoded by a genomic segment absent in bacillus Calmette-Guérin (BCG) vaccine strain and the most non-pathogenic mycobacteria.[194,195] Furthermore, both proteins form a 1:1 heterodimeric complex in their natural state.[196,197] ESAT-6 and CFP-10 have been reported as playing a crucial role in the virulence of Mtb.[198,199] In fact, CFP-10 reduces the expression of a membrane protein found on several immune cells and limits the production of free oxygen and nitrogen radicals, which are

essential for eliminating Mtb.[200] On the other hand, ESAT-6 induces the production of a type of interleukin in dendritic cells to direct CD4 cell differentiation.[201]

MPT64 (24 kDa; **Figure 5.1B**) is one of the significant culture filtrate proteins secreted by actively dividing *M. tuberculosis*.[63,202] It is encoded by a genomic region only present in Mtb, allowing the differentiation with other mycobacteria species.[203] In addition, MPT64 plays an essential role in Mtb survival and virulence, deactivating the apoptotic cytokine expression.[204–206] A lateral flow test known as SD BIOLINE TB Ag MPT64 rapid test (Abbott, US) is commercially available to detect MPT64 protein in 15 min using monoclonal antibodies. This test allows discriminating between *M. tuberculosis* and non-tuberculous mycobacteria from a mycobacterium isolate with high sensitivity (100%) and specificity (96.4%).[207] However, the main drawback of this test is the time required to grow mycobacteria in cell cultures (up to 12 weeks).

Figure 5.1. Tertiary structure of **(A)** ESAT-6 and CFP-10 heterodimer, **(B)** MPT64, and **(C)** Ag85B.

The **Ag85B** protein (30 kDa; **Figure 5.1C**) is the predominant secretion product of actively replicating Mtb. Ag85B belongs to the antigen 85 complex (Ag85), which comprises two other proteins (Ag85A and Ag85C) encoded by different genes. These three proteins play a crucial role in forming the mycobacterial cell wall due to their enzymatic mycolyl transferase activity.[208,209] There is also evidence that the Ag85 complex is highly immunogenic and is involved in the mycobacterium life

cycle in the host and macrophages through its fibronectin-binding capacities.[210]

These above-explained *M. tuberculosis* antigens have a small molecular weight that varies from 6 to 30 kDa. Since Mtb secrete these proteins and several studies have demonstrated that molecules weighing less than 67 kDa escape freely from kidney filtration,[211] these antigens are considered potential biomarkers for detecting active TB in patients' urine.[57,63,212]

In this Chapter, we focus on the assay optimisation in terms of sensitivity and specificity for the direct detection of each biomarker individually in the buffer and in undiluted urine. The final goal of the study is to be able to evaluate the multiplexed capabilities of the novel POC biosensor platform (Chapter 6).

5.2. Materials and methods

5.2.1. Chemical reagents and buffer composition

The following chemical reagents and salts used for buffer preparation and biofunctionalisation were purchased from Sigma-Aldrich (Germany): phosphate buffer saline (PBS: 10 mM Na_2HPO_4, 1.8 mM KH_2PO_4, 2.7 mM KCl, and 137 mM NaCl, pH 7.4), PBST (PBST 10 mM with 0.5% Tween 20, pH 7.4), acetate buffer (10 mM, pH 5.5), MES buffer (50 mM 2-(N-morpholino)ethanesulfonic acid (MES), pH 5.5), and HEPES (10 mM 4-(2-hydroxyethyl)piperazine-1-ethanesulfonic acid, 150 mM NaCl, pH 7.4). Poly(L-lysine)-graft-poly(ethylene glycol) copolymer (PLL-g-PEG) was acquired from SuSoS (Switzerland). Milli-Q water from Millipore (US) was always employed.

5.2.2. Biological compounds

Bovine serum albumin (BSA) was obtained from Sigma-Aldrich (Germany). A monoclonal IgG antibody against 85B (anti-85B), polyclonal IgG antibody against ESAT-6 and CFP-10 (anti-CEH-ECH),

and polyclonal IgG antibody against MPT64 (anti-MPT64) were provided by LIONEX GmbH (Germany). Recombinant proteins Ag85B, ESAT-6, CFP-10, MPT64, and lipopolysaccharide LAM were also supplied by LIONEX GmbH (Germany).

5.2.3. Antibody immobilisation and direct immunoassay in the buffer

Each antibody was diluted in each corresponding buffer and immobilised by physical adsorption onto the photonic sensor chip surface, followed by a blocking step with 10 mg/mL of BSA to avoid non-specific adsorptions. Milli-Q water was used as the running buffer at a flow rate of 10 µL/min. An additional blocking step with 0.75 mg/mL of PLL-g-PEG was added before blocking with BSA for urine evaluation.

Once the immobilisation process was completed, an immunoassay was performed, allowing direct detection of the analyte. The running buffer was changed to PBS. To obtain a calibration curve, different analyte concentrations (1, 10, 50, 100, 250, 500, 750, and 1000 ng/mL) were evaluated. An additive assay was performed by flowing successive dilutions of increasing analyte concentrations.

5.2.4. Antibody immobilisation and direct immunoassay in undiluted urine

Each antibody was diluted in each corresponding buffer and immobilised by physical adsorption onto the surface of the photonic sensor chip, followed by two blocking steps: (i) 0.75 mg/mL of PLL-g-PEG in HEPES buffer followed (ii) with 10 mg/mL of BSA to avoid non-specific adsorptions from urine components. Milli-Q water was used as the running buffer at a flow rate of 10 µL/min.

Once the immobilisation process was completed, an immunoassay was performed, allowing direct detection of the analyte in the urine

sample. The running buffer was changed to PBST. Healthy urine samples were spiked with different analyte concentrations (1, 10, 50, 100, 250, 500, 750, and 1000 ng/mL) to obtain a calibration curve. An additive assay was performed by flowing successive dilutions of increasing analyte concentrations.

5.2.5. Data analysis

Data were analysed using OriginPro 8.0 (OriginLab, US) and Prism 8 (GraphPad Software, US). The accumulated response signals were plotted as a function of the accumulated analyte concentrations to obtain calibration curves fitted to a one-site specific binding model (**Equation 5.1**). The experimental LOD was determined by multiplying three times the SD of the wavelength shift obtained from a blank signal using only the running buffer.

5.3. Optimisation and analytical evaluation

Based on the excellent results obtained in Chapter 4 for direct LAM detection and taking this as a starting point, these optimised procedures were adapted for each of the four selected biomarkers. The physical adsorption of the corresponding antibody onto the sensor surface, followed by a blocking step, was the pursued strategy for each immunoassay.

5.3.1. CFP-10 and ESAT-6

For the direct detection of CFP-10 and ESAT-6, we employed a polyclonal antibody (anti-CEH-ECH), which could recognise both proteins specifically. Using this antibody is important because, as explained before, CFP-10 and ESAT-6 form a heterodimer in natural conditions. The adsorption of the anti-CEH-ECH onto the photonic sensor surface is mainly attributed to intermolecular forces and is highly dependent on the pI of the antibody, the ionic strength, and the pH of the immobilisation buffer. Thus, a previous optimisation of the immobilisation buffer was done by injecting several anti-CEH-ECH (50 μg/mL) solutions diluted in buffers adjusted at various pHs ranging from 4.0 to 7.4. The

results showed that the higher number of adsorbed antibodies was achieved when using MES buffer at pH 5.50.

Several antibody concentrations ranging between 10 and 100 μg/mL were then tested in the previously selected immobilisation buffer, as in the LAM assay. The sensor response obtained for the anti-CEH+ECH is shown in **Figure 5.2A**, where no significant difference was observed in the immobilisation signal of 10, 20, and 50 μg/mL antibody concentration (10.15 ± 0.31, 10.53 ± 0.28 and 11.07 ± 0.48 nm, respectively). However, a slightly higher antibody adsorbed onto the sensor surface (13.65 ± 0.24 nm) was observed for the higher concentration. This higher immobilisation signal is not always translated into an increased efficiency for the analyte specific recognition. Hence, two solutions, one with 1 μg/mL CFP-10 and another with the same ESAT-6 concentration, were injected onto the different biofunctionalised sensor surfaces (anti-CEH+ECH + 10 mg/mL BSA) using PBS as the running buffer. As shown in **Figure 5.2B**, the ESAT-6/CFP-sensor responses were higher when 50 μg/mL antibody was immobilised than when higher amounts of antibody were used, suggesting that more elevated antibody amounts lead to steric hindrance. However, although immobilisation values were very similar to those in the LAM assay, we observed that the obtained wavelength shifts for the detection of 1 μg/mL of CFP-10 and ESAT-6 were lower (0.23 ± 0.06 and 0.19 ± 0.05, respectively). The reasons for this could be related to the affinity of the antibody (polyclonal) for their antigens, which could be less than the anti-LAM (monoclonal)/LAM pair, or it could also be related to the low molecular weight of CFP-10 and ESAT-6 (10 and 6 kDa, respectively), since the working principle of the photonic biosensor is directly related to mass change, which could complicate the detection and affect the immunoassay sensitivity. Thus, the 50 μg/mL of anti-CEH+ECH concentration was selected to evaluate the direct immunoassay sensitivity and specificity. The results of the immobilisation step showed high reproducibility between different photonic sensor chips (CV = 6.11%).

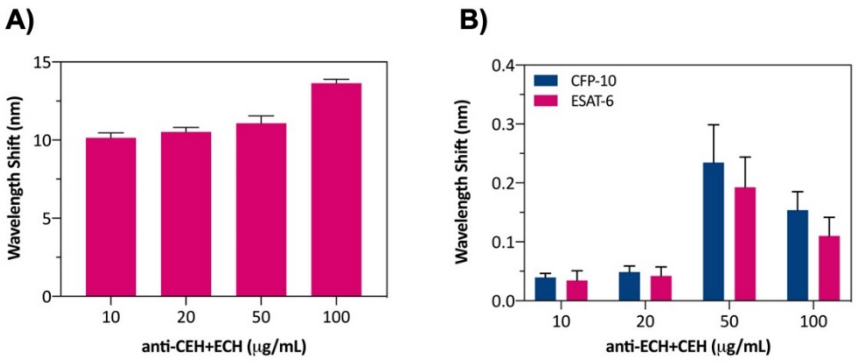

Figure 5.2. (A) Immobilisation signals for different anti-CEH+ECH concentrations (10, 20, 50 and 100 µg/mL). **(B)** Sensor responses for the detection of 1 µg/mL CFP-10 and ESAT-6 in surfaces with different anti-MPT64 concentrations (10, 20, 50 and 100 µg/mL).

The biofunctionalised sensor surface capabilities to specifically recognise CFP-10 and ESAT-6 were evaluated by flowing a solution with 1 µg/mL of LAM (unspecific analyte). As can be observed in **Figure 5.3A,** a blocking step with BSA (10 mg/mL), previously optimised in Chapter 5, was enough to avoid non-specific adsorptions while keeping the surface sensitive enough for ESAT-6 and CFP-10.

Once the immobilisation process was optimised, two additive immunoassays were performed independently, one for ESAT-6 and another for CFP-10. In both cases, different antigen concentrations ranging from 1 to 1000 ng/mL were flowed over the sensor surface without disrupting the already formed antibody-antigen interaction. Calibration curves in PBS buffer were generated by analysing several concentrations in triplicate (**Figure 5.3B**). Neither of the calibration curves reached saturation of the sensor response in the interval of concentrations analysed. From these curves, **LODs** of **32.03 ng/mL** (R^2 = 0.94) and **29.04 ng/mL** (R^2 = 0.96) ng/mL were calculated for ESAT-6 and CFP-10, respectively.

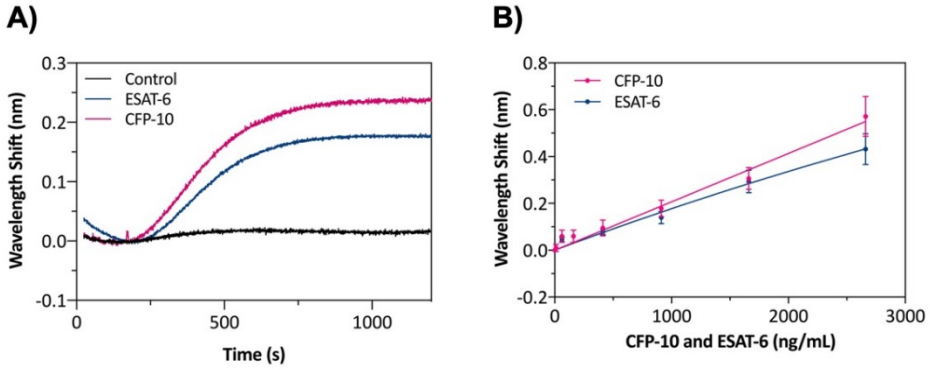

Figure 5.3. (A) Real-time sensorgram comparing the obtained signals for the detection of ESAT-6 and CFP-10 (1 µg/mL) and for a non-specific protein (control; 1 µg/mL). **(B)** Calibration curve obtained for different ESAT-6 and CFP-10 concentrations in buffer. All data show mean ± SD of triplicate measurements.

Despite the low sensitivity achieved, the immunoassay performance for the direct detection of both proteins in the TB patient urine samples was tested. As previously optimised in Chapter 5, an additional step with 0.75 mg/mL of PLL-g-PEG was required to completely avoid non-specific adsorptions. In addition, the running buffer was changed to PBS with 0.5% of Tween 20 (PBST) after the immobilisation and blocking steps. Taking this into account, a healthy urine sample was firstly flowed over the sensor surface, and as it can be observed in **Figure 5.4A**, the baseline remained at the same level after the injection. In contrast, urine samples that were spiked independently with ESAT-6 and CFP-10 (**Figure 5.4A**) gave a positive signal, demonstrating that this blocking was enough to avoid non-specific adsorptions from urine components.

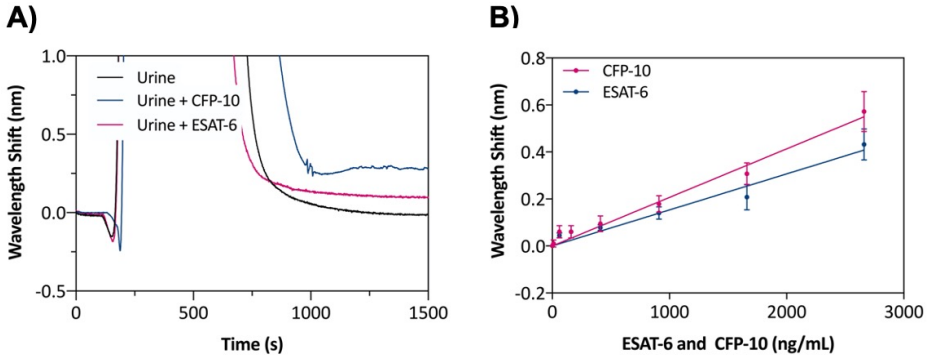

Figure 5.4. (A) Sensorgram comparing the detection of ESAT-6 and CFP-10 (1 µg/mL) in undiluted urine and a blank urine as a control. **(B)** Calibration curve obtained for ESAT-6 and CFP-10 detection performed in undiluted urine. All data show mean ± SD of triplicate measurements.

Two calibration curves, one for ESAT-6 and another for CFP-10, were performed in triplicate using healthy urine samples that were spiked with different concentrations of each protein (from 1 to 1000 ng/mL). Both calibration curves are plotted in **Figure 5.4B**, resulting in a **LOD** of **39.12 ng/mL** (R^2 = 0.92) and **35.68 ng/mL** (R^2 = 0.94) ng/mL for ESAT-6 and CFP-10, respectively. As this figure shows, the sensitivity in urine is slightly worse than in buffer conditions, suggesting that some matrix effects might affect the antibody-antigen interaction.

5.3.2. MPT64

For the detection of MPT64, we used the same protocol conditions (i.e., antibody physically adsorbed onto the sensor surface and blocking with 10 mg/mL of BSA), which worked perfectly for the specific detection of LAM, ESAT-6, and CFP-10. The adsorption of the polyclonal antibody anti-MPT64 was tested by diluting it in different immobilisation buffers of increasing pH from 4.0 to 7.4. Results showed that the buffer with the highest immobilisation yield was acetate buffer at pH 4.5.

The amount of physically adsorbed antibody onto the photonic sensor surface is crucial for the optimal immunoassay performance. Therefore,

optimisation with four concentrations of anti-MPT64 (10, 20, 50, and 100 µg/mL) was carried out. The wavelength shift induced by the adsorption of each anti-MPT64 concentration is shown in **Figure 5.5A**. As expected, an increasing tendency was observed with higher antibody concentrations. Moreover, overall immobilisation signals were lower than those observed with the antibodies against LAM and CFP-10/ESAT-6. However, the detection of 1 µg/mL of MPT64 gave a response for all the antibody concentrations tested (see **Figure 5.5B**), giving the highest response (0.59 ± 0.08 nm) when the 50 µg/mL anti-MPT64 concentration was adsorbed onto the sensor surface. A high reproducibility in the immobilisation step among different photonic sensors was observed with a coefficient of variation of 8.59%.

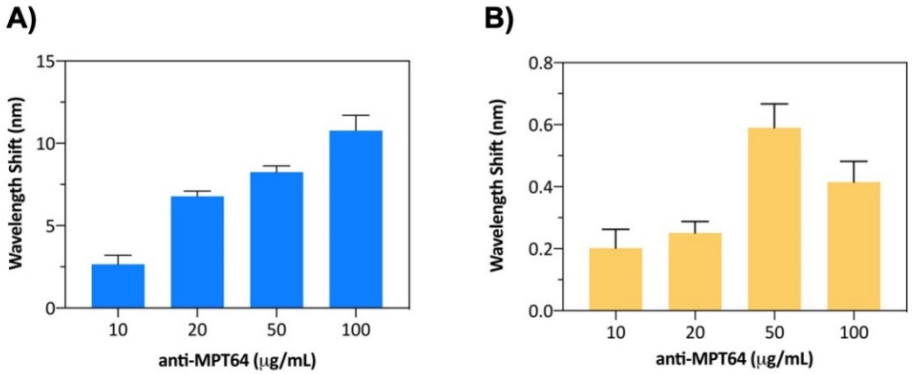

Figure 5.5. (A) Sensorgram showing the detection of ESAT-6 and CFP-10 (1 µg/mL) in undiluted urine and a blank urine as a control. **(B)** Calibration curve obtained for CFP-10 and ESAT-6 detection performed in undiluted urine. All data show mean ± SD of triplicate measurements.

Firstly, the specificity control was carried out by flowing a solution with 1 µg/mL of LAM, leading to a negligible biosensor response (**Figure 5.6A**). This result confirmed the absence of non-specific adsorptions and demonstrated that the sensor response was produced exclusively by the specific antigen (MPT64; **Figure 5.6A**).

Finally, a calibration curve for direct MPT64 detection was carried out in triplicate. Successive dilutions of increasing MPT64 concentrations

(from 1 to 1000 ng/mL) were flowed over the sensor surface to obtain the curve. The calibration curve (**Figure 5.6B**) showed a linear concentration-dependent region before reaching saturation at 1000 ng/mL with an estimated **LOD** of **5.38 ng/mL** (R^2 = 0.97).

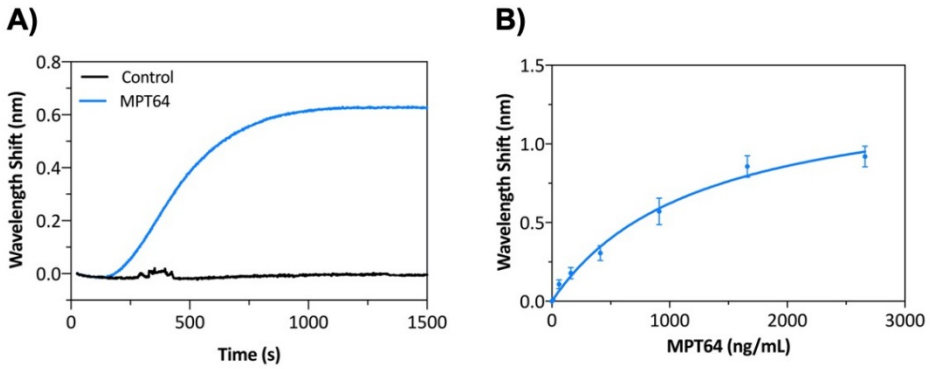

Figure 5.6. (A) Real-time sensorgram comparing the obtained signals for the detection of MPT64 (1 µg/mL) and for a non-specific protein (control; 1 µg/mL). **(B)** Calibration curve obtained for different MPT64 concentrations in buffer. All data show mean ± SD of triplicate measurements.

With the promising results obtained in buffer conditions, we decided to evaluate the optimised immunoassay capabilities for the direct detection of MPT4 protein in urine. Healthy urine samples were spiked with different MPT64 concentrations (from 1 to 1000 ng/mL) and injected directly over the sensor surface. **Figure 5.7A** compares the resulting signals from the flow of undiluted urine with and without MPT64. Injection of healthy donor urine generated no background signal and confirmed the absence of non-specific adsorptions from urine components. Conversely, a specific signal was obtained exclusively for the presence of MPT64 in urine.

A calibration curve in triplicate for the MPT64-spiked undiluted urine is plotted in **Figure 5.7B**, achieving a **LOD** of **6.67 ng/mL** (R^2 = 0.96). These results demonstrated that the urine matrix did not affect the specific interaction between the antibody and the protein, as no significant

differences were apparent between the sensitivity obtained in the buffer and the urine.

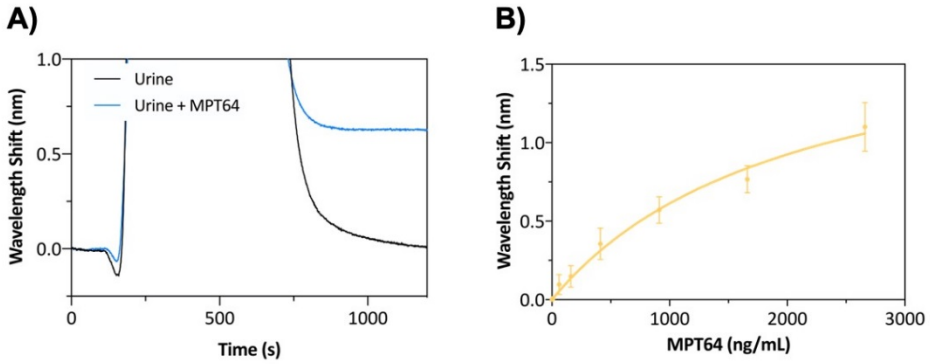

Figure 5.7. (A) Sensorgram showing the detection of MPT64 (1 µg/mL) in undiluted urine and a blank urine as a control. **(B)** Calibration curve obtained for MPT64 detection performed in undiluted urine. All data show mean ± SD of triplicate measurements.

5.3.3. Ag85B

The above-mentioned protocol, including physical adsorption of monoclonal anti-85B followed by a blocking step of the sensor surface free areas with a 10 mg/mL BSA solution, was carried out for the direct detection of Ag85B. The monoclonal antibody adsorption was tested by diluting it in different immobilisation buffers of increasing pH (from 4.0 and 7.4). Results showed that the buffer with the highest immobilisation yield was PBS buffer at pH 7.4.

The amount of antibody physically adsorbed onto the photonic sensor surface was evaluated to assure the optimum surface coverage. For this reason, four different antibody concentrations (10, 20, 50, and 100 µg/mL) were assessed as in previous optimisations. The sensor response obtained for the anti-85B detection is represented in **Figure 5.8A**, where a positive trend gradually increases with antibody concentration. Furthermore, the same tendency was also observed for the detection of Ag85B (1 µg/mL; **Figure 5.8B**). Because a similar response was obtained with 50 and 100 µg/mL of antibody adsorbed onto the sensor surface (0.18 ± 0.03 and 0.21

± 0.02 nm, respectively), the lower concentration of anti-85B (50 µg/mL) was selected for further experiments. In this case, the detection signals were lower than the signals for other analytes. This could be related to a lower antibody affinity for its specific antigen because the Ag85B protein is the one having the largest molecular weight.

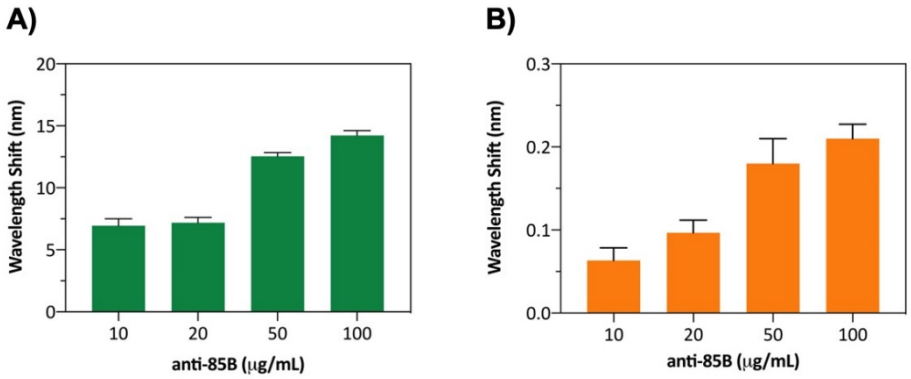

Figure 5.8. (A) Immobilisation signals for different anti-85B concentrations (10, 20, 50 and 100 µg/mL). **(B)** Sensor responses for the detection of 1 µg/mL Ag85B in surfaces with different anti-85B concentrations (10, 20, 50 and 100 µg/mL).

The specificity of the Ag85B immunoassay was assessed by flowing a control analyte. A negligible signal was observed when injecting the non-specific antigen (1 µg/mL LAM; **Figure 5.9A**). In contrast, the target protein (**Figure 5.9A**) resulted in a clear sensor response, corroborating the lack of non-specific binding over the blocked surface.

A calibration curve for Ag85B detection in PBS with three replicates for each concentration is plotted, as shown in **Figure 5.9B**. The interval of analysed concentrations (from 1 to 1000 ng/mL) did not reach signal saturation. A **LOD** of **8.49 ng/mL** was estimated, although the fitting was slightly worse (R^2 = 0.91) compared with the ones for the other analysed biomarkers. This may also be related to the lower affinity of the anti-85B antibody to its antigen (Ag85B).

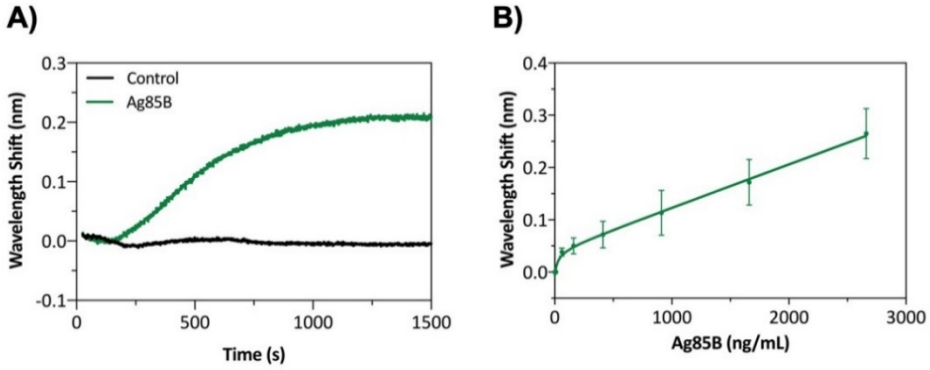

Figure 5.9. (A) Real-time sensorgram comparing the obtained signals for the detection of Ag85B (1 µg/mL) and for a non-specific protein (control; 1 µg/mL). **(B)** Calibration curve obtained for different Ag85B concentrations in buffer. All data show mean ± SD of triplicate measurements.

The immunoassay performance for the direct detection of Ag85B in urine was also tested despite the lower signals. The wavelength shift induced by the flow of urine from a healthy donor and Ag85B-spiked urine over the sensor surface is shown in **Figure 5.9A**. Clear sensor response was obtained when Ag85B was present in urine compared to the negligible response obtained for healthy urine. This result confirms the absence of non-specific adsorptions and demonstrates that the sensor response came exclusively from Ag85B.

A calibration curve in triplicate for Ag85B-spiked undiluted urine is plotted in **Figure 5.9B**, achieving a **LOD** of **11.92 ng/mL** (R^2 = 0.89). These results demonstrate that the urine matrix does not affect the specific interaction between the antibody and the protein, as no significant differences were detected between the sensitivity obtained in the buffer and the urine.

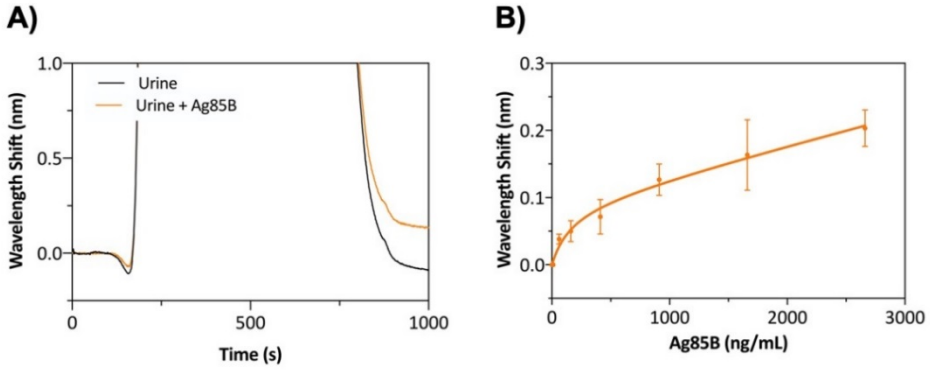

Figure 5.10. (A) Sensorgram showing the detection of 1 µg/mL of Ag85B in urine and blank urine control. **(B)** Calibration curve obtained for Ag85B in undiluted urine. All data show the mean ± SD of triplicate measurements.

5.4. Discussion

Despite the high sensitivity obtained for the selected panel of TB biomarkers in buffer and in undiluted urine (see **Table 5.1**), previous reports give no information about which one is each protein concentration range in the TB patients urine. Instead, the vast majority of reported studies only compare the immunoassay capabilities to discriminate between positive TB patients and healthy donors.[207,213–215]

Table 5.1. Summary of the sensitivity achieved for each analysed TB biomarker in buffer and undiluted urine.

	MW (kDa)	LOD (ng/mL)	
		PBS buffer	Undiluted urine
LAM	17	0.96	0.47
CFP-10	10	29.04	35.68
ESAT-6	6	32.03	39.12
MPT64	24	5.38	6.67
Ag85B	30	8.49	11.92

Among the few reported studies which have performed a quantitative analysis of the selected biomarkers, the vast majority employ a sandwich assay instead of a direct immunoassay, as in our case. Taking this

difference into account, the achieved LOD for the direct detection of MPT64 and Ag85B in undiluted urine with our POC platform is similar to the reported studies (LOD 2.1, 8, and 10 ng/mL) using conventional ELISAs and SPR biosensors.[55,216,217] However, for the specific case of ESAT-6 and CFP-10, reported LODs (0.006 and 0.01 ng/mL) are better than the sensitivity achieved with our POC biosensor platform.[57,218] Moreover, a recently reported electrochemical sensor for MPT64 demonstrates that using aptamers instead of antibodies might help achieve higher sensitivity values (LOD 0.33 fg/mL).[219] The same effect has also been observed using quantum dots and nanorods for Ag85B detection (LOD 13 pg/mL).[220]

Despite the lower sensitivity obtained in our results, which can be mainly related to the affinity of the antibodies employed, our POC biosensor platform is advantageous compared with the other reported techniques because trained staff are not required, results are obtained in 15 minutes without the need of secondary amplification, and there is no need for sumptuous laboratory infrastructure. For these reasons, we think that an extended validation study should be performed in the future with real clinical samples to determine if the sensitivity obtained with our platform is high enough to discriminate between infected and non-infected patients by analysing each biomarker independently. If results show that an improvement in assay sensitivity is required, this could be achieved by modifying the microfluidic cartridge design to allow for an amplification step with a secondary antibody in addition to look for more specific bioreceptors if available.

5.5. Conclusions

In this Chapter, we have successfully developed a photonic biosensor for the direct and label-free identification of four TB biomarkers: ESAT-6, CFP-10, Ag85B, and MPT64 in undiluted urine. All the optimisations performed for LAM (Chapter 4) were taken as a starting point for this study, and then, adapted for each biomarker. The LODs achieved were

35.68 ng/mL for CFP-10, 39.12 ng/mL for ESAT-6, 6.67 ng/mL for MPT64, and 11.92 ng/mL for Ag85B in unprocessed urine. Despite the high sensitivity obtained for the selected panel of TB biomarkers, there is no available information about the concentration range of each protein in urine of patients with active TB. A validation study with clinical TB samples should be performed in the future to determine if the obtained sensitivity allows discriminating patients with active TB from healthy ones. If higher sensitivity is needed, an amplification step (e.g., secondary antibody) can be added to improve the LOD.

Overall, these results demonstrate the feasibility of using the novel POC biosensor platform for TB diagnosis in a label-free and direct format, revealing that the technology is not limited to LAM detection. Furthermore, as the photonic sensor chip is designed for the simultaneous detection of a panel of six different biomarkers, this opens the door for the use of our POC platform for the fast and simultaneous detection of the previously studied TB biomarkers in a single urine sample.

Chapter 6
Multiplexed biosensor for active Tuberculosis diagnosis

In this Chapter, we exploit the multiplexed capabilities of the photonic sensor chip for the detection of a Tuberculosis biomarker panel. Dip-Pen Nanolithography was employed for the immobilisation of two different antibodies on different Mach-Zehnder Interferometers. First, we evaluated the optimal parameters for the solution deposition (viscosity, hydrophobicity, and cantilever size). After that, ex-situ immobilisation was tested with two different antibody concentrations, and preliminary results for Tuberculosis biomarker simultaneous detection were obtained.

6. Multiplexed measurements for active Tuberculosis diagnosis

6.1. Introduction

Early and accurate TB diagnosis plays a decisive role in its effective treatment and preventing the spread of this infectious disease. Many biomarker-based tests are currently designed to diagnose based on a single biomarker associated with a specific disease, leading to low sensitivity, as happens with the commercially available LAM test.[174] In fact, in order to increase sensitivity and develop an accurate and reliable clinical diagnostic method, the simultaneous screening of several biomarkers is often required.[221] Therefore, there has been a strong interest over the last few years in the development of **multiplexed** tests, which allow interrogating several biomarkers at the same time within the same patient sample.[222,223]

However, detecting multiple analytes in a unique immunoassay has introduced another challenge associated with the immobilisation of different biological receptors in defined locations over the sensor surface. The optimal way to allocate multiple bioreceptors on a microscopic sensor surface is based on **microarrays**, where ten to thousands of spots can be generated with different bioreceptors in each array. To date, a variety of printing technologies have been developed for spotting small volumes of biomolecules in a controlled mode. The more prominent array fabrication technologies include lithography (i.e., photolithography, electron-beam, and dip-pen), contact (i.e., pin printing, microstamping, and flow printing), and non-contact (i.e., thermal inkjet, piezo actuation, and valve jet).[224]

Among the different printing technologies, **dip-pen nanolithography** (DPN) is a powerful patterning technique that can deliver small volumes directly where desired on the sensor surface. It consists of a modified atomic force microscope (AFM) cantilever that is immersed in a spotting solution, and is then transferred to the sensor surface in writing mode,

creating the desired pattern (spots or lines) by moving the cantilever across the sensor surface (**Figure 6.1**).[225] The main advantage of this method is that it can deliver various biomolecules onto a single sensor surface by immersing the cantilever in different spotting solutions (see **Figure 6.1**). However, the mechanism of transporting the spotting solution from the cantilever to the sensor surface is complex. Several parameters can affect the process, such as the spotting solution viscosity, temperature, humidity, and other deposition parameters (e.g., dwell time, rate, and surface and cantilever hydrophobicity).[226,227] Besides, the modified AFM cantilever size can range from between 10 and 60 μm. Despite all these parameters, DPN has been successfully applied to produce protein,[228] antibody,[229,230] DNA,[229] lipid,[231] and nanostructure arrays.[232]

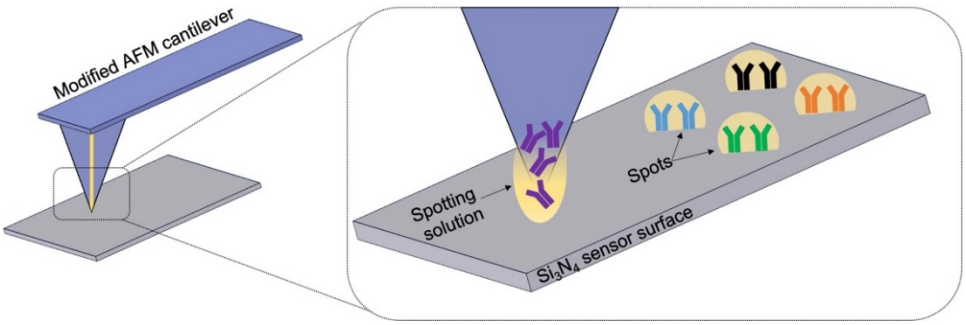

Figure 6.1. Schematic representation of Dip-Pen Nanolithography.

Until now, a POC multiplexed biosensor platform able to discriminate with high accuracy infected TB patients from non-infected patients regardless of HIV-coinfection has not yet been developed. In consequence, and to significantly increase the value of our novel POC platform, we decided to exploit the design of our photonic sensor chip for the simultaneous detection of a six TB biomarker panel in the same patient urine sample (**Figure 6.2**). In this Chapter, several parameters directly affecting the printing of different antibodies onto the photonic sensor chip using DPN have been evaluated and optimised. The final goal of this study is the simultaneous evaluation of the biomarkers assessed previously in Chapter 4 and 5.

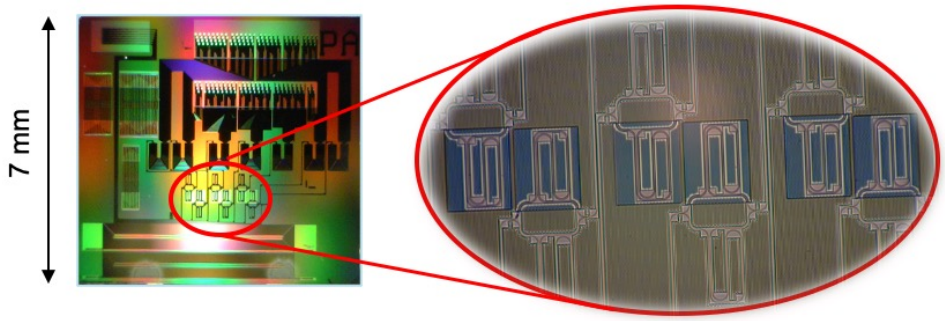

Figure 6.2. Photograph of the photonic sensor chip. Zoom in showing the six MZI sensors integrated in photonic sensor chip.

6.2. Materials and methods

6.2.1. Chemical reagents and buffer composition

Chemical reagents and salts used for buffer preparation and biofunctionalisation were purchased from Sigma-Aldrich (Germany): glycerol, phosphate buffer saline (PBS: 10 mM Na_2HPO_4, 1.8 mM KH_2PO_4, 2.7 mM KCl, and 137 mM NaCl, pH 7.4). Poly(L-lysine)-graft-poly(ethylene glycol) copolymer (PLL-g-PEG) was acquired from SuSoS (Switzerland). Milli-Q water from Millipore (US) was always employed.

6.2.2. Biological samples

Bovine Serum Albumin (BSA) was purchased from Sigma-Aldrich (Germany). Human C-Reactive Protein (CRP) and monoclonal IgG antibody against CRP C7 (anti-CRP) were acquired from BBI Solutions (UK) and HyTest (Finland), respectively. Lipoarabinomannan (LAM), antigen 85B (Ag85B), and a monoclonal IgG antibody against LAM (anti-LAM) were provided by LIONEX GmbH (Germany).

6.2.3. Antibody immobilisation by Dip-Pen Nanolithography

The DPN spotter NanoInk (NanoInk Inc., US) was used for the immobilisation of multiple antibodies in the sensor surface. A modified

AFM cantilever of 30 μm was purchased from BioForce Nanoscience (US) and was used to deposit small volumes of antibodies onto the photonic sensor surface. The modified AFM cantilever was always treated by oxygen plasma (Electronic Diener, Germany) for 2 min at 45 sccm gas flow before use. Different antibody solutions were spotted on the sensor surface at high humidity conditions (75 – 80% Relative Humidity).

6.2.4. Direct immunoassay

Once the surface biofunctionalisation was carried out, a solution with 1 μg/mL of CRP diluted in PBS was injected into the system at 20 μL/min.

6.2.5. Data analysis

Data were analysed using OriginPro 8.0 (OriginLab, US) and Prism 8 (GraphPad Software, US).

6.3. Design and optimisiation of antibody immobilisation using Dip-Pen Nanolithography

A Dip-Pen Nanolithography system was employed for the selective deposition of different antibodies on each MZI sensor available in the photonic sensor. This molecular printing platform enables the direct deposition of 10 – 60 μm size droplets with high position resolution. The deposited drop size depends on the contact time and the force between the modified AFM cantilever cantilevers and the sensor surface. The molecules to be printed are loaded into the modified AFM cantilever reservoir with 0.5 μL of the corresponding solution by using a pipette. Previously, the modified AFM cantilever must be treated with oxygen plasma to reduce hydrophobicity and allow the flow of the spotting solution through the cantilever by capillary force. Glycerol is often used to regulate the viscosity, to facilitate the flow, and to reduce the spot evaporation.

A series of experiments were performed to assess the optimal parameters, including printing contact time (1 – 5 s), various percentages of glycerol (0 – 10%), the activation of the photonic sensor surface through oxygen plasma (1 – 5 min) and the printing cantilever size. Our partner in the project, IMEC (Belgium), provided us with photonic sensor chips without microfluidic cartridge to perform these experiments.

Firstly, the percentage of glycerol in the spotting solution was assessed. Different glycerol percentages ranging from 0 to 10% were added to the PBS solution. As expected, the presence of glycerol in the spotting solution facilitated the deposition. A solution with 1% and 10% of glycerol resulted in tiny spots; however, when 5% of glycerol was used, the spots were significantly larger. Therefore, 5% glycerol in the solution was selected for further optimisations.

Secondly, the activation of the sensor surface using oxygen plasma was evaluated. Different photonic sensor chips were activated at different times (from 1 to 5 min). As shown in **Figure 6.3**, the activation time influenced the deposition efficiency by generating hydroxyl groups which facilitate the physical adsorption of the biological receptors in the photonic sensor surface. A photonic sensor chip activated for 2 min resulted in a deposition drop with high volume (see **Figure 6.3A**). In contrast, higher activation times made the sensor surface highly hydrophilic, and when the spotting solution was deposited into the MZI sensor, the spot spread over the sensor surface (see **Figure 6.3B**). This could have complicated the deposition control and negatively affected the multiplex sensor because the solution could have contaminated the aside MZI sensor. Thus, a previous surface activation with 2 min in oxygen plasma was selected for further experiments.

Finally, we had to optimise the cantilever size and so, the spot size. In our case, selecting the spot size was not crucial because our aim was the deposition of antibodies solution within each MZI sensing arm (180 x 270 μm). With bigger cantilever sizes, the sensor area will be filled more quickly, whereas smaller sizes will require more depositions. For this

reason, a modified AFM cantilever of 30 μm was selected for the development of the multiplexed chip.

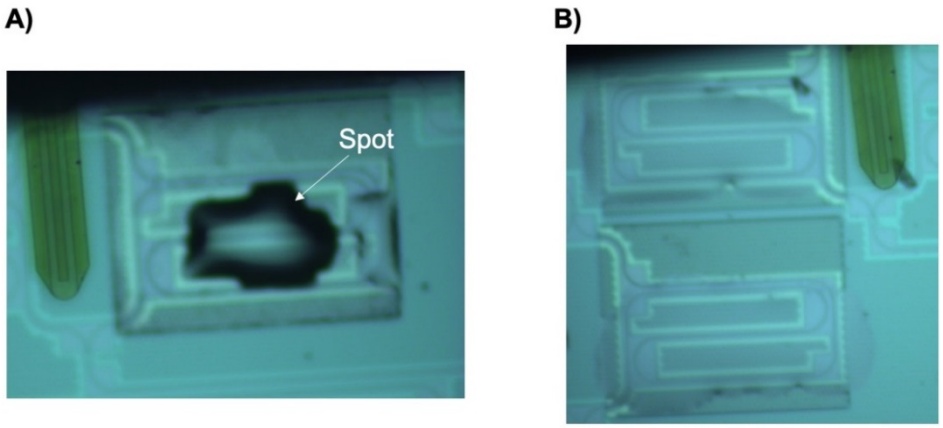

Figure 6.3. Photograph of the deposition of a spotting solution with 5% of glycerol in two photonic sensor chips previously activated **(A)** 2 min and **(B)** 5 min in the oxygen plasma.

Once the spotting conditions were optimised and considering all the above parameters, *in-situ* immobilisation was tested to check the effect of the surface activation (2 min) and the addition of glycerol (5%) in the immobilisation buffer. These testing experiments were performed using a monoclonal antibody against CRP (anti-CRP), previously employed in Chapter 4. A 50 μg/mL antibody concentration in PBS with 5% glycerol was physically adsorbed onto the photonic sensor surface, followed by a blocking step with BSA (10 mg/mL). A comparison of the immobilisation signals obtained in PBS with and without glycerol is shown in **Figure 6.4A**. Similar immobilisation signals were obtained in PBS (10.72 ± 0.43 nm) in comparison with the ones obtained by adding glycerol (9.98 ± 0.77 nm). Biosensor response was also evaluated by flowing a solution with 1 μg/mL of CRP. As can be observed in **Figure 6.4B**, the specific protein flow over the photonic sensor surface leads to a detection signal of 0.71 ± 0.03 nm, highly similar in comparison with the one previously obtained (0.79 ± 0.09 nm). Additionally, a t-test indicated that there were no statistically significant differences between both conditions (p-value >

0.05), and it can be concluded that the addition of the glycerol in the immobilisation buffer did not affect the immunoassay performance.

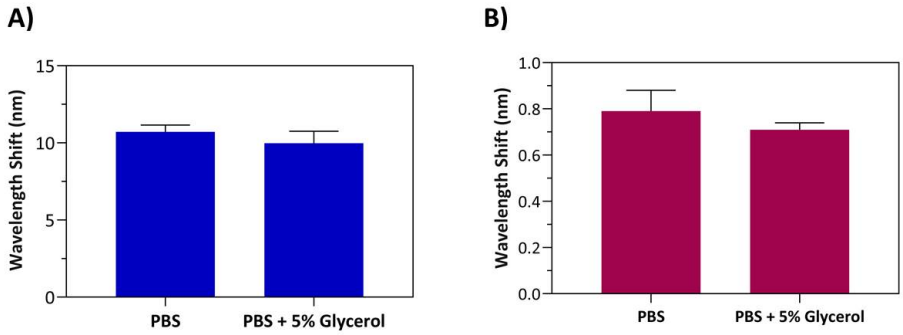

Figure 6.4. (A) Immobilisation signals of 50 µg/mL anti-CRP diluted in two different buffers: PBS and PBS with glycerol (5%). **(B)** Sensor response for the detection of 1 µg/mL of CRP over biofunctionalised sensor surface.

In our previous experiments, all the immobilisations were performed *in-situ,* monitoring the procedure in real-time. However, this is not possible when the antibody solution is deposited onto the sensor surface using Dip-Pen Nanolithography. For this reason, the evaluation of the multiplexed capabilities of our photonic sensor chips also involved the optimisation of *ex-situ* immobilisation. The incubation time (2 – 4 h and overnight), the temperature (room temperature, 4 and 37 °C), and the antibody concentration (50 – 500 µg/mL) had to be optimised. As a starting point, the same concentration of anti-CRP employed for *in-situ* immobilisation (50 µg/mL) was spotted in each of the six MZI sensors contained in the photonic sensor chip. After that, the photonic sensor chip was incubated for four hours at room temperature and 75 – 80% humidity, rinsed with Milli-Q water, and dried under N_2 gas. Subsequently, the photonic sensor chip was introduced into the microfluidic cartridge and placed in the POC platform employing PBS as a running buffer. After leaving the PBS flowing over the sensor surface for 15 min, the blocking step was carried out by injecting a BSA (10 mg/mL) solution. Unfortunately, when the specific protein (1 µg/mL CRP) was flowed over the sensor surface, a negligible signal was obtained (see **Figure 6.5A**).

This result suggested that the antibody concentration employed was not enough for an *ex-situ* immobilisation, or the incubation time was too short. For this reason, a higher antibody concentration (250 µg/mL) was spotted in each MZI sensor and incubated for four hours at room temperature. After the blocking step, a solution with 1 µg/mL of CRP was flowed over the sensor surface in PBS buffer. As can be observed in **Figure 6.5B**, the deposition of higher antibody concentration leads to a clear sensor response of 0.16 ± 0.03 nm. These signals were significantly higher than those obtained from immobilising the antibody using in-flow conditions, suggesting that the antibody concentration influenced the biorecognition event.

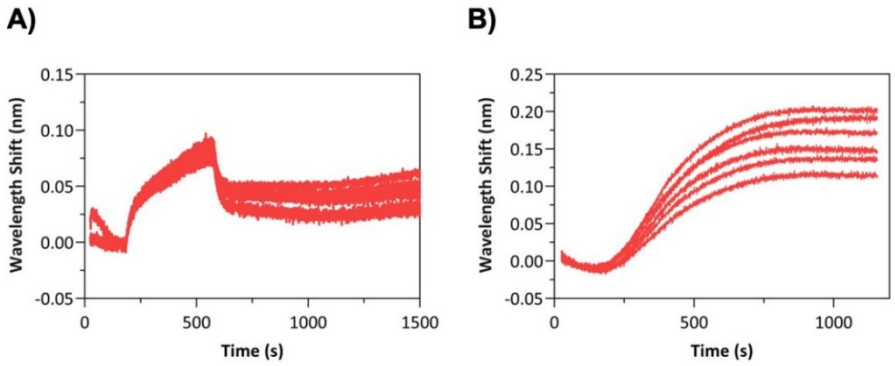

Figure 6.5. Sensorgrams showing the response to the injection of 1 µg/mL of CRP over a sensor surface immobilised with **(A)** 50 µg/mL of anti-CRP incubated for four hours, and **(B)** 250 µg/mL of anti-CRP incubated for four hours.

The assessment of the biosensor capabilities to specifically and simultaneously detect different biomarkers was carried out. Two specific antibodies, one against CRP and the other against LAM, were spotted in different MZI sensors. As shown in **Figure 6.6A** two MZI sensors were immobilised with anti-LAM and the remaining sensors with anti-CRP. As can be observed in **Figure 6.6B**, after the injection of 1 µg/mL of CRP in PBS, the MZI sensor biofunctionalised with the anti-CRP shows an increase in the signal (0.19 ± 0.06 nm). Meanwhile, those biofunctionalised with the anti-LAM resulted in no background signal. The same behaviour was observed after the injection of LAM (1 µg/mL)

with a response for the specific antibodies, and a negligible signal for the MZI sensor biofunctionalised with anti-CRP. These results demonstrate the absence of cross-signals between sensors and the possibility of performing simultaneous detection of a panel of TB biomarkers as a proof-of-concept for our novel POC biosensor platform.

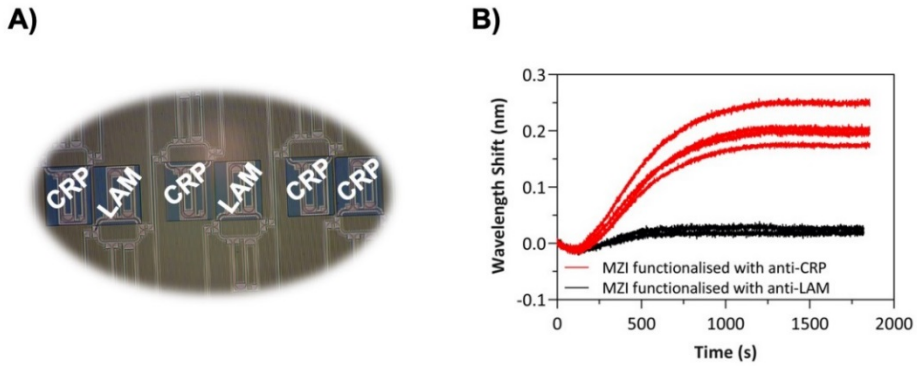

Figure 6.6. (A) Photograph of the MZI sensors showing that two specific antibodies, one against CRP and the other against LAM, were spotted in a specific MZI. **(B)** Real-time sensor response to the flow of 1 µg/mL of CRP over a sensor surface functionalised with two specific antibodies.

6.4. Conclusions

In this Chapter, we have demonstrated a preliminary proof-of-concept of the POC biosensor platform multiplexed capabilities for the simultaneous detection of a panel of TB biomarkers. In order to carry out the multiplex detection, DPN was used to spot different antibody solutions in the six-sensor array. The main advantage of employing DPN is reducing the bioreceptor amount required to cover the MZI sensors. Hence, this technique would be especially relevant for biosensor mass-production because it implies a significant reduction in the reagent cost compared with *in-situ* immobilisation.

Several parameters related to DPN were optimised for the specific deposition of antibody solution in each of the six MZI sensors and some of the parameters affecting ex-situ immobilization directly. In the case of

antibody solution deposition, the glycerol percentage, plasma activation time, and cantilever size were optimised to create a droplet that completely covered each MZI sensor without interfering with the adjacent ones. In the case of ex-situ immobilisation optimisation, different antibody concentrations and incubation times were tested. Using the optimised parameters, DPN allowed the immobilisation of anti-CRP in four MZI sensors and immobilisation of anti-LAM in the other two MZI sensors of the photonic sensor chip. After flowing each of the corresponding antigens (CRP and LAM), preliminary results demonstrate the possibility of performing multiplexing analysis.

These results are very promising, but there are still some parameters related to *ex-situ* immobilisation which need to be improved, such as the concentration of the antibody, the incubation time, and the environmental conditions. All these optimisations will allow the simultaneous detection of a panel of six TB biomarkers (LAM, ESAT-6, CFP-10, Ag85B, and MPT64) in a single urine sample in less than 20 minutes. Taken together, this will imply a significant improvement in the sensitivity and specificity of the current diagnostic techniques for TB diagnosis.

General conclusions and future perspectives

General conclusions and future perspectives

This Doctoral Thesis describes a novel point-of-care (POC) biosensor platform and demonstrates its applicability for the rapid diagnostics of Tuberculosis. The novel POC platform uses a photonic sensor chip based on a highly sensitive Mach-Zehnder Interferometer transducer with an on-chip spectral filter. The required elements for light coupling and optical readout are integrated in a prototype instrument, which allows real-time monitoring, data processing and the control of fluid injection over the sensor surface. My contribution to the POC development was focused on the sensor chip and prototype evaluation, sensor biofunctionalisation and, the full POC biosensor development (including complete assay development, characterisation and validation) for the final application of detecting active TB in real patient samples.

The main general conclusions that can be drawn from this thesis work are the following:

- The novel POC biosensor platform has been fully characterised to evaluate its potential for biosensing purposes. Several solutions with different refractive indices were evaluated achieving a bulk sensitivity of $(3.25 \pm 0.58) \times 10^{-6}$ RIU in the range of the reported MZI sensors. Furthermore, it demonstrates the excellent performance and reproducibility of the photonic sensor chips and the POC platform.

- An extensive exploration of different functionalisation strategies was performed to be able to attach specific antibodies to the photonic sensor surface. Initially, the use of N_3-silane was the preferred option because vapour-phase deposition was made at wafer-scale and could be performed after finalising the fabrication procedure. However, copper-free click chemistry showed a low yield in the antibody immobilisation, causing a weak antigen detection signal. Other options were evaluated, including APTES

silanization and physical adsorption. Both strategies showed higher antibody immobilisation and analyte detection signals. However, due to regeneration incompatibilities observed with the covalent binding through APTES chemistry and the waveguide material, there was no advantage in using covalent binding instead of physical adsorption. Therefore, physical adsorption was chosen as the preferred option in terms of sensitivity, reproducibility and simplicity in the procedure.

- The selected biofunctionalisation strategy was applied for the detection of LAM (17 kDa), CFP-10 (10 kDa), ESAT-6 (6 kDa), MPT64 (30 kDa), and Ag85B (40 kDa) biomarkers, which are important *M. tuberculosis*-derived antigens for TB diagnosis. The strategy was based on the direct and label-free antigen detection in unprocessed urine, previously immobilising the corresponding antibody and producing an antofouling sensor surface. After a thoughtful optimisation, LODs of 0.475 ng/mL for LAM, 35.68 ng/mL for CFP-10, 39.12 ng/mL for ESAT-6, 6.67 ng/mL for MPT64, and 11.92 ng/mL for Ag85B, respectively, were achieved. Despite the high sensitivity obtained for the selected panel of TB biomarkers in undiluted urine, there is no available information in the literature about the concentration range of each protein in the urine of patients with active TB.

- The POC biosensor platform was validated for LAM detection with clinical samples from TB patients and healthy donors. For the first time, it was successfully applied to the detection of TB regardless of HIV co-infection surpassing one of the main limitations of commercially available urine-based LAM tests. The results showed an excellent correlation with those obtained with current TB diagnostic methods, demonstrating high sensitivity (100%) and specificity (95%).

- The multiplexed capabilities of the novel POC biosensor platform for the simultaneous detection of a panel of TB biomarkers were explored as a proof-of-concept. Preliminary results demonstrated the capacity of the photonic sensor chip to analyse two biomarkers (LAM and CRP) in the same patient sample simultaneously in less than 20 minutes. Besides, the photonic sensor chip design allowed the analysis of up to six different biomarkers.

These promising results, if validated in larger clinical studies, could have important diagnostics implications taking into account the advantages added to the POC biosensor platform in comparison with the fastest method recommended by WHO. The advantages of the novel POC platform, including low-cost, single-use, user-friendliness, results in 15 minutes, no requirement of qualified personnel, and no need for special laboratory infrastructure, make this novel POC platform an outstanding candidate for in-situ use during routine check-ups in developing countries.

Future improvements may be directed to overcome some of the drawbacks of the additive immunoassay, finding and optimising a compatible biofunctionalisation protocol for the covalent binding of the antibodies. This could be solved by changing the technique for the production of the waveguide material (Si_3N_4) of the MZI sensors, from PECVD to LPCVD, which renders in more compact and high-refractive index Si_3N_4 material. The LPCVD Si_3N_4 is fully compatible with silanisation and regeneration protocols as we have widely demonstrated in our BiMW interferometric sensors. Also, further optimisations should be performed to demonstrate the capabilities of the POC platform for the simultaneous detection of a six TB biomarker panel in a single urine sample. Taken together, this will imply a significant improvement in the sensitivity and specificity of the current diagnostic techniques for TB diagnosis.

In conclusion, this Doctoral Thesis represents a significant contribution to the TB diagnosis field, demonstrating the enormous

potential of a novel POC biosensor platform for clinical diagnosis. Furthermore, it opens the door for use in the rapid detection of other infectious diseases and for its application in other fields, such as environmental monitoring and food analysis.

Annex A

Real-time and label-free SARS-CoV-2 detection by an interferometric biosensor

The work described in this Annex was carried out during my PhD within the frame of CoNVat H2020 European Project. The aim of the project was the development of a point-of-care device for the rapid detection of the novel coronavirus (SARS-CoV-2) in real samples. The point-of-care was based on the Bimodal Waveguide Interferometers (BiMW) functionalised with selective antibodies for the virus recognition. To test the nanophotonic device for the intact virus identification, a pseudovirus carrying the SARS-CoV-2 Spike (S) protein was used to optimise the immunoassay parameters.

A. Real-time and label-free SARS-CoV-2 detection by an interferometric biosensor

A.1. Introduction

On 31 December 2019, first reports of patients with unknown pneumonia in Wuhan City (China) were announced, being finally linked to a new causative infectious agent identified on 9 January by the Chinese Centre for Disease Control and Prevention (CDC).[233] Since then, the novel Severe Acute Respiratory Syndrome Coronavirus 2 (SARS-CoV-2), which causes coronavirus disease 2019 (COVID-19), has massively spread worldwide, obligating WHO to declare it as a pandemic. To date (October 2020), more than 39 million laboratory-confirmed cases with over 1 million deaths have been reported globally.[234]

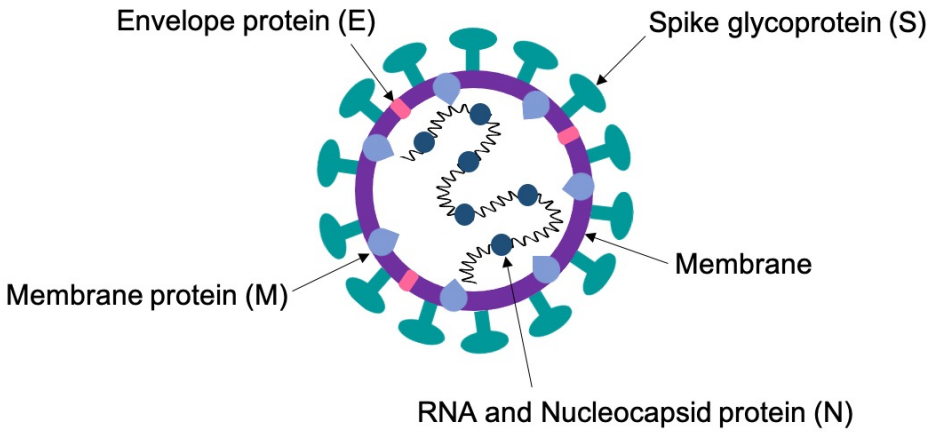

Figure A.1. Structure of SARS-CoV-2.

SARS-CoV-2 is an enveloped virus with single-stranded RNA, belonging to the betacoronavirus genera in the family *Coronaviridae*. As can be observed in **Figure A.1**, it has four major structural proteins, including spike (S), envelope (E), membrane (M), and nucleocapsid (N).[235] Among them, spike is a trimetric glycoprotein that plays an essential role in the infection, mediating the binding of the viral particles to host surface cellular receptors.[236] S protein comprises two functional

subunits: S1 subunit that contains the receptor-binding domain (RBD), which directly binds to the host cell receptor angiotensin-converting enzyme 2 (ACE 2), and S2 subunit, which is responsible for the membrane fusion.[237]

SARS-CoV-2 virus is transmitted from person to person through airborne droplets or aerosols, fomite, and close contact, primarily affecting the respiratory system. Moreover, a range of clinical manifestations have been observed, including fever, dry cough, fatigue, loss of taste or smell, headache, and in more severe cases, the infection can lead to respiratory failure, acute respiratory syndrome, septic shock, and multiorgan failure. However, there are also asymptomatic individuals with SARS-CoV-2 infection. This is one of the main challenges in the fight against COVID-19 because patients who never develop symptoms or who have not yet developed symptoms are able to spread the disease.[238]

The current gold standard for the diagnosis of COVID-19 is based on molecular tests such as reverse transcription PCR (RT-PCR), where specific sequences of the viral nucleic acid are amplified and detected from nasopharyngeal swabs samples.[239] This methodology offers high specificity and sensitivity,[240] due to the large volume of nucleic acid produced during amplification. However, the test involves expensive equipment and reagents, requires specialised laboratories and well-trained staff, and is often time-consuming mainly due to the transportation of the samples to centralised laboratories. There are also serological tests, which enable the monitoring of the humoral immune response generated during the infection through the identification of antibodies (IgM and IgG) in blood samples. However, this approach is used mainly for prevalence or contact tracing investigation and is not currently considered for diagnostic purposes.[241,242]

Complementary to molecular tests are rapid antigen tests. These tests allow the rapid and direct detection of the intact virus or fragments through the recognition of specific structural proteins of the virus (i.e.,

spike or nucleocapsid proteins in SARS-CoV-2).[239] For example, a lateral flow test Panbio™ COVID-19 Ag Rapid Test Device (Abbott, US) is commercially available since September 2020 for the detection of SARS-CoV-2 nucleocapsid protein in 15 minutes from a nasopharyngeal sample. The test has shown a high sensitivity (91.4%) and specificity (99.8%) determined by Abbott analyses, and more studies are underway.[243] Some studies have revealed that this test is only reliable during the first seven days after the onset of the symptoms.[244] Thus, there is still an urgent need to develop highly sensitive and specific POC biosensor platform for the rapid diagnosis of COVID-19.

Biosensors are one of the preferred options to develop these antigen tests, as these devices can offer straightforward, rapid, portable, and low-reagent consumption analyses with high sensitivity and selectivity.[239] Herein, we propose the use of our highly sensitive photonic biosensor based on bimodal waveguide interferometers (BiMW).[108] This design has already demonstrated numerous advantages over conventional methods, such as unprecedented sensitivity, rapid, label-free, and real-time monitoring. All the above benefits of the BiMW biosensor make this device an ideal candidate to identify individuals who are infected with SARS-CoV-2 and prevent further spreading. For instance, the BiMW platform has already been employed for the specific detection of relevant bacteria pathogens, being capable of detecting *E. coli* at extremely low concentrations (LOD of 4 CFU/mL) in human ascitic fluid in 25 min using a direct immunoassay.[245]

Within the framework of a new EU project (CoNVat), we are developing a POC biosensor for the rapid detection of the intact SARS-CoV-2 in human samples (mainly saliva). The detection strategy consists of a direct immunoassay that employs a highly specific antibody produced against the Spike protein and which does not need of any additional labelling or amplification steps.

A.2. Materials and methods

A.2.1. Chemical reagents and buffer composition

Organic solvents (acetone, ethanol, and methanol), hydrochloric acid, and nitric acid were purchased from Panreac (Barcelona, Spain). Triethoxysilane polyethylene glycol carboxylic acid (Silane-PEG-COOH, 600 Da) was supplied by Nanocs (New York, US). Reagents for carboxylic acid activation (N-(3-dimethylaminopropyl)-N'-ethylcarbodiimide hydrochloride (EDC) and N-hydroxysulfosuccinimide (sulfo-NHS)), and all reagents used for buffer preparation were provided by Sigma-Aldrich (Steinheim, Germany).

The buffers employed were the following: phosphate buffer saline (PBS; 10 mM Na_2HPO_4, 1.8 mM KH_2PO_4, 2.7 mM KCl and 137 mM NaCl, pH 7.4), PBST (PBS with different concentrations of Tween 20, pH 7.4), MES buffer (0.1 M 2-(N-morpholino)ethanesulfonic acid (MES), pH 5.5), acetate buffer (10 mM pH 5.0), ethanolamine hydrochloride (1 M, pH 8.5). Milli-Q water was employed for all the buffer preparation.

A.2.2. Biological reagents

Monoclonal antibodies against S1 subunit (anti-S1 mAb), polyclonal antibodies against S1 subunit (anti-S1 pAb), chimeric monoclonal antibodies against RBD (anti-RBD chAb), and chimeric polyclonal antibodies against RBD (anti-RBD pAb) were purchased from Sino Biological Europe GmbH (Germany). Recombinant S1 protein, RBD, and N protein were also provided by Sino Biological Europe GmbH (Germany). Human C-Reactive Protein (CRP) and Interleukin 6 (IL6) were acquired from BBI Solutions (UK) and Abyntek Biopharma (Spain), respectively.

Vesicular Stomatitis Virus (VSV) with the SARS-CoV-2 spike protein, VSV-ΔG-S, and without the spike protein, VSV-ΔG-G, (serving

as a control with the glycoprotein of VSV) was kindly provided by Dr. Ron Geller (University of Valencia).

A.2.3. Bimodal waveguide sensor

The BiMW sensor chip (3 cm x 1 cm; Figure 2A) was fabricated in silicon nitride (Si_3N_4) at wafer-scale in a cleanroom facility, as previously described.[108] Each chip integrates an array of 20 independent bimodal waveguides sensors. The working principle of the BiMW sensor relies on the evanescent wave principle, as previously described. (**Figure A.2**). In brief, light from a polarised diode laser (λ = 660 nm; P = 120 mW; Hitachi, Japan) is first confined through the waveguide core in a single (fundamental) mode. This fundamental mode is coupled into a bimodal section after a certain distance through a step junction that allows the first propagating mode appearance. These two modes travel across the sensing area and exit the waveguide. The evanescent field of the waveguide decays within the external medium and is altered by any change occurring close to the surface. This principle is exploited for sensing purposes. A sensing window is opened along the waveguide bimodal section, where the bioreceptors are immobilised, and the detection take places. Therefore, any refractive index change in this area, such as the one induced by the binding (or detachment) of any molecule, affects the propagating modes and results in an interferometric phase shift ($\Delta\varphi$) between the two modes, modifying the intensity distribution at the sensor chip output. The intensity is recorded by a two-sectional photodetector (Hamamatsu Photonics, Japan) and processed through an acquisition card. An all-optical phase modulation method previously developed is applied transforming the interference signal into a linear one able to continuously quantify the phase shifts between both modes. A fluidic system to ensure the liquid circulation to the sensing area is incorporated. It includes the following components: a five-channel polydimethylsiloxane (PDMS) microfluidic cell (channel dimensions = 1.25 mm wide x 500 µm height) that seals to the sensor chip, a syringe pump (New Era; New York, US) to guarantee continuous flow rate of a running buffer, and a 6-port injection valve

(VICI; Texas, US) that allows the sequential loading of the sample loop (100 µL) and injection of the different solutions.

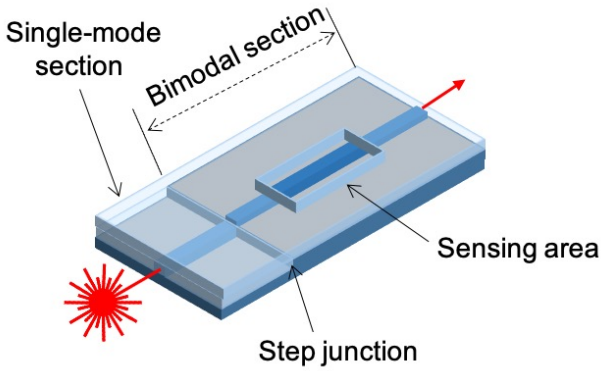

Figure A.2. Schematic representation of a Bimodal Waveguide Interferometer.

A.2.4. Surface functionalisation

Before surface functionalisation, the sensor chips were consecutively sonicated for 5 min in acetone, ethanol, milli-Q water, and 10 min in methanol/HCl 1:1 (v/v) to remove organic contamination. They were then rinsed with water, and dried with a nitrogen stream. A layer of active hydroxyl group was generated onto the sensor surface by using oxygen plasma (Electronic Diener; Ebhausen, Germany) for 5 min at 45 sccm gas flow, followed by immersion in a 15% HNO_3 solution at 75 °C for 25 min. After rinsing generously with water and drying under N_2 flow, the sensor chip was immediately functionalised with silane-PEG-COOH, following a previously described protocol.[245] Briefly, the sensor chip was incubated with the silane solution (25 mg/mL in ethanol absolute/water 95:5 (v/v)) for 2 h at 4 °C. After the incubation, the sensor chip was sequentially rinsed with ethanol and water, and dried with a nitrogen stream. Finally, the sensor chip was subjected to a high-temperature curing process by placing it in a conventional autoclave for 90 min at 121 °C and a pressure of 1.5 bars.

A.2.5. Antibody covalent immobilisation

The silanised sensor chip was placed on the experimental setup for the *in-situ* immobilisation of the corresponding antibody through the covalent binding of the carboxylic groups introduced on the sensor chip surface and the free amino groups of the antibody. The carboxyl groups were activated by flowing a solution with 0.2 M EDC/0.05 M sulfo-NHS in MES buffer (0.1 M, pH 5.5) at 20 µL/min over the sensor surface. A solution of the antibody was injected at a flow rate of 10 µL/min. The remaining unreacted activated groups were deactivated with an ethanolamine solution (1 M, pH 8.5) for 2 minutes at 20 µL/min. Milli-Q water was used as the running buffer during the immobilisation step and was then switched to the corresponding working buffer.

A.2.6. Direct immunoassay performance

The corresponding concentration of the analysed protein or pseudotype virus (100 µL) was injected over the biofunctionalised sensor surface at a constant flow rate ranging from 5 to 25 µL/min. Calibration curves were obtained by evaluating different concentrations in triplicate in PBS or PBST with different Tween 20 concentrations.

A.2.7. Data analysis

Data were analysed using Origin 8.0 (OriginLab, US) and GraphPad Prism 8 (GraphPad Software, US). Calibration curves were plotted as mean and standard deviation (Mean ± SD) of the acquired biosensor response ($\Delta\varphi$) *versus* the analysed concentration logarithm. The data were fitted to an exponential growth model.

A.3. Selection of biorecognition element

The BiMW biosensor is based on the label-free evanescent field sensing principle. Therefore, specific bioreceptor elements must be immobilised on the sensor surface in such way that SARS-CoV-2 viruses can be selectively recognised and captured. The most important factors to

take into account to achieve accurate and reliable label-free detection are: (i) the use of high affinity and specific bioreceptors, and (ii) a stable and robust bioreceptor immobilisation on the sensor surface. The first step for the biosensor development and optimisation involves the selection of the most appropriate biorecognition elements and the evaluation of the affinity and selectivity for the antigen.

The external spike (S) protein of SARS-CoV-2 was selected as thetarget for the intact virus recognition (**Figure A.3**). A set of different commercial antibodies were acquired, including polyclonal (pAb), monoclonal (mAb), and chimeric monoclonal antibodies (chAb) targeting both the S protein and the RBD domain. In addition, the recombinant S protein (S1 subunit) and RBD antigen were purchased for the bioassay optimisation.

The BiMW sensor chip was first functionalised with a Silane-PEG-COOH and directly placed into the experimental setup for further *in-situ* covalent binding of the antibodies (**Figure A.3**). Carboxylic groups provided by the silane were activated employing the well-known EDC/sulfo-NHS chemistry, highly reactive to primary amine groups accessible in the lysine residues of antibodies. After antibody binding, a robust covalent amide bond is formed, and remaining activated groups can be blocked with ethanolamine.

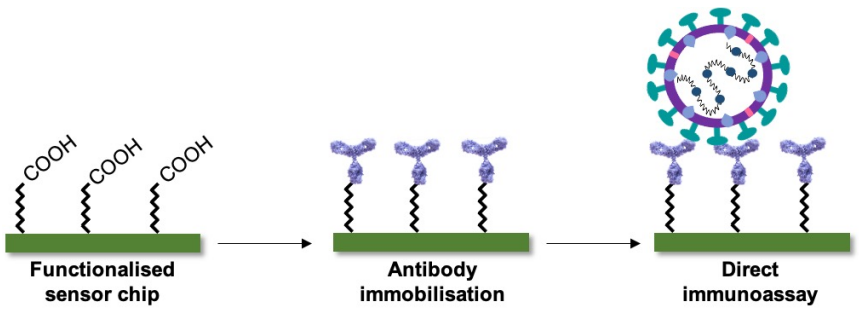

Figure A.3. Representation of the three main steps in the development of a direct immunoassay for the detection of SARS-CoV-2: functionalisation of the sensor chip with silane-PEG-COOH; covalent immobilisation of the specific antibody against Spike protein and direct detection of the SARS-CoV-2.

The affinity and specificity of anti-S1 and anti-RBD antibodies for the recombinant SARS-CoV-2 antigens were evaluated. Moreover, non-specific proteins (SARS-CoV-2 N protein, IL-6, and CRP) were employed as negative controls. As shown in **Figure A.4**, some degree of non-specific binding of both N protein and IL6 were observed, which might be attributed to cross-reactivity with a His-Tag residue, because in the case of unspecific proteins without a His-Tag (i.e., CRP protein), it was not observed. A polyhistidine-tag consists of six or nine histidine residues added at the N or C-terminal of the protein, and is extensively used for recombinant protein purification. In our case, His-Tag is present in the control proteins as well as in the immunogens employed for antibody production. However, this cross-reactivity would not be relevant when addressing the direct measurement of the intact virus samples. In terms of affinity and detection sensitivity, the best initial results were obtained for the chimeric monoclonal anti-RBD and monoclonal anti-S1 antibodies. Therefore, they were selected as initial biological receptors for the optimisation of the SARS-CoV-2 virus detection.

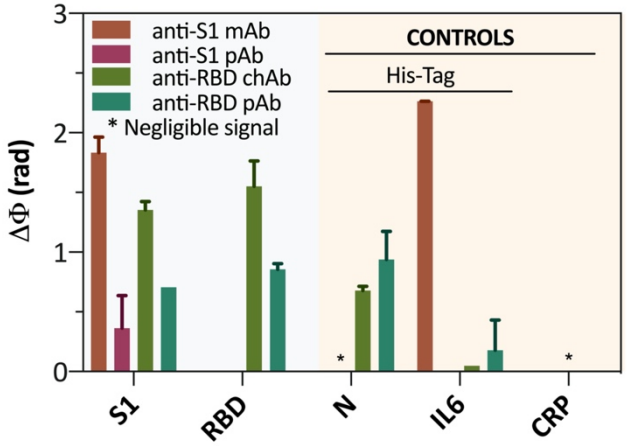

Figure A.4. Comparison of the affinity and specificity of anti-S1 and anti-RBD antibodies against recombinant antigens (S1 and RBD), and non-specific proteins as controls (N, IL6, and CRP). Each column represents the mean ± SD of duplicates.

A.4. Real-time and label-free pseudovirus detection in buffer

Direct capture and detection of intact coronavirus on the BiMW biosensor was evaluated and optimised employing a non-replicative vesicular stomatitis virus (VSV) coated with the same SARS-CoV-2 Spike protein (VSV-ΔG-S; **Figure A.5A**). A control pseudovirus expressing the major virulence factor of VSV, the glycoprotein (G) (VSV-ΔG-G; **Figure A.5B**) was also evaluated. The pseudovirus samples were produced at the University of Valencia in cell culture and provided in PBS solution at moderate titters (≈ 10^6 focus forming units per mL (FFU/mL)). These pseudoviruses can be safely used to evaluate the BiMW biosensor without the need for biosafety level 3 (BSL3) containment because they are not able to replicate inside host cells.[246]

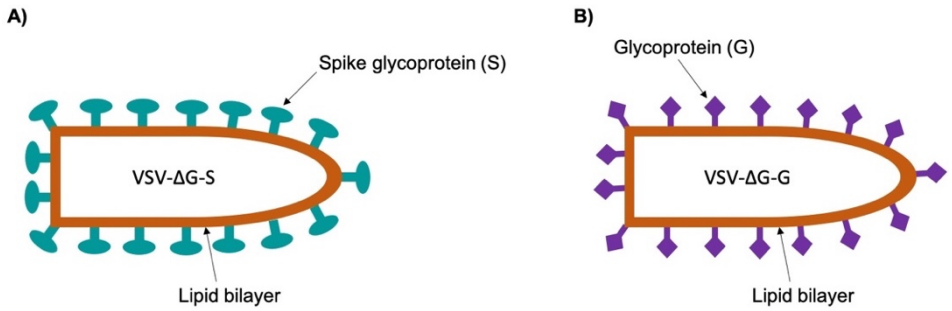

Figure A.5. Structure of **(A)** VSV-ΔG-S and **(B)** VSV-ΔG-G.

The direct detection of the pseudovirus using the previously selected antibodies (anti-S1 mAb and anti-RBD chAB) was initially tested to evaluate the affinity of the commercial SARS-CoV-2 antibodies for the pseudovirus. An antibody concentration of 10 μg/mL was immobilised onto the BiMW sensor surface. A specificity study of the bioassay using VSV-ΔG-G, which does not express any SARS-CoV-2 antigen on the pseudovirus surface, was firstly tested. The sensorgrams shown in **Figure A.6** confirm that both antibodies exclusively recognised the specific SARS-CoV-2 S protein expressed in the VSV pseudovirus with no cross-reactivity with the one expressing the glycoprotein (VSV-ΔG-G) not

present in the SARS-CoV-2 envelope. It also demonstrates that the immobilised antibodies selectively captured virus particles, and unspecific binding to the sensor surface was not observed.

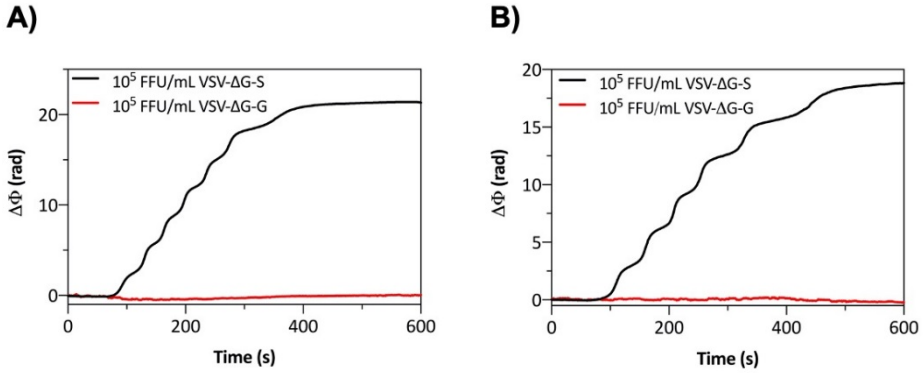

Figure A.6. (A) Real-time sensorgram showing the response to a sample with 10^5 FFU/mL of VSV-ΔG-S (black line) and 10^5 FFU/mL of VSV-ΔG-G (red line) into a sensor previously coated with 10 µg/mL of anti-S1 mAb and **(B)** 10 µg/mL of anti-RBD chAb.

As shown in **Figure A.7A**, the biosensor response in real-time exhibits a correlation between the analysed concentration and the response. Calibration curves obtained by flowing over the sensor surface several VSV-ΔG-S concentrations ranging from 10^2 to 10^5 FFU/mL for the two analysed antibodies are plotted in **Figure A.7B**. Similar sensor responses were obtained when using anti-S1 mAb and anti-RBD chAb, with estimated LODs of 1057 and 348 FFU/mL, respectively. Because anti-RBD chAb showed superior performance, this antibody was selected for further optimisation for the direct pseudovirus detection.

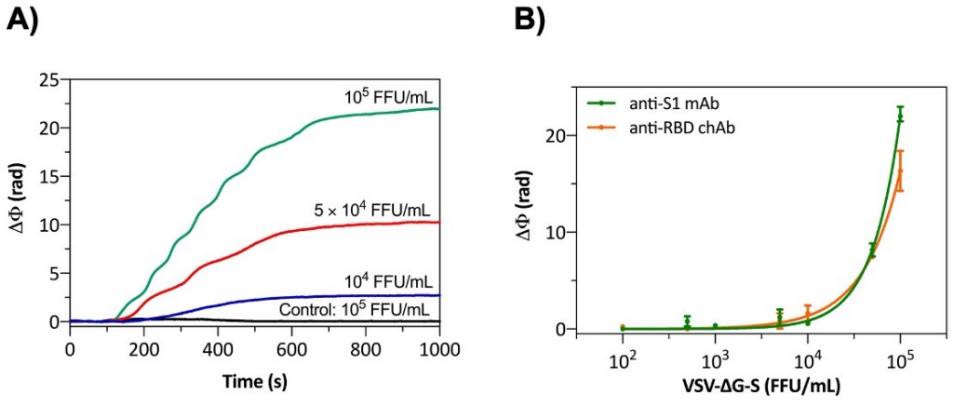

Figure A.7. (A) Real-time sensorgram showing the response to different VSV-ΔG-S concentrations in comparison to the control (VSV-ΔG-G) flowed over a sensor surface biofunctionalised with anti-S1 mAb. **(B)** Calibration curve obtained for the detection of VSV-ΔG-S using two different antibodies: Green curve: anti-S1 mAb and orange curve: anti-RBD chAb. Each concentration represents the mean ± SD of duplicates.

The intact pseudovirus assay parameters were then optimised to enhance the detection sensitivity. Firstly, the flow rate employed to deliver the pseudovirus sample over the sensor surface was evaluated. A concentration of 10^4 FFU/mL of VSV-ΔG-S was flowed at different flow rates ranging from 5 to 25 µL/min. As observed in **Figure A.8A**, the flow rate affects the pseudovirus recognition, demonstrating that lower flow rates increase virus contact time with the sensor surface, favouring the detection signal. The best results were obtained with a flow rate of 5 µL/min, although it increased the time-to-result to 45 minutes. In order to be able to obtain more data in less time, we decided to perform all the experiments at 10 µL/min with a time-to-result of 20 min.

The buffer composition was also evaluated, comparing the sensor response for 10^4 FFU/mL of VSV-ΔG-S diluted in PBS and PBST with different percentages of Tween 20 (0.05, 0.1 and 0.50%). As shown in **Figure A.8B**, the addition of different Tween 20 amounts to the PBS buffer had a positive effect on the sensor response compared with PBS without Tween. However, when performing the calibration curves with the three different percentages of Tween 20 (**Figure A.8C**), high Tween 20

percentages were observed to negatively affect the sensitivity of the intact pseudovirus detection. PBST 0.1% demonstrated higher sensitivity values (LOD = 71 FFU/mL) and was therefore selected for further optimisations.

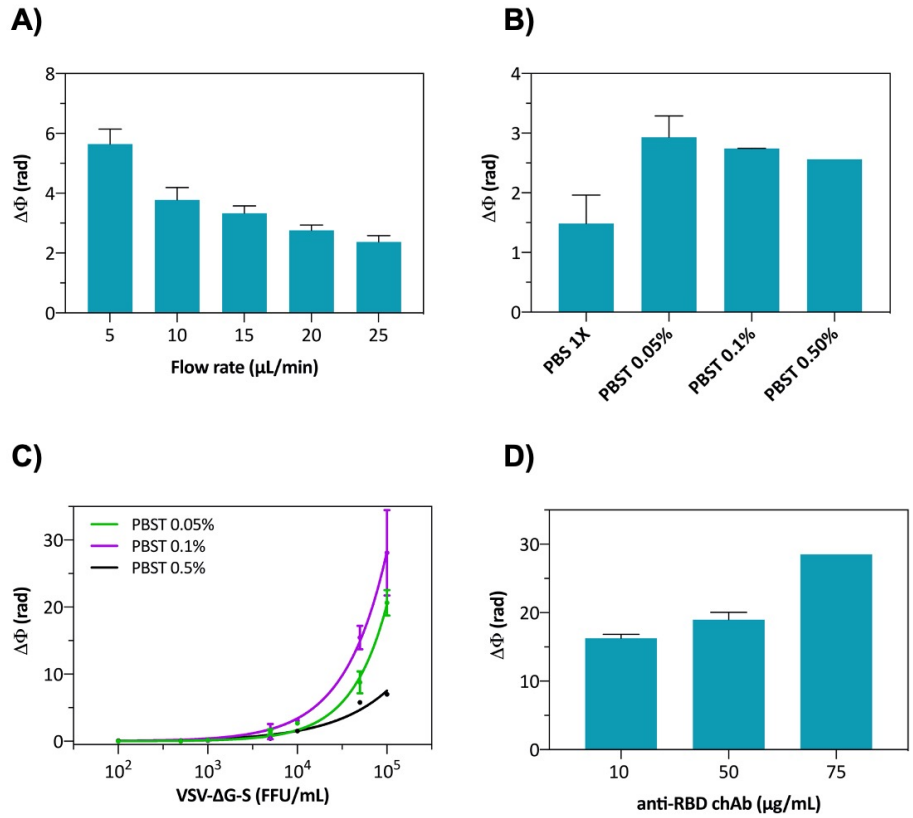

Figure A.8. (A) Flow rate effect in the detection of 10^4 FFU/mL VSV-ΔG-S. **(B)** Signals obtained in the detection of 10^4 FFU/mL VSV-ΔG-S in different buffers: PBS and PBST with 0.05 – 0.50% of Tween 20. **(C)** Calibration curve obtained for the detection of VSV-ΔG-S using three different buffers. **(D)** Immobilisation signals obtained at different antibody concentrations (10 – 75 µg/mL anti-RBD chAb). Each sensor response represents the mean ± SD of duplicates.

Finally, the antibody density was also evaluated, taking into account all the above-optimised parameters. Different anti-RBD chAb concentrations (ranging from 10 to 75 µg/mL) were immobilised on the sensor surface. As shown in **Figure A.8D**, an increasing sensor response was observed by increasing the antibody concentration. However, after evaluating different pseudovirus concentrations and plotting the different

calibration curves, higher sensitivity was obtained with 50 μg/mL of anti-RBD, and PBST 0.1% as running buffer at 10 μL/min, achieving a **LOD of 46 FFU/mL**. Furthermore, this biofunctionalisation strategy provided a highly stable antibody immobilisation on the sensor surface, enabling the biosurface regeneration at the laboratory level with NaOH 10 mM for multiple repeated measurement cycles (up to 12 cycles) with excellent reproducibility. The sensitivity levels obtained with the BiMW biosensor would assure reliable diagnostics of COVID-19 infection since the typical viral load in nasopharyngeal or saliva samples is between 10^4 – 10^7 virus particles/mL.[247–249] Furthermore, we proved that the BiMW biosensor is capable of quantification of the viral load in a one-step assay in less than 20 minutes.

A.5. Inactivation effect

Although the initial evaluation and optimisation study was performed with VSV-ΔG-S pseudovirus with promising results, the analytical sensitivity and specificity might vary when attempting to detect the real SARS-CoV-2 virus. In order to address this, we decided to test the effect of inactivated procedures in SARS-CoV-2 samples. The Instituto Nazionale per le Malattie Infettive (INMI, Italy) provided samples of UV-inactivated SARS-CoV-2 virus (UV for 15 min; λ = 254 nm) and Aix-Marseille Université (AMU, France) provided two samples of thermally inactivated SARS-CoV-2, one at 95 °C for 10 min and another at 56 °C for 30 min. All samples were proven to be non-infectious before shipping to our lab, so they did not have to be used in BSL3 facilities.

The characterisation of the inactivated samples was carried out to check whether the inactivation process affected the virus external protein structure, hindering the antibody recognition of the S protein. This was especially important for the heat-inactivated samples, as high temperatures might denaturalise the proteins, while UV treatment is supposed only to affect the viral RNA. Three virus samples inactivated with different processes were analysed at the Transmission Electron Microscopy (TEM)

service of the Autonomous University of Barcelona (UAB). As shown in **Figure A.9A**, in the UV-inactivated samples, the virus structure was well defined. However, it was difficult to find whole virus particles in both thermally inactivated samples (**Figure A.9B**,**C**), and the identified viral particles did not show a clear structure. Moreover, the inactivated samples looked dirty, meaning that many proteins and other biological material were dissolved in the sample. This study confirms that the heat-inactivation of virus samples is not an effective treatment for intact virus detection.

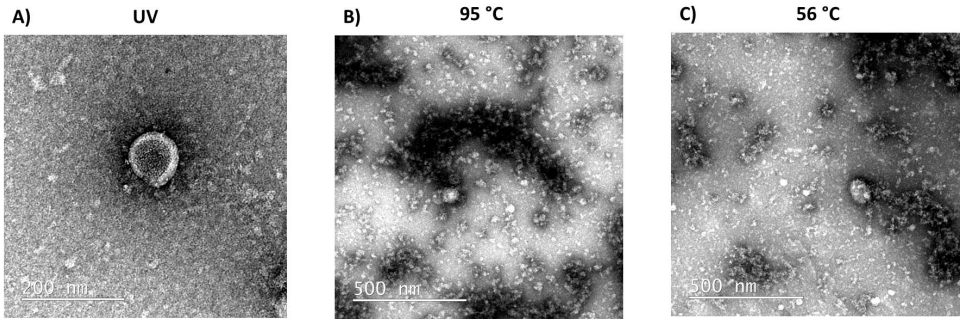

Figure A.9. TEM images of three SARS-CoV-2 inactivation processes: **(A)** UV for 15 minutes, **(B)** 95 °C for 10 min, and **(C)** 56 °C for 30 min.

Nonetheless, the effect of the different inactivation protocols in antibody recognition was evaluated. To this end, the same inactivation procedures (UV, 95 °C and 56 °C) were performed on three aliquots of the VSV-ΔG-S pseudovirus and compared with the detection performance of a non-treated aliquot. As shown in **Figure A.10** and as expected, the UV-inactivated pseudovirus detection was comparable to the non-treated samples, whereas there was a significant decrease in the signal for the two heated samples. The main conclusion from this study is that only the UV-inactivation protocol is reliable for intact virus detection studies since the thermal procedures seriously affect the virus structure, reducing the accuracy of the assay.

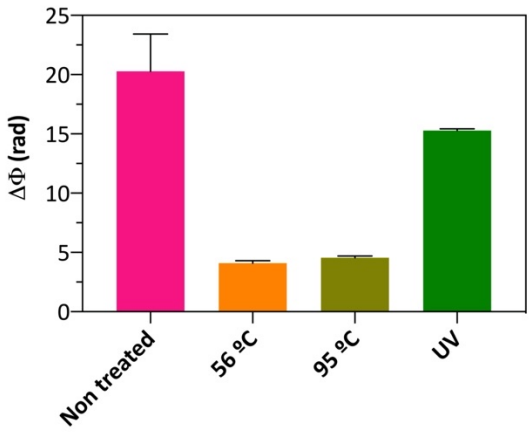

Figure A.10. Effects of the inactivation processes in the detection of 10^5 FFU/mL of VSV-ΔG-S samples with the BiMW biosensor.

A.6. Conclusions and future perspectives

We have developed a biosensor for the direct, label-free, and real-time detection of a pseudovirus coated with the SARS-CoV-2 Spike protein. This pseudovirus offers a highly similar virus particle to the novel coronavirus, so the detection optimisation can be carried out without the SARS-CoV-2 viruses. Consequently, the BiMW biosensor capabilities to directly detect intact viruses was tested without the need for a BSL3 infrastructure. The strategy consisted of a direct immunoassay where chimeric monoclonal antibodies against the SARS-CoV-2 Spike protein were linked covalently to the BIMW sensor surface. Several parameters affecting the immunoassay sensitivity were optimised, achieving a LOD of 46 FFU/mL with a short time-to-result (less than 20 min). The assay LOD was well below the standard viral load in nasopharyngeal or saliva samples. Furthermore, the effect of different protocols to inactivate SARS-CoV-2 revealed that UV-inactivated samples are the only ones that enable a reliable intact virus detection. In contrast, thermal procedures seriously affected the virus structure denaturalising the envelope proteins and reducing the assay accuracy.

The current work focused on evaluating and optimising the detection of the virus in complex biofluids (cell culture media and saliva). Results show that non-specific adsorptions of matrix components present in both samples can produce false-positive sensor signals that must be controlled and minimised. Different blocking agents with anti-fouling properties are currently being tested as well as buffer additives and sample dilutions. The main objective will be to analyse real clinical samples with minimum pre-treatment so that our photonic POC biosensor can be operated by non-specialised personnel in decentralised settings.

Annex B

Real-time monitoring of fenitrothion in water samples with a photonic immunosensor

The work described in this Annex was carried out during my PhD within the frame of a Retos-Colaboración Project in collaboration with the petrol company CEPSA (DIONISOS Project). This project shows the potential of the silicon photonics interferometers in other fields, such as environmental monitoring. Particularly, we employed our own technology of Bimodal Waveguide Interferometer (BiMW) for the rapid, label-free, and specific quantification of an organophosphate insecticide, fenitrothion, directly in tap water samples.

B. Real-time monitoring of fenitrothion in water samples with a photonic immunosensor

B.1. Introduction

Fenitrothion [O,O-Dimethyl O-(3-methyl-4-nitrophenyl) phosphorothioate] (FN) (**Figure B.1**) is a powerful organophosphate (OP) insecticide used in large quantities because of its efficacy, cost-effectiveness, and availability.[250] This type of pesticide is extensively employed in agriculture and everyday household applications worldwide. Some of FN's applications include the control of a wide range of insects in cereals, rice, fruits, vegetables, store grains, and other crops, as well as in public health programs to control flies, mosquitoes, and cockroaches.[251,252] Uncontrolled use of these organophosphate insecticides represents a serious risk to the environment, as they are potentially toxic for non-target organisms, including humans. Their principal mechanism of action is based on the inhibition of the acetylcholinesterase enzyme involved in nerve impulse transmission.[250,253] Additionally, several studies have demonstrated that they are also carcinogenic,[254] cytotoxic,[255] mutagenic, genotoxic,[256,257], and immunotoxic.[258] The toxicity of FN has been tested in mice, rats, Guinea pigs, and rabbits showing an oral lethal dose ranging between 250 and 870 mg/kg.[259,260] In humans, the Food and Agriculture Organization of the United Nations, together with WHO established an acceptable daily intake of 0.005 mg/kg.[261] Some of the chronic symptoms include general fatigue, headache, loss of memory, anorexia, nausea, and muscular weakness, among others.[260] For this reason, FN, in particular, was recently banned in Europe and the United States; however, it is still used in Central and South America, Asia, and Africa.[259,262,263] Because of the toxicity of OP pesticides, including FN, the continuous monitoring in a wide range of samples such as soil, sediments, air, water, and food is crucial.[264,265] Indeed, one of the most common causes of human exposure is through drinking-water supplies due to pesticide leaching from contaminated soils to the groundwater.[266] To protect human health, WHO has published international standards for drinking water by publishing

Guideline Values (GV) for different pesticides. Although a GV for FN has not been established (judging by the occurrence of the pesticide at concentrations well below those of health concern), a health-based value (HBV) of 8 μg/mL can be calculated based on toxicity studies.[267,268]

Conventional methods for detecting FN and other OP pesticides include liquid and gas chromatography,[269–271] mass spectroscopy,[272,273] capillary electrophoresis,[274] and ELISA.[275,276] These methods are highly sensitive for the determination of OP pesticides. However, these techniques require laborious and time-consuming sample preparation and the use of bulky laboratory equipment and trained staff, making them unsuitable for in-field testing. To facilitate continuous routine analysis in real scenarios, the implementation of analytical tools that overcome these limitations and provide equal or even better levels of sensitivity are still in demand. Biosensors are one of the preferred options, as these devices can offer straightforward, rapid, portable, and low-sample and reagents consumption designs. Several examples have been reported for the specific detection of FN. For instance, Ensafi et al. and Qi et al. employed an electrochemical sensor functionalised with graphene and metal oxide nanostructured material, achieving a LOD of 0.45 and 2.20 ng/mL, respectively, for FN in water samples.[277,278] Furthermore, Kant functionalised a SPR biosensor with similar nanostructures, reaching a LOD of 11.40 ng/mL in the case of FN in environmental samples.[279]

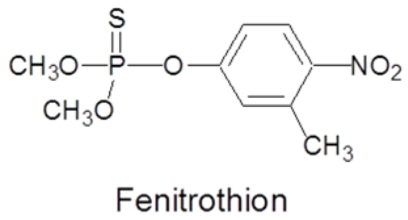

Figure B.1. Structure of fenitrothion.

We herein propose the use of a highly sensitive photonic biosensor based on BiMW.[108] This design has already demonstrated numerous

advantages over conventional methods, such as unprecedented sensitivity, rapid, label-free, and real-time monitoring. In addition, BiMW sensor chips are fabricated with standard microelectronics technology, enabling a reduction in fabrication costs and therefore, in the final analysis price. All the above advantages of the BiMW biosensor make this device an ideal candidate for on-site monitoring of OP pesticides. This BiMW device has already been employed for several clinical[109,245,280,281] and environmental[132,282] applications with the evaluation of real samples, for example, for the specific detection of the biocide Irgarol 1051 in seawater, combining high specific custom-designed antibodies against the selected contaminant and the extreme sensitivity of the BiMW sensor.[132]

In this work, we have optimised and validated the BiMW biosensor device to identify and quantify FN in tap water samples. The detection strategy consisted of a competitive immunoassay by employing a highly specific monoclonal antibody (non-commercial) produced against FN. The optimisation of the immunoassay was focused on two aspects: firstly, on improving the analytical parameters compared with routine detection methods and state-of-the-art biosensors, and secondly, on avoiding any previous sample pre-treatment or extraction for directly analysing real water samples.

B.2. Materials and methods

B.2.1. Chemical reagents and buffer composition

Organic solvents (acetone, ethanol, methanol, and ethanol absolute), hydrochloric acid, and nitric acid were purchased from Panreac (Spain). Triethoxysilane polyethylene glycol carboxylic acid (Silane-PEG-COOH, 600 Da) was supplied by Nanocs (US). Reagents for carboxylic acid activation (N-(3-dimethylaminopropyl)-N'-ethylcarbodiimide hydrochloride (EDC) and N-hydroxysulfosuccinimide (sulfo-NHS)), (3-Aminopropyl)triethoxysilane (APTES), N,N-Diisopropylethylamine (DIPEA), p-Phenylene diisothiocyanate (PDITC), anhydrous toluene, pyridine, N,N-Dimethylformamide (DMF), 1,4-dioxane, fenitrothion (FN)

analytical standard, and all reagents used for buffer preparation were provided by Sigma-Aldrich (Germany).

The buffers employed were the following: phosphate buffer saline (PBS; 10 mM Na_2HPO_4, 1.8 mM KH_2PO_4, 2.7 mM KCl and 137 mM NaCl, pH 7.4), PBST (PBS with different concentrations of Tween 20, pH 7.4), carbonate buffer (0.1 M, pH 9.5), MES buffer (0.1 M 2-(N-morpholino)ethanesulfonic acid (MES), pH 5.5), acetate buffer (10 mM pH 5.0), ethanolamine hydrochloride (1 M, pH 8.5). Milli-Q water was employed for all the buffer preparation.

B.2.2. Biological compounds

The bovine serum albumin conjugate (BSA-FN4C) and the monoclonal antibody (mAb) LIB-FN4C22 specific for FN were previously designed, synthesised and characterised by the Immunotechnology Group (Centro de Investigación e Innovación en Bioingeniería (Ci2B); Universitat Politècnica de València).

B.2.3. Bimodal waveguide sensor

Previously described in Annex A.

B.2.4. Surface biofunctionalisation

Previous to surface functionalisation, the sensor chips were consecutively sonicated for 5 min in acetone, ethanol, milli-Q water, and 10 min in methanol/HCl 1:1 (v/v), to remove organic contamination. They were then rinsed with water and dried with a stream of nitrogen. A layer of active hydroxyl group was generated onto the sensor surface using oxygen plasma (Electronic Diener; Germany) for 5 min at 45 sccm gas flow, followed by immersion in a 15% HNO_3 solution at 75 °C for 25 min. After rinsing generously with water and drying under N_2 flow, the sensor chip was immediately functionalised.

B.2.4.1 BSA-FN4C covalent immobilisation on Silane-PEG-COOH surface

The hydroxylated sensor chip was immediately incubated with a solution of Silane-PEG-COOH (25 mg/mL in absolute ethanol/water 95:5 (v/v)) for 2 h at 4 °C. After the incubation, the sensor chip was sequentially rinsed with ethanol and water, and dried with a nitrogen stream. Finally, the sensor chip was subject to a high-temperature curing process by placing it in a conventional autoclave for 90 min at 121 °C and a pressure of 1.5 bars.

The silanised sensor chip was placed on the experimental setup for the *in-situ* immobilisation of the BSA-FN4C conjugate through the covalent binding of the carboxylic groups introduced on the surface of the sensor chip and the free amino groups of the BSA carrier protein in the conjugate. The carboxyl groups were activated by flowing a solution with 0.2 M EDC/0.05 M sulfo-NHS in MES buffer (0.1 M, pH 5.5) at 20 µL/min over the sensor surface. A solution of BSA-FN4C conjugate was injected at a flow rate of 10 µL/min. The remaining unreacted carboxylic groups were deactivated with an ethanolamine solution (1 M, pH 8.5) for 2 minutes at 20 µL/min. Milli-Q water was used as the running buffer during the immobilisation step and was then switched to the corresponding working buffer.

B.2.4.2 BSA-FN4C covalent immobilisation on APTES surface

The hydroxylated sensor chip was immediately transferred into an anhydrous toluene solution with 1% (v/v) APTES and 0.3% (v/v) DIPEA for 1 h under an argon atmosphere. After the incubation, the sensor chip was sequentially rinsed with toluene and water, and dried with a nitrogen stream. Finally, the sensor chip was subject to a curing process by placing it in the oven at 110 °C for 1 h.

The silanised sensor chip was activated with a solution containing 20 mM of PDITC and 10% pyridine in DMF for 1 hour in darkness. Then, the

activated sensor chip was placed in the experimental setup for the *in-situ* immobilisation of the BSA-FN4C conjugate through the covalent binding of the amino groups introduced on the sensor surface and the free amino groups of the BSA carrier protein in the conjugate. A BSA-FN4C conjugate solution diluted in carbonate buffer (0.1 M, pH 9.5) was injected at a flow rate of 10 µL/min. Milli-Q water was used as the running buffer during the immobilisation step and was then switched to the corresponding working buffer.

B.2.5. Competitive immunoassay performance

Different stock solutions of FN (from 2.5 mM to 0.978 µM) were prepared in 1,4-dioxane and stored at 4 °C. Working standards were freshly prepared from each stock solution by a 1/500 dilution in the corresponding working buffer. The set of FN concentrations were pre-incubated for 10 min with a fixed concentration of antibody at room temperature. The mixture (100 µL) was injected over the biofunctionalised sensor surface at a constant flow rate of 20 µL/min. Calibration curves were obtained by assaying different FN concentrations (between 5 µM and 1.95 nM) by triplicate.

B.2.6. Matrix effect of tap water

The tap water was collected in Bellaterra (Spain) and stored at 4 °C. For the preparation of calibration curves, working standards were prepared in tap water, and (1:1) in PBST 20 mM 0.1% Tween 20 (PBST 2x) to match the same concentration range described above. This mixture was incubated for 10 min with the specific monoclonal antibody.

B.2.7. Accuracy study

To evaluate the accuracy of the assay, seven blind samples (S1 – S7) were prepared by a different researcher (blind samples for the analyst) by spiking tap water with known concentrations of FN. Samples were diluted (1:1) in PBST 2x and analysed as described above. Concentrations were

determined by interpolating from the PBST 0.05% standard curve. Accuracy was determined by applying the following equation:

$$\text{Accuracy (\%)} = \frac{[\text{FN}]_{\text{calculated}}}{[\text{FN}]_{\text{real}}} \times 100 \qquad \textbf{(B.1)}$$

B.2.8. Data analysis

Data were analysed using Origin 8.0 (OriginLab, US) and GraphPad Prism 8 (GraphPad Software, US). The acquired biosensor response was normalised by expressing the phase variation ($\Delta\varphi$) of each standard point as the percentage of the maximum response ($\Delta\varphi_{max}$). Calibration curves were plotted as mean and standard deviation (Mean ± SD) of normalised signal *versus* the logarithm of FN concentration. The data were fitted to a four-parameter logistic regression equation according to the following formula:

$$y = D + \frac{A-D}{1+\left(\frac{x}{C}\right)^{B}} \qquad \textbf{(B.2)}$$

where y is the biosensor response, x is the FN concentration, A is the asymptotic maximum corresponding to the signal in the absence of FN, B is the slope of the curve at the inflection point, C is the inflection point, equivalent to the half-maximal inhibitory concentration (IC_{50}), and D is the asymptotic minimum corresponding to the background signal. The LOD was calculated as the FN concentration corresponding to 90% of the signal. The working range was set as the interval between 20 and 80% of the normalised signal (IC_{20} – IC_{80}).

B.3. Optimisation of the immunoassay

The selection of the most suitable immunoassay detection format is highly dependent on the analyte properties. The key factors to consider are

the size, molecular weight, and the number of different epitopes (part of the structure recognised by the antibodies). In the case of evanescent wave biosensors, like the BiMW biosensor, the response depend explicitly on the mass changes induced on the sensor surface;[108] thus, the size of the analyte is the most critical aspect. For large analytes, direct or sandwich assays are the more appropriate formats. However, when small analytes (MW < 500 Da), such as fenitrothion (FN, MW = 277.23 Da), bind directly to the antibody, the induced changes of the refractive index are relatively very small for a direct quantification, limiting the sensitivity of the immunoassay. For this reason, an indirect competitive immunoassay is the preferred option (**Figure B.2B**). In the indirect competitive configuration, a competitor (BSA-FN4C) related to the target analyte (FN), which is also recognised by the specific antibodies (LIB-FN4C22), is covalently immobilised onto the sensor surface. A fixed concentration of the specific monoclonal antibody is incubated with different concentrations of the analyte in solution and after is flown over the sensor surface. The antibody recognises both the target and the immobilised antigen, which compete for its binding. Therefore, at higher FN concentrations in solution, a lower amount of antibody will bind to the sensor surface, and the resulting signal is inversely proportional to the analyte concentration.

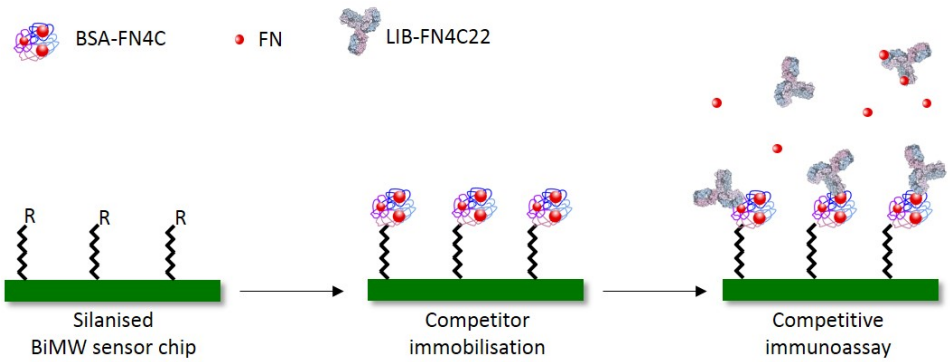

Figure B.2. Schematic representation of the three main steps in the development of a competitive immunoassay for the detection of FN: functionalisation of the sensor chip with a silane; covalent immobilisation of hapten-protein conjugate (BSA-FN4C competitor) and competition step with the sample containing a fixed concentration of antibody (LIB-FN4C22) and FN as target analyte.

As mentioned previously, biofunctionalisation is a critical step in the development of a biosensor, affecting the immunoassay performance directly. For this reason, two different biofunctionalisation protocols based on silane-PEG-COOH and APTES were evaluated.

On one side, a BiMW sensor chip was functionalised with a silane-PEG-COOH and directly placed in the experimental setup for further *in-situ* covalent bonding of the conjugate. Carboxylic groups provided by the silane were activated following the well-known EDC/sulfo-NHS chemistry. The pH of the buffer employed to prepare the BSA-FN4C solution can play a decisive role, especially in in-flow dynamic reactions as it can favour the local pre-concentration of the ligand on the surface through electrostatic interactions, therefore increasing the yield of the covalent coupling. This influence was studied by injecting several solutions of 10 μg/mL BSA-FN4C prepared in different immobilisation buffers adjusted at various pHs ranging from 4.0 to 7.4 (**Figure B.3A)**. As the acetate buffer 10 mM at pH 5.0 resulted in a higher accumulation of the protein conjugate on the surface (i.e., pH very close to the pI of BSA equal to 4.8), it was selected for the covalent immobilisation. In parallel, another BiMW sensor chip was functionalised with APTES followed by activation of the terminal amino groups with PDITC as a crosslinker. Subsequently, the sensor chip was placed in the experimental setup for the *in-situ* covalent immobilisation of the conjugate in carbonate buffer (pH 9.5).

A solution with 50 μg/mL of BSA-FN4C was covalently attached to sensor chips previously functionalised either with APTES or with silane-PEG-COOH to choose the optimal silanisation procedure. For this concentration, the higher immobilisation signals were obtained for the silane-PEG-COOH functionalisation ($\Delta\phi_{\text{silane-PEG-COOH}}$ = 84 rad, $\Delta\phi_{\text{APTES}}$ = 24 rad). A higher amount of BSA-FN4C covalently immobilised onto the sensor surface does not always imply better detection; therefore, the choice of the optimal functionalisation protocol was carried out by flowing

a solution with 1 µg/mL of the antibody in the absence of FN. The results had a similar average shift, but they were significantly more reproducible with the silane-PEG-COOH (SD = 0.39 ± 0.53; %CV = 7.39 ± 10.62) than with the APTES functionalisation (SD: 3.32 ± 2.06; %CV = 57.69 ± 22.41). Thus, silane-PEG-COOH was selected as the best candidate for further optimisation experiments.

After choosing the silanisation protocol, other parameters directly affecting the surface biofunctionalisation process and the immunoassay performance were evaluated (i.e., conjugate and antibody concentrations, and immunoassay buffer). The appropriate concentration of both BSA-FN4C and antibody were first selected following non-competitive assays (without FN). Two concentrations of BSA-FN4C (20 and 50 µg/mL) were immobilised onto the sensor surface. As expected, immobilisation signals showed an increasing tendency with a higher concentration (i.e., Δφ of 37 and 87 rad, respectively, see **Figure B.3B**). For each case, a set of different antibody concentrations ranging between 0.125 and 8 µg/mL were injected. As shown in **Figure B.3C**, a similar response for the same antibody concentration was obtained regardless of the conjugate concentration immobilised onto the sensor surface. The antibody concentration should guarantee a sufficient signal to allow a broad working range below non-saturation conditions. We did not reach signal saturation in the evaluated antibody range (see **Figure B.3C**), and the signals were very similar and high enough for both BSA-FN4C concentrations. Thus, to favour the competition, the lowest concentration of conjugate (20 µg/mL of BSA-FN4C) was selected in combination with an antibody concentration that induces a signal near 1 rad. This antibody signal is high enough, considering the signal-to-noise ratio of the experimental setup, to ensure FN detection at low concentrations. Accordingly, a concentration of 1 µg/mL of the antibody was selected for the immunoassay. We confirmed the specificity of the binding of the LIBFN4C22 antibody for the biofunctionalised sensor surface by testing a nonspecific mAb at the same concentration (1 µg/mL). As observed in **Figure B.3D**, this control antibody led to a negligible response,

demonstrating that the signal came solely from the specific recognition of the BSA-FN4C conjugate immobilised onto the sensor surface.

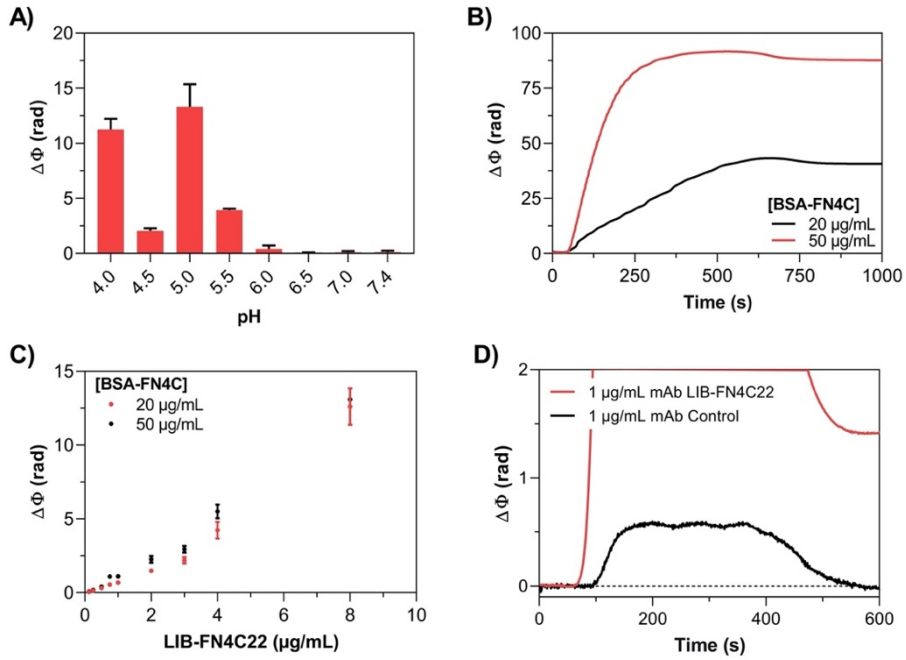

Figure B.3. (A) Preconcentration signals for BSA-FN4C (10 µg/mL) prepared in several buffers adjusted at different pHs (4.0 – 7.4). Each point represents the mean ± SD of duplicates. **(B)** Real-time sensorgrams showing the immobilisation of BSA-FN4C at 20 and 50 µg/mL. **(C)** Non-competitive curves obtained for LIB-FN4C22 antibody at different concentrations (0.125 – 8 µg/mL) with different BSA-FN4C-coated sensor chips ([FN4C-BSA] = 20 and 50 µg/mL). Each point represents the mean ± SD of duplicates. **(D)** Real-time sensorgrams for the detection of the specific mAb LIB-FN4C22 (red line) and a control mAb (black line) at 1 µg/mL.

The effect of the assay buffer composition on the immunoassayanalytical parameters (i.e., LOD, IC_{50}, and working range) was also evaluated. Particularly, PBS solutions with variable Tween 20 percentages (PBST, with 0.0125 – 0.75 % of Tween 20) were tested. Commonly, this surfactant agent is added to the immunoassays to improve the reproducibility among measurements and to prevent nonspecific adsorptions. To evaluate its effect during the competition, a set of three different FN concentrations (0, 0.25, and 2 µM) were studied. The three

FN concentrations allowed making a sweep of the complete analyte range: the first one being high enough to be close to the curve bottom limit (maximum inhibition, signal close to zero), the second one being in the dynamic range, and the third one providing the maximum signal (absence of FN).

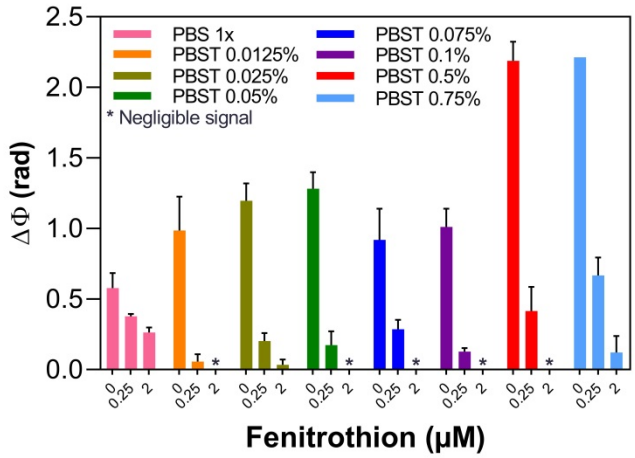

Figure B.4. Results obtained from the competitive immunoassay for different FN concentrations (0, 0.25, and 2 μM) pre-incubated with the antibody in different buffers: PBS and PBST with 0.0125 – 0.75% of Tween 20. [BSA-FN4C] = 20 μg/mL; [LIB-FN4C22] = 1 μg/mL (Each column represents the mean ± SD of duplicates).

Additionally, an initial pre-incubation of the antibody with each FN concentration during 10 min was fixed, following previous optimised immunoassays.[283] The results are shown in **Figure B.4**, where an evident influence of the Tween percentage in the immunoassay performance is appreciated. When comparing all the analysed ratios, the best results were obtained with PBST 0.05% and 0.5%. The highest maximum signal was observed with 0.5% and 0.75% of Tween but in this later case, no complete inhibition was observed at the highest FN concentration (2 μM). Besides these two cases, the conditions corresponding to 0.05% Tween showed the most promising results (i.e. high maximum signal around 1.5 rad, a total inhibition signal with high FN concentrations, and with a signal reduced more than half for a FN intermediate concentration). Thus, PBST

0.05% and PBST 0.5% were initially selected to perform a complete competitive assay.

Reusability of the biofunctionalised sensor surface, by disrupting LIB-FN4C mAb/BSA-FN4C interaction while maintaining the biorecognition layer intact, is one of the main advantages of biosensors over other bioanalytical methods, which can be especially useful for continuous automated *in-situ* monitoring in the environment. This can be achieved with changes in the pH or ionic strength of the media. In our case, the regeneration of the sensor surface was accomplished by introducing a NaOH 10 mM solution (**Figure B.5A**). The conditions were strong enough to guarantee the total disruption of the binding but mild enough to ensure high stability of the functionalised sensor surface for more than 120 cycles without significantly reducing the maximum antibody signal (**Figure B.5B**).

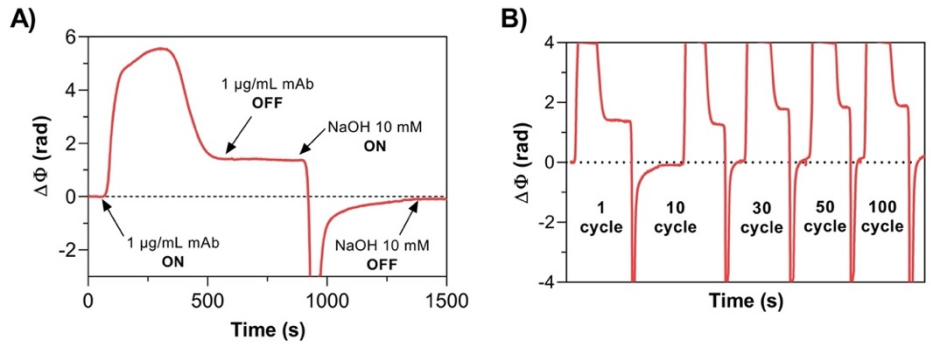

Figure B.5. (A) Real-time sensorgram representing antibody LIB-FN4C22 detection (1 µg/mL) and subsequent regeneration of the surface with NaOH 10 mM. **(B)** Real-time sensorgrams showing the detection of 1 µg/mL mAb LIB-FN4C22 throughout successive measurements and regeneration cycles in PBST 0.05%.

With all the above-selected immunoassay parameters, complete calibration curves were carried out with FN concentrations ranging from 1.95 nM to 5 µM diluted in the two selected buffers (PBST 0.05% and 0.5%). Samples were flowed over the BSA-FN4C coated surface after a pre-incubation of 10 minutes with a fixed concentration of LIB-FN4C22

antibody (1 µg/mL). As shown in **Figure B.6** and **Table B.1**, a clear influence of the Tween percentage in the immunoassay was observed. The PBST with ten times more concentrated Tween 20 (PBST 0.5% Tween), resulted in a significant worsening of the sensitivity of around one order of magnitude (both in the LOD and the IC_{50}). The main analytical parameters for each of the assays are summarised in **Table B.1**. According to these results, PBST 0.05% was finally selected for the evaluations. Under the selected conditions, a LOD and IC_{50} of 0.93 nM (0.26 ng/mL) and 5.88 nM (1.65 ng/mL) were reached, respectively and a linear working range was found between 1.84 and 18.74 nM (0.52 and 5.25 ng/mL). The CV for both intra-assays and inter-assays for the main analytical parameters were well-below 10 and 15%, respectively (see **Table B.2**), which are values commonly acceptable for bioanalytical methods.[182] These results corroborate the excellent reproducibility and low variability of the competitive immunoassay for the detection of FN.

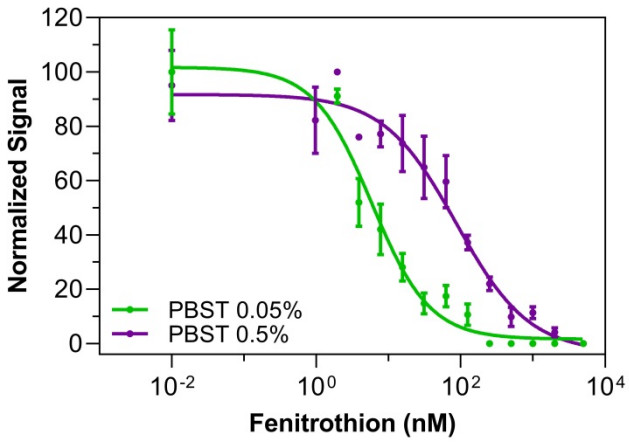

Figure B.6. Normalised standard calibration curves of a competitive immunoassay for FN detection in PBST 0.05% (green curve) and PBST 0.5% (purple curve). [LIBFN4C22] = 0.5 µg/mL; Each point represents the mean ± SD of three replicates.

Table B.1. Analytical parameters for the competitive immunoassay for FN in buffer and tap water (1:1).

	LOD (IC_{90}) (ng/mL)	IC_{50} (ng/mL)	Working Range ($IC_{80} - IC_{20}$) (ng/mL)	HillSlope
PBST 0.05%	0.26	1.65	0.52 – 5.25	-1.195
PBST 0.5%	1.91	24.4	4.89 – 122.3	-0.875
Tap water:PBST 2x (1:1)	0.29	1.71	0.56 – 5.17	-1.251

Table B.2. Intra-assay and inter-assay variability of the main analytical parameters for the competitive immunoassay in PBST 0.05%.

	Intra-assay[a]		Inter-assay[b]	
	Average ± SD	%CV	Average ± SD	%CV
IC_{50} (ng/mL)	1.59 ± 0.11	6.82	1.65 ± 0.06	3.74
LOD (ng/mL)	0.25 ± 0.01	5.84	0.26 ± 0.008	3.26
$\Delta\varphi_{max}$ (rad)	1.80 ± 0.02	1.11	1.81 ± 0.03	1.66
HillSlope	-1.15 ± 0.03	2.61	-1.20 ± 0.03	4.17

[a] Triplicates within the same biofunctionalised BiMW sensor chip.
[b] Triplicates with three different biofunctionalised BiMW sensor chips.

B.4. Analysis in tap water. Accuracy study

Widely used pesticides, including fenitrothion, have the potential to eventually contaminate natural waters and reach water systems, becoming harmful for humans and other organisms by ingestion or direct contact with them. The feasibility of using the developed immunosensor to analyse water samples was assessed using tap water. To evaluate matrix effects, 1 µg/mL of the mAb LIB-FN4C22 was prepared in tap water and injected over the sensor surface. Lower detection signals were observed in comparison with the ones obtained previously in buffer conditions (**Figure B.7**). This result reveals that some water parameters like pH, ionic

strength, or the concentration of certain compounds interfere in the assay performance. To correct this effect, samples were diluted 1:1 in PBST 2x (i.e., PBS 20 mM with 0.1% Tween 20). When monitoring the sensor response to the flow of tap water (1:1) in the absence of the antibody, a negligible signal was observed (**Figure B.7**) confirming the lack of any nonspecific adsorption. The same phase variation as in buffer conditions was obtained when the antibody in tap water was diluted 1:1 in PBST 2x (**Figure B.7**), indicating that buffered tap water did not affect the interaction of the antibody with the hapten immobilised on the sensor surface.

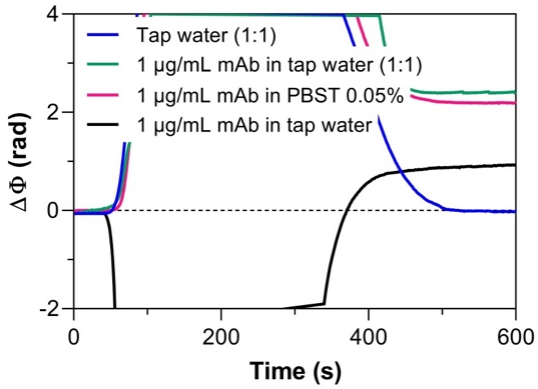

Figure B.7. Real-time sensorgrams showing the response to different solutions: tap water diluted 1:1 in PBST 2x 0.1% (blue line); tap water diluted 1:1 in PBST 2x 0.1% and [LIBFN4C22] = 1 µg/mL (pink line); PBST 0.05% and [LIBFN4C22] = 1 µg/mL (green line); undiluted tap water and [LIB-FN4C22] 1 µg/mL.

Tap water was spiked with different FN concentrations in the range from 1.95 nM to 5 µM. The samples were incubated for 10 minutes with a fixed concentration of the LIB-FN4C22 antibody (1 µg/mL) and diluted in PBST 2x before injection onto the BSA-FN4C coated sensor surface. As shown and compared in **Figure B.8** and **Table B.1**, calibration curves obtained in PBST 0.05% and tap water samples (1:1) exhibited non-significant differences concerning assay sensitivity. In particular, a LOD of 1.05 nM (0.29 ng/mL), an IC_{50} of 6.09 nM (1.71 ng/mL), and a working

range from 2.01 and 18.45 nM (0.56 to 5.17 ng/mL) were reached for FN detection in tap water samples.

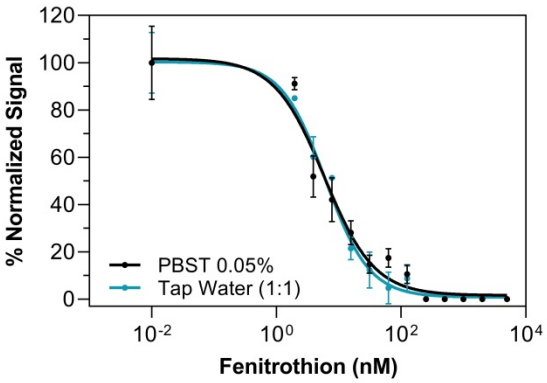

Figure B.8. Calibration curves for FN detection in PBST 0.05% (black) and tap water (1:1, blue). Each point represents the mean ± SD of three replicates.

The accuracy of our biosensor for the determination of the FN concentration was then evaluated with tap water samples fortified with FN within and far above the working range of the immunoassay. Seven blind samples (concentration unknown for the researcher performing the analysis) were prepared (S1 – S7). Before the injection over the sensor surface, all samples were diluted 1:1 in PBST 2x (or more if necessary, to fall within the dynamic range, as in the case of samples S1 and S2). The sensor response was monitored in real-time for each analysed sample, and the signal was interpolated in the calibration curve obtained for FN (**Figure B.8**). Recoveries and FN concentrations obtained by duplicate with the biosensor were calculated and listed in **Table B.3**. A good correlation was observed between FN concentrations obtained with the biosensor and the real concentration. Accuracy values indicate a slight overestimation (i.e., above 100%) except for the lowest concentration, which is around 80%. Overall, these values are within the accepted accuracy range between 80 – 120%. These results confirm the high accuracy and feasibility of the developed label-free biosensor to analyse FN in water in less than 20 minutes without the need for any sample pre-treatment.

Overall, we have established a biosensor-based immunoassay for the detection of FN in water with an analytical performance slightly better than some examples reported in the literature using a conventional ELISA (LOD of 0.30 or 0.90 ng/mL) and electrochemical sensors (LOD of 0.45 and 2.20 ng/mL), employing different immunoreagents.[275–278] Furthermore, the high sensitivity and specificity of our methodology for the determination of FN in water samples meet the health-based value imposed for drinking water by WHO (8 µg/mL) and also the minimum amount set by Australia, as the most restrictive value currently established at worldwide level (7 µg/mL).[268,284]

Table B.3. Accuracy study performed with blind samples with the immunosensor

Samples	Concentration (nM)			Accuracy (%)
	Spiked		Measured[a]	
	nM	ng/mL	Mean ± SD	
S1	200	55.91	208.6 ± 3.89	104.3
S2	75	20.97	73.26 ±5.23	97.7
S3	20	5.59	20.29 ± 0.41	101.4
S4	15	4.19	17.18 ± 0.46	114.5
S5	10	2.80	11.07 ± 0.22	110.7
S6	5	1.40	3.94 ± 0.01	78.8
S7	1	0.28	< LOD	-

[a] Average of two measurements

B.5. Conclusions

We have developed a biosensor for the straightforward, label-free, and real-time detection of fenitrothion in tap water based on a highly sensitive interferometric detection. The strategy consisted of a competitive immunoassay format that combined the covalent immobilisation of a BSA conjugate carrying fenitrothion hapten molecules with specific

monoclonal antibodies against the insecticide. The binding of the antibody to the coated sensor surface was inversely proportional to the fenitrothion concentration in the sample. Several parameters affecting the immunoassay sensitivity were optimised, achieving a LOD of 1.05 nM (0.29 ng/mL) and IC_{50} of 6.09 nM (1.71 ng/mL) in tap water with short time-to-result (20 minutes), which are sufficient for the health-based value calculated for drinking water by WHO (8 μg/mL). Furthermore, the biosensor accuracy was evaluated with blind tap water samples showing an excellent correlation with spiked fenitrothion concentrations.

Given these promising results, further steps will include the integration of the biosensor in a portable and miniaturised platform with the aim of pushing the technology from laboratory prototypes to compact devices able to perform continuous in-field monitoring of water quality without sample pre-treatment.

List of publications

- **PUBLICATIONS**

A low-cost integrated biosensing platform based on SiN nanophotonics for biomarker detection in urine
D. Martens, P. Ramirez-Priego, M.S. Murib, A.A. Elamin, A. B. Gonzalez-Guerrero, M. Stehr, F. Jonas, B. Anton, N. Hlawatsch, P. Soetaert, R. Vos, A. Stassen, S. Severi, A. Stassen, S. Severi, W. Van Roy, R. Bockstaele, H. Becker, M. Singh, L.M. Lechuga and P. Bienstman
2018 Analytical Methods, 10, 3066-3073

Label-Free and Real-Time Detection of Tuberculosis in Human Urine Samples Using a Nanophotonic Point-of-Care Platform
P. Ramirez-Priego, D. Martens, A.A. Elamin, P. Soetaert, W. Van Roy, R. Vos, B. Anton, R. Bockstaele, H. Becker, M. Singh, P. Bienstman and L.M. Lechuga
2018 ACS Sensors, 3 (10), 2079-2086

Coherent Silicon Photonic Interferometric Biosensor with Inexpensive Laser Source for Sensitive Label-Free Immunoassays
J. Leuermann, V. Stamenkovic, P. Ramirez-Priego, A. Sanchez-Postico, A. Fernández-Gavela, C.A. Chapman, R.C. Bailey, L.M. Lechuga, E. Perez-Inestrosa, D. Collado, R. Halir and I. Molina-Fernández
2020 Optics Letters (*revisions submitted*)

Real-time monitoring of fenitrothion in water samples using a silicon nanophotonic biosensor
P. Ramirez-Priego, M.C. Estévez, H.J. Díaz-Luisravelo, J.J. Manclús, A. Montoya and L.M. Lechuga
2020 ACS Environmental Science & Technology (*submitted*)

- **CONFERENCES**

Direct quantification of exosomes from tumor cell cultures by bimodal waveguide interferometry
A.B. González-Guerrero, P. Ramírez, J. Maldonado and L.M. Lechuga
EUROPT(R)ODE XIII – Conference on Optical Chemical Sensor and Biosensors, Graz (Austria). March 20th – 23rd 2016 **Poster presentation**

Development of a low-cost Point-of-care test for Tuberculosis detection
P. Ramírez, D. Martens, P. Bienstman, M. Singh, A.A. Elamin, W. Van Roy, R. Vos, P. Soetaert, B. Anton, H. Becker and L.M. Lechuga
VIII International Congress on Analytical Nanoscience and Nanotechnology (NyNA), Barcelona (Spain). July 3rd – 5th 2017 **Poster presentation – 1st PRIZE POSTERS AWARD**

Development of a low-cost Point-of-care test for Tuberculosis detection
B. Anton, P. Ramírez, D. Martens, P. Bienstman, M. Singh, A.A. Elamin, W. Van Roy, R. Vos, P. Soetaert, L.M. Lechuga and H. Becker.
21st International Conference on Miniaturized Systems for Chemistry and Life Sciences (μTAS2017), Savannah (US). October 22nd – 26th 2017 **Poster presentation**

Abbreviations and acronyms

Ab	Antibody
AFM	Atomic Force Microscope
Ag85B	Antigen 85B
AlereLAM	Alere Determine™ Tb Lam Ag
ANOVA	A One-Way Analysis of Variance
anti-85B	Monoclonal IgG Antibody Against 85B
anti-CEH-ECH	Polyclonal IgG Antibody Against ESAT-6 And CFP-10
Anti-CRP	Monoclonal IgG Antibody Against C-Reactive Protein
Anti-LAM	Monoclonal IgG Antibody Against Lipoarabinomannan
Anti-MPT64	Polyclonal IgG Antibody Against MPT64
Anti-RBD chAb	Chimeric Monoclonal Antibody against RBD
Anti-RBD pAb	Chimeric Polyclonal Antibody against RBD
anti-S1 mAb	Monoclonal Antibody against S1 Subunit
Anti-S1 pAb	Polyclonal Antibody against S1 Subunit
APTES	3-Aminopropyltriethoxy silane
AWG	Arrayed Waveguide Grating
BiMW	Bimodal Waveguide Interferometer
BSA	Bovine Serum Albumin
BSA-FN4C	Bovine Serum Albumin Conjugate
BSL3	Biosafety Level 3
CD4	Cluster of Differentiation 4
CFP-10	10 kDa Culture Filtrate Protein
CMOS	Complementary Metal-Oxide-Semiconductor
COVID-19	Coronavirus Disease 2019
CRP	C-Reactive Protein
CV	Coefficient of Variation
DBCO-PEG$_4$-NHS	Dibenzylcyclooctyne Polyethylene Glycol N-Hydroccinimide Ester

DPN	Dip-Pen Nanolithography
EDC	(N-(3-Dimethylaminopropyl)-N'-Ethylcarbodiimide Hydrochloride
ELISA	Enzyme-Linked Immunosorbent Assay
ESAT-6	6 kDa Early Secretory Antigenic Target
FFU	Focus Forming Units
FN	Fenitrothion
FujiLAM	Fujifilm SILVAMP TB LAM
GV	Guideline Values
HBV	Health-Based Value
HCl	Hydrochloric acid
HEPES	4-(2-Hydroxyethyl)Piperazine-1-Ethanesulfonic Acid
HIV	Human Immunodeficiency Virus
HNO_3	Nitric Acid
IC_{50}	Half-Maximal Inhibitory Concentration
IgG	Immunoglobulin
IL6	Interleukin 6
LAM	Lipoarabinomannan
LIB-FN4C22	Monoclonal Antibody Specific for Fenitrothion
LOD	Limit of Detection
LPCVD	Low-Pressure Chemical Vapour Deposition
mAb	Monoclonal antibody
MeOH	Methanol
MES	2-(N-Morpholino)Ethanesulfonic Acid
MPT64	Immunogenic Protein MPT64
Mtb	*Mycobacterium tuberculosis*
MZI	Mach-Zehnder Interferometer
N	Nucleocapsid Protein
N_3-PEG-SH	Azide-Peg-Thiol
N_3-silane	11-Azidoundecyltrimethoxysilane

OP	Organophosphate
pAb	Polyclonal antibody
PBS	Phosphate Buffer Saline
PBST	Phosphate Buffer Saline With Tween 20
PCR	Polymerase Chain Reaction
PDITC	P-Phenylene Diisothiocynate
PECVD	Plasma-Enhanced Chemical Vapour Deposition
pI	Isoelectric Point
PLL-g-PEG	Poly(L-Lysine)-Graft-Poly(Ethylene Glycol) Co-Polymer
POC	Point-of-Care
R^2	Coefficient of Determination
RBD	Receptor-Binding Domain
RI	Refractive Index
RIU	Refractive Index Units
ROC	Receiver Operating Characteristic
S	Spike Protein
SARS-CoV-2	Severe Acute Respiratory Syndrome Coronavirus 2
Si_3N_4	Silicon Nitride
Silane-PEG-COOH	Triethoxysilane Polyethylene Glycol Carboxylic Acid
SLED	Superluminescent diode
SPP	Surface Plasmon Polaritons
SPR	Surface Plasmon Resonance
Sulfo-NHS	N-Hydroxysulfosuccinimide
TB	Tuberculosis
TPP	Target Priority Profiles
UV	Ultraviolet
VSV-ΔG-G	Vesicular Stomatitis Virus expressing a Glycoprotein
VSV-ΔG-S	Vesicular Stomatitis Virus coated with SARS-Cov-2 Spike Protein

WHO	World Health Organisation

Bibliography

1. Adigun, R. & Singh, R. *Tuberculosis*. *StatPearls* (StatPearls Publishing, 2020).

2. Chai, Q., Zhang, Y. & Liu, C. H. Mycobacterium tuberculosis: An adaptable pathogen associated with multiple human diseases. *Frontiers in Cellular and Infection Microbiology* **8**, 158 (2018).

3. Delogu, G., Sali, M. & Fadda, G. The biology of mycobacterium tuberculosis infection. *Mediterranean Journal of Hematology and Infectious Diseases* **5**, 2013070 (2013).

4. World Health Organisation. Global tuberculosis report 2019. (2020).

5. Kiazyk, S. & Ball, T. Latent tuberculosis infection: An overview. *Canada Commun. Dis. Rep.* **43**, 62–66 (2017).

6. Fogel, N. Tuberculosis: A disease without boundaries. *Tuberculosis* **95**, 527–531 (2015).

7. Pai, M. *et al.* Tuberculosis. *Nat. Rev. Dis. Prim.* **2**, 1–23 (2016).

8. Andrews, J. R. *et al.* Risk of progression to active tuberculosis following reinfection with Mycobacterium tuberculosis. *Clin. Infect. Dis.* **54**, 784–791 (2012).

9. Joanne Willey, L. S. & Woolverton, C. J. *Prescott's microbiology*. (McGraw-Hill, 2017).

10. Kaufmann, S. H. How can immunology contributed to TB control. *Nat. Rev. Immunol.* **1**, 20–30 (2001).

11. Lin, P. L. *et al.* Sterilization of granulomas is common in active and latent tuberculosis despite within-host variability in bacterial killing. *Nat. Med.* **20**, 75–79 (2014).

12. Havlir, D. V., Getahun, H., Sanne, I. & Nunn, P. Opportunities and challenges for HIV care in overlapping HIV and TB epidemics. *Journal of the American Medical Association* **300**, 423–430 (2008).

13. Cui, Z., Lin, M., Nie, S. & Lan, R. Risk factors associated with Tuberculosis (TB) among people living with HIV/AIDS: A pairmatched case-control study in Guangxi, China. *PLoS One* **12**,

(2017).

14. Burman, W. J. & Jones, B. E. Clinical and Radiographic Features of HIV-Related Tuberculosis. *Seminars in Respiratory Infections* **18**, 263–271 (2003).

15. Harries, A. D. *et al.* Deaths from tuberculosis in sub-Saharan African countries with a high prevalence of HIV-1. *Lancet* **357**, 1519–1523 (2001).

16. Gandhi, N. R. *et al.* HIV coinfection in multidrug- and extensively drug-resistant tuberculosis results in high early mortality. *Am. J. Respir. Crit. Care Med.* **181**, 80–86 (2010).

17. Ducati, R. G., Ruffino-Netto, A., Basso, L. A. & Santos, D. S. The resumption of consumption - A review on tuberculosis. *Memorias do Instituto Oswaldo Cruz* **101**, 697–714 (2006).

18. Bruchfeld, J., Correia-Neves, M. & Kallenius, G. Tuberculosis and HIV coinfection. *Cold Spring Harb. Perspect. Med.* **5**, (2015).

19. Pawlowski, A., Jansson, M., Sköld, M., Rottenberg, M. E. & Källenius, G. Tuberculosis and HIV co-infection. *PLoS Pathogens* **8**, (2012).

20. Aaron, L. *et al.* Tuberculosis in HIV-infected patients: A comprehensive review. *Clinical Microbiology and Infection* **10**, 388–398 (2004).

21. Bell, L. C. K. & Noursadeghi, M. Pathogenesis of HIV-1 and mycobacterium tuberculosis co-infection. *Nat. Rev. Microbiol.* **16**, 80–90 (2018).

22. Sonnenberg, P. *et al.* How soon after infection with HIV does the risk of tuberculosis start to increase? A retrospective cohort study in South African gold miners. *J. Infect. Dis.* **191**, 150–158 (2005).

23. World Health Organisation. The End TB Strategy. (2014).

24. World Health Organisation. *Global Tuberculosis Report 2017*. (2018).

25. European Centre for Disease Prevention and Control. *Handbook on tuberculosis laboratory diagnostic methods in the European Union*. (2018).

26. Kana, B. D. *et al.* The resuscitation-promoting factors of Mycobacterium tuberculosis are required for virulence and resuscitation from dormancy but are collectively dispensable for growth in vitro. *Mol. Microbiol.* **67**, 672–684 (2008).

27. Kik, S. V., Denkinger, C. M., Chedore, P. & Pai, M. Replacing smear microscopy for the diagnosis of tuberculosis: What is the market potential? *European Respiratory Journal* **43**, 1793–1796 (2014).

28. Srivastava, S. K., van Rijn, C. J. M. & Maarten, A. J. Biosensor-based detection of tuberculosis. *RSC Adv.* **6**, 17759–17771 (2016).

29. Atkinson, K. & Mabey, D. *Revolutionizing Tropical Medicine: Point-of-Care Tests, New Imaging Technologies and Digital Health*. (Wiley Blackwell, 2019). doi:10.1002/9781119282686

30. Steingart, K. R. *et al.* Xpert® MTB/RIF assay for pulmonary tuberculosis and rifampicin resistance in adults. *Cochrane Database of Systematic Reviews* **2014**, (2014).

31. Callaway, E. TB diagnostic test fails to curb cases: Poor response to roll-out of automated test highlights need for better health-care infrastructure in many countries. *Nature* **551**, 424–425 (2017).

32. Shah, M., Chihota, V., Coetzee, G., Churchyard, G. & Dorman, S. E. Comparison of laboratory costs of rapid molecular tests and conventional diagnostics for detection of tuberculosis and drug-resistant tuberculosis in South Africa. *BMC Infect. Dis.* **13**, 352 (2013).

33. Mori, Y. & Notomi, T. Loop-mediated isothermal amplification (LAMP): A rapid, accurate, and cost-effective diagnostic method for infectious diseases. *Journal of Infection and Chemotherapy* **15**, 62–69 (2009).

34. World Health Organisation. *The use of loop-mediated isothermal amplification (TB-LAMP) for the diagnosis of pulmonary tuberculosis. Policy guidance*. (2016).

35. Steingart, K. R. *et al.* Fluorescence versus conventional sputum smear microscopy for tuberculosis: a systematic review. *Lancet Infectious Diseases* **6**, 570–581 (2006).

36. Cruciani, M. *et al.* Meta-Analysis of BACTEC MGIT 960 and

BACTEC 460 TB, with or without Solid Media, for Detection of Mycobacteria. *J. Clin. Microbiol.* **42**, 2321–2325 (2004).

37. Ling, D. I., Zwerling, A. A. & Pai, M. GenoType MTBDR assays for the diagnosis of multidrug-resistant tuberculosis: A meta-analysis. *Eur. Respir. J.* **32**, 1165–1174 (2008).

38. World Health Organisation. *The use of molecular line probe assays for the detection of resistance to isoniazid and rifampicin*. (2016).

39. World Health Organisation. *Molecular line probe assays for rapid screening of patients at risk of multidrug-resistant tuberculosis (MDR-TB). Policy statement*. (2008).

40. Nathavitharana, R. R. *et al.* Accuracy of line probe assays for the diagnosis of pulmonary and multidrug-resistant tuberculosis: A systematic review and meta-analysis. *European Respiratory Journal* **49**, 1601075 (2017).

41. Barnard, M. *et al.* The diagnostic performance of the GenoType MTBDRplus version 2 line probe assay is equivalent to that of the Xpert MTB/RIF assay. *J. Clin. Microbiol.* **50**, 3712–3716 (2012).

42. Crudu, V. *et al.* First evaluation of an improved assay for molecular genetic detection of tuberculosis as well as rifampin and isoniazid resistances. *J. Clin. Microbiol.* **50**, 1264–1269 (2012).

43. World Health Organisation. High-priority target product profiles for new tuberculosis diagnostics: report of a consensus meeting. (2014).

44. Land, K. J., Boeras, D. I., Chen, X.-S., Ramsay, A. R. & Peeling, R. W. REASSURED diagnostics to inform disease control strategies, strengthen health systems and improve patient outcomes. *Nat. Microbiol.* **4**, 46–54 (2019).

45. Atkinson, A. J. *et al.* Biomarkers and surrogate endpoints: Preferred definitions and conceptual framework. *Clin. Pharmacol. Ther.* **69**, 89–95 (2001).

46. Strimbu, K. & Tavel, J. A. What are biomarkers? *Current Opinion in HIV and AIDS* **5**, 463–466 (2010).

47. Goletti, D., Petruccioli, E., Joosten, S. A. & Ottenhoff, T. H. M. Tuberculosis biomarkers: From diagnosis to protection. *Infect. Dis. Rep.* **8**, 24–32 (2016).

48. Penn, B. H. *et al.* An Mtb-Human Protein-Protein Interaction Map Identifies a Switch between Host Antiviral and Antibacterial Responses. *Mol. Cell* **71**, 637-648.e5 (2018).

49. Tucci, P., González-Sapienza, G. & Marin, M. Pathogen-derived biomarkers for active tuberculosis diagnosis. *Front. Microbiol.* **5**, 549 (2014).

50. MacLean, E. *et al.* A systematic review of biomarkers to detect active tuberculosis. *Nat. Microbiol.* **4**, 748–758 (2019).

51. Yerlikaya, S., Broger, T., Maclean, E., Pai, M. & Denkinger, C. M. A tuberculosis biomarker database: the key to novel TB diagnostics. **56**, 253–257 (2017).

52. Kruh-Garcia, N. A. *et al.* Detection of Mycobacterium tuberculosis peptides in the exosomes of patients with active and latent M. tuberculosis infection using MRM-MS. *PLoS One* **9**, (2014).

53. Kashyap, R. S. *et al.* Demonstration of components of antigen 85 complex in cerebrospinal fluid of tuberculous meningitis patients. *Clin. Diagn. Lab. Immunol.* **12**, 752–758 (2005).

54. Kashyap, R. S. *et al.* Diagnosis of tuberculosis in an Indian population by an indirect ELISA protocol based on detection of Antigen 85 complex: A prospective cohort study. *BMC Infect. Dis.* **7**, (2007).

55. Trzaskowski, M., Napiórkowska, A., Augustynowicz-Kopeć, E. & Ciach, T. Detection of tuberculosis in patients with the use of portable SPR device. *Sensors Actuators, B Chem.* **260**, 786–792 (2018).

56. Song, F., Sun, X., Wang, X., Nai, Y. & Liu, Z. Early diagnosis of tuberculous meningitis by an indirect ELISA protocol based on the detection of the antigen ESAT-6 in cerebrospinal fluid. *Ir. J. Med. Sci.* **183**, 85–88 (2014).

57. Broger, T. *et al.* Sensitive electrochemiluminescence (ECL) immunoassays for detecting lipoarabinomannan (LAM) and ESAT-6 in urine and serum from tuberculosis patients. *PLoS One* **14**, (2019).

58. Mukundan, H. *et al.* Rapid detection of Mycobacterium tuberculosis biomarkers in a sandwich immunoassay format using a

waveguide-based optical biosensor. *Tuberculosis* **92**, 407–416 (2012).

59. Peláez, E. C. *et al.* Detection and Quantification of HspX Antigen in Sputum Samples Using Plasmonic Biosensing: Toward a Real Point-of-Care (POC) for Tuberculosis Diagnosis. *ACS Infect. Dis.* **6**, 1110–1120 (2020).

60. Haldar, S. *et al.* Detection of Mycobacterium tuberculosis GlcB or HspX Antigens or devR DNA Impacts the Rapid Diagnosis of Tuberculous Meningitis in Children. *PLoS One* **7**, (2012).

61. Nicol, M. P. *et al.* Urine lipoarabinomannan testing for diagnosis of pulmonary tuberculosis in children: A prospective study. *Lancet Glob. Heal.* **2**, e278–e284 (2014).

62. Kawasaki, M. *et al.* Lipoarabinomannan in sputum to detect bacterial load and treatment response in patients with pulmonary tuberculosis: Analytic validation and evaluation in two cohorts. *PLOS Med.* **16**, (2019).

63. Turbawaty, D. K. *et al.* Comparison of the Performance of Urinary Mycobacterium tuberculosis Antigens Cocktail (ESAT6, CFP10, and MPT64) with Culture and Microscopy in Pulmonary Tuberculosis Patients. *Int. J. Microbiol.* **2017**, (2017).

64. Bekmurzayeva, A., Sypabekova, M. & Kanayeva, D. Tuberculosis diagnosis using immunodominant, secreted antigens of Mycobacterium tuberculosis. *Tuberculosis* **93**, 381–388 (2013).

65. Sakashita, K. *et al.* Ultrasensitive enzyme-linked immunosorbent assay for the detection of MPT64 secretory antigen to evaluate Mycobacterium tuberculosis viability in sputum. *Int. J. Infect. Dis.* **96**, 244–253 (2020).

66. Pollock, N. R. *et al.* Validation of mycobacterium tuberculosis Rv1681 protein as a diagnostic marker of active pulmonary tuberculosis. *J. Clin. Microbiol.* **51**, 1367–1373 (2013).

67. Wu, X. *et al.* Preparation of immunochromatographic strips for rapid detection of early secreted protein ESAT-6 and culture filtrate protein CFP-10 from Mycobacterium tuberculosis. *Medicine (Baltimore).* **96**, (2017).

68. Alhajj, M. & Farhana, A. *Enzyme Linked Immunosorbent Assay*

(ELISA). *StatPearls* (StatPearls Publishing, 2020).

69. Dheda, K. *et al.* Clinical Utility of a Commercial LAM-ELISA Assay for TB Diagnosis in HIV-Infected Patients Using Urine and Sputum Samples. *PLoS One* **5**, (2010).

70. Dai, Z. *et al.* A multiple-antigen detection assay for tuberculosis diagnosis based on broadly reactive polyclonal antibodies. *Iran. J. Basic Med. Sci.* **20**, 360–367 (2017).

71. Koczula, K. M. & Gallotta, A. Lateral flow assays. *Essays Biochem.* **60**, 111–120 (2016).

72. Correia-Neves, M. *et al.* Biomarkers for tuberculosis: the case for lipoarabinomannan. *ERJ Open Res.* **5**, 00115–02018 (2019).

73. World Health Organisation. The use of lateral flow urine lipoarabinomannan assay (LF-LAM) for the diagnosis and screening of active tuberculosis in people living with HIV: policy. (2015).

74. Drain, P. K. *et al.* Evaluating diagnostic point-of-care tests in resource-limited settings. *The Lancet Infectious Diseases* **14**, 239–249 (2014).

75. Monošík, R. & Angnes, L. Utilisation of micro- and nanoscaled materials in microfluidic analytical devices. *Microchem. J.* **119**, 159–168 (2015).

76. Aryasomayajula, A., Bayat, P., Rezai, P. & Selvaganapathy, P. R. Microfluidic Devices and Their Applications. in *Springer Handbook of Nanotechnology* 487–536 (Springer, Berlin, Heidelberg, 2017).

77. Chin, C. D., Linder, V. & Sia, S. K. Commercialization of microfluidic point-of-care diagnostic devices. *Lab Chip* **12**, 2118 (2012).

78. Sia, S. K. & Whitesides, G. M. Microfluidic devices fabricated in Poly(dimethylsiloxane) for biological studies. *Electrophoresis* **24**, 3563–3576 (2003).

79. Whitesides, G. M. The origins and the future of microfluidics. *Nature* **442**, 368–373 (2006).

80. Becker, H. & Gärtner, C. Polymeric Microfluidic Devices for High

Performance Optical Imaging and Detection Methods in Bioanalytics. in *Optical Nano- and Microsystems for Bioanalytics* 271–288 (2012). doi:10.1007/978-3-642-25498-7_10

81. Nagel, B., Dellweg, H. & Gierasch, L. M. Glossary for chemists of terms used in biotechnology. *Pure Appl. Chem.* **64**, 143–168 (1992).

82. Bhalla, N., Jolly, P., Formisano, N. & Estrela, P. Introduction to biosensors. *Essays Biochem.* **60**, 1–8 (2016).

83. Wang, J. Electrochemical glucose biosensors. *Chemical Reviews* **108**, 814–825 (2008).

84. Narayanaswamy, R. & Wolfbeis, O. S. *Optical sensors*. (Springer Berlin Heidelberg, 2004).

85. Damborský, P., Švitel, J. & Katrlík, J. Optical biosensors. *Essays Biochem.* **60**, 91–100 (2016).

86. González-Guerrero, A. B., Maldonado, J., Herranz, S. & Lechuga, L. M. Trends in photonic lab-on-chip interferometric biosensors for point-of-care diagnostics. *Anal. Methods* **8**, 8380–8394 (2016).

87. Passaro, V., Dell'Olio, F., Casamassima, B. & De Leonardis, F. Guided-Wave Optical Biosensors. *Sensors* **7**, 508–536 (2007).

88. Estevez, M. C., Alvarez, M. & Lechuga, L. M. Integrated optical devices for lab-on-a-chip biosensing applications. *Laser Photon. Rev.* **6**, 463–487 (2012).

89. Kozma, P., Kehl, F., Ehrentreich-Förster, E., Stamm, C. & Bier, F. F. Integrated planar optical waveguide interferometer biosensors: A comparative review. *Biosens. Bioelectron.* **58**, 287–307 (2014).

90. Puiu, M. & Bala, C. SPR and SPR imaging: Recent trends in developing nanodevices for detection and real-time monitoringof biomolecular events. *Sensors (Switzerland)* **16**, (2016).

91. Cottier, K., Wiki, M., Voirin, G., Gao, H. & Kunz, R. E. Label-free highly sensitive detection of (small) molecules by wavelength interrogation of integrated optical chips. *Sensors Actuators, B Chem.* **91**, 241–251 (2003).

92. Iqbal, M. *et al.* Label-free biosensor arrays based on silicon ring resonators and high-speed optical scanning instrumentation. *IEEE*

J. Sel. Top. Quantum Electron. **16**, 654–661 (2010).

93. Luchansky, M. S. *et al.* Characterization of the evanescent field profile and bound mass sensitivity of a label-free silicon photonic microring resonator biosensing platform. *Biosens. Bioelectron.* **26**, 1283–1291 (2010).

94. Gavela, A. F., García, D. G., Ramirez, J. C. & Lechuga, L. M. Last advances in silicon-based optical biosensors. *Sensors* **16**, 285 (2016).

95. Homola, J. Surface plasmon resonance sensors for detection of chemical and biological species. *Chem. Rev.* **108**, 462–93 (2008).

96. Nguyen, H. H., Park, J., Kang, S. & Kim, M. Surface plasmon resonance: A versatile technique for biosensor applications. *Sensors* **15**, 10481–10510 (2015).

97. Hill, R. T. Plasmonic biosensors. *Wiley Interdisciplinary Reviews: Nanomedicine and Nanobiotechnology* **7**, 152–168 (2015).

98. *Surface Plasmon Resonance Based Sensors*. **4**, (Springer Berlin Heidelberg, 2006).

99. Lopez, G. A., Estevez, M. C., Soler, M. & Lechuga, L. M. Recent advances in nanoplasmonic biosensors: Applications and lab-on-a-chip integration. *Nanophotonics* **6**, 123–136 (2017).

100. Prabowo, B. A., Purwidyantri, A. & Liu, K. C. Surface plasmon resonance optical sensor: A review on light source technology. *Biosensors* **8**, (2018).

101. Gao, Y., Gan, Q. & Bartoli, F. J. Breakthroughs in Photonics 2013: Research Highlights on Biosensors Based on Plasmonic Nanostructures. *IEEE Photonics Journal* **6**, (2014).

102. Luan, E., Shoman, H., Ratner, D. M., Cheung, K. C. & Chrostowski, L. Silicon photonic biosensors using label-free detection. *Sensors* **18**, (2018).

103. Misiakos, K. *et al.* Broad-band Mach-Zehnder interferometers as high performance refractive index sensors: Theory and monolithic implementation. *Opt. Express* **22**, 8856 (2014).

104. Psarouli, A. *et al.* Monolithically integrated broad-band Mach-Zehnder interferometers for highly sensitive label-free detection of

biomolecules through dual polarization optics. *Sci. Rep.* **5**, 17600 (2015).

105. Fernández-Gavela, A. *et al.* Full integration of photonic nanoimmunosensors in portable platforms for on-line monitoring of ocean pollutants. *Sensors Actuators, B Chem.* **297**, 126758 (2019).

106. Duval, D., Osmond, J., Dante, S., Domínguez, C. & Lechuga, L. M. Grating couplers integrated on Mach-Zehnder interferometric biosensors operating in the visible range. *IEEE Photonics J.* **5**, (2013).

107. Prieto, F. *et al.* Integrated Mach-Zehnder interferometer based on ARROW structures for biosensor applications. *Sensors Actuators, B Chem.* **92**, 151–158 (2003).

108. Zinoviev, K. E., González-Guerrero, A. B., Domínguez, C. & Lechuga, L. M. Integrated bimodal waveguide interferometric biosensor for label-free analysis. *J. Light. Technol.* **29**, 1926–1930 (2011).

109. González-Guerrero, A. B., Maldonado, J., Dante, S., Grajales, D. & Lechuga, L. M. Direct and label-free detection of the human growth hormone in urine by an ultrasensitive bimodal waveguide biosensor. *J. Biophotonics* **10**, 61–67 (2017).

110. Martens, D. *et al.* Compact silicon nitride arrayed waveguide gratings for very near-infrared wavelengths. *IEEE Photonics Technol. Lett.* **27**, 137–140 (2015).

111. Smit, M. K., Member, A. & Dam, C. Van. PHASAR-Based WDM-Devices : **2**, 236–250 (1996).

112. Martens, D. & Bienstman, P. Comparison between Vernier-cascade and MZI as transducer for biosensing with on-chip spectral filter. *Nanophotonics* **6**, 703–712 (2017).

113. Jena, R. K. & Yue, C. Y. Cyclic olefin copolymer based microfluidic devices for biochip applications: Ultraviolet surface grafting using 2-methacryloyloxyethyl phosphorylcholine. *Biomicrofluidics* **6**, 12822–1282212 (2012).

114. Rodrigues, R. O., Lima, R., Gomes, H. T. & Silva, A. M. T. Polymer microfluidic devices: an overview of fabrication methods. *U.Porto J. Eng.* **1**, 67–79 (2017).

115. Tsao, C. W. Polymer microfluidics: Simple, low-cost fabrication process bridging academic lab research to commercialized production. *Micromachines* **7**, (2016).

116. Tsao, C. W. & DeVoe, D. L. Bonding of thermoplastic polymer microfluidics. *Microfluidics and Nanofluidics* **6**, 1–16 (2009).

117. Zinoviev, K. *et al.* Silicon photonic biosensors for lab-on-a-chip applications. *Adv. Opt. Technol.* (2008). doi:10.1155/2008/383927

118. Welch, N. G., Scoble, J. A., Muir, B. W. & Pigram, P. J. Orientation and characterization of immobilized antibodies for improved immunoassays (Review). *Biointerphases* **12**, 02D301 (2017).

119. Kim, D. & Herr, A. E. Protein immobilization techniques for microfluidic assays. *Biomicrofluidics* **7**, 1–47 (2013).

120. Trilling, A. K., Beekwilder, J. & Zuilhof, H. Antibody orientation on biosensor surfaces: A minireview. *Analyst* **138**, 1619–1627 (2013).

121. Rusmini, F., Zhong, Z. & Feijen, J. Protein immobilization strategies for protein biochips. *Biomacromolecules* **8**, 1775–1789 (2007).

122. Sassolas, A., Blum, L. J. & Leca-Bouvier, B. D. Immobilization strategies to develop enzymatic biosensors. *Biotechnol. Adv.* **30**, 489–511 (2012).

123. Jung, Y., Jeong, J. Y. & Chung, B. H. Recent advances in immobilization methods of antibodies on solid supports. *Analyst* **133**, 697–701 (2008).

124. Samanta, D. & Sarkar, A. Immobilization of bio-macromolecules on self-assembled monolayers: Methods and sensor applications. *Chem. Soc. Rev.* **40**, 2567–2592 (2011).

125. Diao, J., Ren, D., Engstrom, J. R. & Lee, K. H. A surface modification strategy on silicon nitride for developing biosensors. *Anal. Biochem.* **343**, 322–328 (2005).

126. Yadav, A. R., Sriram, R., Carter, J. A. & Miller, B. L. Comparative study of solution-phase and vapor-phase deposition of aminosilanes on silicon dioxide surfaces. *Mater. Sci. Eng. C* **35**, 283–290 (2014).

127. Miranda, A., Martínez, L. & De Beule, P. A. A. Facile synthesis of an aminopropylsilane layer on Si/SiO2 substrates using ethanol as APTES solvent. *MethodsX* **7**, 100931 (2020).

128. Wang, Y. & Lieberman, M. Growth of ultrasmooth octadecyltrichlorosilane self-assembled monolayers on SiO2. *Langmuir* **19**, 1159–1167 (2003).

129. Fadeev, A. Y. & McCarthy, T. J. Self-assembly is not the only reaction possible between alkyltrichlorosilanes and surfaces: monomolecular and oligomeric covalently attached layers of dichloro- and trichloroalkylsilanes on silicon. *Langmuir* **16**, 7268–7274 (2000).

130. Vashist, S. K., Lam, E., Hrapovic, S., Male, K. B. & Luong, J. H. T. Immobilization of antibodies and enzymes on 3-aminopropyltriethoxysilane-functionalized bioanalytical platforms for biosensors and diagnostics. *Chemical Reviews* **114**, 11083–11130 (2014).

131. Vos, R. *et al.* Vapor-phase deposition of n3-containing monolayers on sio2 and si3 n4 for wafer scale biofunctionalization. in *Solid State Phenomena* **282 SSP**, 31–36 (Trans Tech Publications Ltd, 2018).

132. Chocarro-Ruiz, B. *et al.* Interferometric nanoimmunosensor for label-free and real-time monitoring of Irgarol 1051 in seawater. *Biosens. Bioelectron.* **117**, 47–52 (2018).

133. González-Guerrero, A. B., Alvarez, M., Castaño, A. G., Domínguez, C. & Lechuga, L. M. A comparative study of in-flow and micro-patterning biofunctionalization protocols for nanophotonic silicon-based biosensors. *J. Colloid Interface Sci.* **393**, 402–410 (2013).

134. Seplveda, B. *et al.* Optical biosensor microsystems based on the integration of highly sensitive Mach-Zehnder interferometer devices. *J. Opt. A Pure Appl. Opt.* **8**, S561 (2006).

135. Vos, R. *et al.* Chemical Vapor Deposition of Azidoalkylsilane Monolayer Films. *Langmuir* **34**, 1400–1409 (2018).

136. Kolb, H. C., Finn, M. G. & Sharpless, K. B. Click Chemistry: Diverse Chemical Function from a Few Good Reactions. *Angewandte Chemie - International Edition* **40**, 2004–2021 (2001).

137. Takayama, Y., Kusamori, K. & Nishikawa, M. Click chemistry as a tool for cell engineering and drug delivery. *Molecules* **24**, (2019).

138. Zeng, D., Zeglis, B. M., Lewis, J. S. & Anderson, C. J. The growing impact of bioorthogonal click chemistry on the development of radiopharmaceuticals. *Journal of Nuclear Medicine* **54**, 829–832 (2013).

139. Best, M. D. Click chemistry and bioorthogonal reactions: Unprecedented selectivity in the labeling of biological molecules. *Biochemistry* **48**, 6571–6584 (2009).

140. Grammel, M. & Hang, H. C. Chemical reporters for biological discovery. *Nature Chemical Biology* **9**, 475–484 (2013).

141. Evans, R. A. The Rise of Azide-Alkyne 1,3-Dipolar 'Click' Cycloaddition and its Application to Polymer Science and Surface Modification. *Aust. J. Chem* **60**, 384–395 (2007).

142. Pickens, C. J., Johnson, S. N., Pressnall, M. M., Leon, M. A. & Berkland, C. J. Practical Considerations, Challenges, and Limitations of Bioconjugation via Azide-Alkyne Cycloaddition. *Bioconjugate Chemistry* **29**, 686–701 (2018).

143. Sen, R., Escorihuela, J., Smulders, M. M. J. & Zuilhof, H. Use of Ambient Ionization High-Resolution Mass Spectrometry for the Kinetic Analysis of Organic Surface Reactions. *Langmuir* **32**, 3412–3419 (2016).

144. Agard, N. J., Prescher, J. A. & Bertozzi, C. R. A strain-promoted [3 + 2] azide-alkyne cycloaddition for covalent modification of biomolecules in living systems. *J. Am. Chem. Soc.* **126**, 15046–15047 (2004).

145. Marks, I. S. *et al.* Strain-promoted 'click' chemistry for terminal labeling of DNA. *Bioconjug. Chem.* **22**, 1259–1263 (2011).

146. Kim, E. & Koo, H. Biomedical applications of copper-free click chemistry:: In vitro, in vivo, and ex vivo. *Chem. Sci.* **10**, 7835–7851 (2019).

147. Dommerholt, J., Rutjes, F. P. J. T. & van Delft, F. L. Strain-Promoted 1,3-Dipolar Cycloaddition of Cycloalkynes and Organic Azides. *Topics in Current Chemistry* **374**, 1–20 (2016).

148. Mauriz, E., Dey, P. & Lechuga, L. M. Advances in nanoplasmonic

biosensors for clinical applications. *Analyst* **144**, 7105–7129 (2019).

149. Soler, M., Huertas, C. S. & Lechuga, L. M. Label-free plasmonic biosensors for point-of-care diagnostics: a review. *Expert Review of Molecular Diagnostics* **19**, 71–81 (2019).

150. Bürgi, T. Properties of the gold-sulphur interface: from self-assembled monolayers to clusters. *Nanoscale* **7**, 15553–15567 (2015).

151. Love, J. C., Estroff, L. A., Kriebel, J. K., Nuzzo, R. G. & Whitesides, G. M. Self-assembled monolayers of thiolates on metals as a form of nanotechnology. *Chemical Reviews* **105**, 1103–1169 (2005).

152. Soler, M. *et al.* Direct detection of protein biomarkers in human fluids using site-specific antibody immobilization strategies. *Sensors (Basel).* **14**, 2239–58 (2014).

153. Eeftens, J. M., van der Torre, J., Burnham, D. R. & Dekker, C. Copper-free click chemistry for attachment of biomolecules in magnetic tweezers. *BMC Biophys.* **8**, 9 (2015).

154. Gori, A. *et al.* Screening Complex Biological Samples with Peptide Microarrays: The Favorable Impact of Probe Orientation via Chemoselective Immobilization Strategies on Clickable Polymeric Coatings. *Bioconjug. Chem.* **27**, 2669–2677 (2016).

155. Ryken, J. *et al.* Biosensing with SiO2-covered SPR substrates in a commercial SPR-tool. *Sensors Actuators, B Chem.* **200**, 167–172 (2014).

156. Bañuls, M. J., Puchades, R. & Maquieira, Á. Chemical surface modifications for the development of silicon-based label-free integrated optical (IO) biosensors: A review. *Analytica Chimica Acta* **777**, 1–16 (2013).

157. Fernandez, R. E., Bhattacharya, E. & Chadha, A. Covalent immobilization of Pseudomonas cepacia lipase on semiconducting materials. *Appl. Surf. Sci.* **254**, 4512–4519 (2008).

158. Cardenosa-Rubio, M. C., Graybill, R. M. & Bailey, R. C. Combining asymmetric PCR-based enzymatic amplification with silicon photonic microring resonators for the detection of lncRNAs from low input human RNA samples. *Analyst* **143**, 1210–1216

(2018).

159. Manning, M., Harvey, S., Galvin, P. & Redmond, G. A versatile multi-platform biochip surface attachment chemistry. *Mater. Sci. Eng. C* **23**, 347–351 (2003).

160. Gandhiraman, R. P. *et al.* Deposition of chemically reactive and repellent sites on biosensor chips for reduced non-specific binding. *Colloids Surfaces B Biointerfaces* **79**, 270–275 (2010).

161. Huertas, C. S., Domínguez-Zotes, S. & Lechuga, L. M. Analysis of alternative splicing events for cancer diagnosis using a multiplexing nanophotonic biosensor. *Sci. Rep.* **7**, 1–8 (2017).

162. Janissen, R., Oberbarnscheidt, L. & Oesterhelt, F. Optimized straight forward procedure for covalent surface immobilization of different biomolecules for single molecule applications. *Colloids Surfaces B Biointerfaces* **71**, 200–207 (2009).

163. Wallis, R. S. *et al.* Biomarkers for tuberculosis disease activity, cure, and relapse. *The Lancet Infectious Diseases* **9**, 162–172 (2009).

164. Peter, J. *et al.* Urine for the diagnosis of tuberculosis: current approaches, clinical applicability, and new developments. *Curr. Opin. Pulm. Med.* **16**, 262–270 (2010).

165. Agha, M. A., El-Helbawy, R. H., El-Helbawy, N. G. & El-Sheak, N. M. Utility of quantitative analysis of urine lipoarabinomannan in the diagnosis of tuberculosis. *Egypt. J. Chest Dis. Tuberc.* **62**, 401–407 (2013).

166. Lawn, S. D. Point-of-care detection of lipoarabinomannan (LAM) in urine for diagnosis of HIV-associated tuberculosis: A state of the art review. *BMC Infect. Dis.* **12**, 1 (2012).

167. Kaur, D. *et al.* Lipoarabinomannan of Mycobacterium: mannose capping by a multifunctional terminal mannosyltransferase. *Proc. Natl. Acad. Sci. U. S. A.* **105**, 17973–7 (2008).

168. Mukundan, H. *et al.* Understanding the interaction of Lipoarabinomannan with membrane mimetic architectures. *Tuberculosis* **92**, 38–47 (2012).

169. Mishra, A. K., Driessen, N. N., Appelmelk, B. J. & Besra, G. S. Lipoarabinomannan and related glycoconjugates: Structure,

biogenesis and role in Mycobacterium tuberculosis physiology and host-pathogen interaction. *FEMS Microbiol. Rev.* **35**, 1126–1157 (2011).

170. Fukuda, T. *et al.* Critical roles for lipomannan and lipoarabinomannan in cell wall integrity of mycobacteria and pathogenesis of tuberculosis. *MBio* **4**, 8–10 (2013).

171. Hamasur, B. *et al.* Rapid diagnosis of tuberculosis by detection of mycobacterial lipoarabinomannan in urine. *J. Microbiol. Methods* **45**, 41–52 (2001).

172. Choudhary, A. *et al.* Characterization of the Antigenic Heterogeneity of Lipoarabinomannan, the Major Surface Glycolipid of Mycobacterium tuberculosis , and Complexity of Antibody Specificities toward This Antigen . *J. Immunol.* **200**, 3053–3066 (2018).

173. Lawn, S. D., Kerkhoff, A. D., Vogt, M. & Wood, R. Diagnostic accuracy of a low-cost, urine antigen, point-of-care screening assay for HIV-associated pulmonary tuberculosis before antiretroviral therapy: A descriptive study. *Lancet Infect. Dis.* **12**, 201–209 (2012).

174. World Health Organization (WHO). Lateral flow urine lipoarabinomannan assay (LF-LAM) for the diagnosis of active tuberculosis in people living with HIV. *WHO* (2019).

175. Bulterys, M. A. *et al.* Point-Of-Care Urine LAM Tests for Tuberculosis Diagnosis : A Status Update. 1–14

176. Broger, T. *et al.* Novel lipoarabinomannan point-of-care tuberculosis test for people with HIV: a diagnostic accuracy study. *Lancet Infect. Dis.* **19**, 852–861 (2019).

177. Kalayjian, R. C. The Treatment of HIV-Associated Nephropathy. *Advances in Chronic Kidney Disease* **17**, 59–71 (2010).

178. Lawn, S. D. & Gupta-Wright, A. Detection of lipoarabinomannan (LAM) in urine is indicative of disseminated TB with renal involvement in patients living with hiv and advanced immunodeficiency: Evidence and implications. *Transactions of the Royal Society of Tropical Medicine and Hygiene* **110**, 180–185 (2015).

179. Cox, J. A. *et al.* Is urinary lipoarabinomannan the result of renal tuberculosis? Assessment of the renal histology in an autopsy cohort of ugandan HIV-infected adults. *PLoS One* **10**, 123323 (2015).

180. De, P. *et al.* Estimation of D-arabinose by gas chromatography/mass spectrometry as surrogate for mycobacterial lipoarabinomannan in human urine. *PLoS One* **10**, (2015).

181. Xu, H., Lu, J. R. & Williams, D. E. Effect of surface packing density of interfacially adsorbed monoclonal antibody on the binding of hormonal antigen human chorionic gonadotrophin. *J. Phys. Chem. B* **110**, 1907–1914 (2006).

182. FDA. *Bioanalytical Method Validation - Guidance for Industry*. (2018).

183. Karak, T. & Bhattacharyya, P. Human urine as a source of alternative natural fertilizer in agriculture: A flight of fancy or an achievable reality. *Resources, Conservation and Recycling* **55**, 400–408 (2011).

184. Wang, Z. H., Viana, A. S., Jin, G. & Abrantes, L. M. Immunosensor interface based on physical and chemical immunoglobulin G adsorption onto mixed self-assembled monolayers. *Bioelectrochemistry* **69**, 180–186 (2006).

185. Tengvall, P., Lundström, I. & Liedberg, B. Protein adsorption studies on model organic surfaces: An ellipsometric and infrared spectroscopic approach. *Biomaterials* **19**, 407–422 (1998).

186. Peláez, E. C. *et al.* Nanoplasmonic biosensor device for the monitoring of acenocoumarol therapeutic drug in plasma. *Biosens. Bioelectron.* **119**, 149–155 (2018).

187. Gutiérrez-Mejía, F. A., van Ijzendoorn, L. J. & Prins, M. W. J. Surfactants modify the torsion properties of proteins: A single molecule study. *N. Biotechnol.* **32**, 441–449 (2015).

188. Krishnan, S., Weinman, C. J. & Ober, C. K. Advances in polymers for anti-biofouling surfaces. *J. Mater. Chem.* **18**, 3405–3413 (2008).

189. Soler, M., Estevez, M.-C., Villar-Vazquez, R., Casal, J. I. & Lechuga, L. M. Label-free nanoplasmonic sensing of tumor-associate autoantibodies for early diagnosis of colorectal cancer.

Anal. Chim. Acta **930**, 31–38 (2016).

190. Shah, M. *et al.* Diagnostic Accuracy of a Urine Lipoarabinomannan Test for Tuberculosis in Hospitalized Patients in a High HIV Prevalence Setting. *JAIDS J. Acquir. Immune Defic. Syndr.* **52**, 145–151 (2009).

191. Shah, M. *et al.* Quantitative analysis of a urine-based assay for detection of lipoarabinomannan in patients with tuberculosis. *J. Clin. Microbiol.* **48**, 2972–4 (2010).

192. Woldeyohannes, D., Sisay, S., Mengistu, B. & Kassa, H. Directly observed treatment short-course (DOTS) for treatment of new tuberculosis cases in Somali Regional State, Eastern Ethiopia: Ten years retrospective study. *BMC Res. Notes* **8**, 1–7 (2015).

193. Andersen, P., Munk, M. E., Pollock, J. M. & Doherty, T. M. Specific immune-based diagnosis of tuberculosis. *Lancet* **356**, 1099–1104 (2000).

194. Arend, S. M. *et al.* Detection of active tuberculosis infection by T cell responses to early- secreted antigenic target 6-kDa protein and culture filtrate protein 10. *J. Infect. Dis.* **181**, 1850–1854 (2000).

195. Lalvani, A. & Millington, K. A. T-cell interferon-γ release assays: Can we do better? *European Respiratory Journal* **32**, 1428–1430 (2008).

196. Shen, G. H., Chiou, C. S., Hu, S. T., Wu, K. M. & Chen, J. H. Rapid identification of the Mycobacterium tuberculosis complex by combining the ESAT-6/CFP-10 immunochromatographic assay and smear morphology. *J. Clin. Microbiol.* **49**, 902–907 (2011).

197. Mener, A. K., Bal, N. C., Chary, K. V. R. & Arora, A. Mycobacterium tuberculosis H37Rv ESAT-6-CFP-10 complex formation confers thermodynamic and biochemical stability. *FEBS J.* **273**, 1445–1462 (2006).

198. Uvarova, E. A. *et al.* Oral immunogenicity of plant-made mycobacterium tuberculosis ESAT6 and CFP10. *Biomed Res. Int.* **2013**, (2013).

199. Guo, S. *et al.* The CFP10/ESAT6 complex of Mycobacterium tuberculosis may function as a regulator of macrophage cell death at different stages of tuberculosis infection. *Med. Hypotheses* **78**, 389–

392 (2012).

200. Singh, B., Singh, G., Trajkovic, V. & Sharma, P. Intracellular expression of Mycobacterium tuberculosis-specific 10-kDa antigen down-regulates macrophage B7·1 expression and nitric oxide release. *Clin. Exp. Immunol.* **134**, 70–77 (2003).

201. Dwivedi, V. P. *et al.* Mycobacterium tuberculosis directs T helper 2 cell differentiation by inducing interleukin-1β production in dendritic cells. *J. Biol. Chem.* **287**, 33656–33663 (2012).

202. Nagai, S., Gotten Wiker, H., Harboe, M. & Kinomoto, M. Isolation and partial characterization of major protein antigens in the culture fluid of Mycobacterium tuberculosis. *Infect. Immun.* **59**, 372–382 (1991).

203. Fu, R. *et al.* An improved whole-blood gamma interferon assay based on the CFP21-MPT64 fusion protein. *Clin. Vaccine Immunol.* **16**, 686–691 (2009).

204. Mustafa, T., Wiker, H. G., Mørkve, O. & Sviland, L. Reduced apoptosis and increased inflammatory cytokines in granulomas caused by tuberculous compared to non-tuberculous mycobacteria: Role of MPT64 antigen in apoptosis and immune response. *Clin. Exp. Immunol.* **150**, 105–113 (2007).

205. Mustafa, T., Wiker, H. G., Mørkve, O. & Sviland, L. Differential expression of mycobacterial antigen MPT64, apoptosis and inflammatory markers in multinucleated giant cells and epithelioid cells in granulomas caused by Mycobacterium tuberculosis. *Virchows Arch.* **452**, 449–456 (2008).

206. Forrellad, M. A. *et al.* Virulence factors of the mycobacterium tuberculosis complex. *Virulence* **4**, 3–66 (2013).

207. Arora, J. *et al.* Utility of MPT64 antigen detection for rapid confirmation of mycobacterium tuberculosis complex. *J. Glob. Infect. Dis.* **7**, 66–69 (2015).

208. Abrahams, K. A. & Besra, G. S. Mycobacterial cell wall biosynthesis: A multifaceted antibiotic target. *Parasitology* **145**, 116–133 (2018).

209. Backus, K. M. *et al.* The three Mycobacterium tuberculosis antigen 85 isoforms have unique substrates and activities determined by

non-active site regions. *J. Biol. Chem.* **289**, 25041–25053 (2014).

210. Belisle, J. T. *et al.* Role of the major antigen of Mycobacterium tuberculosis in cell wall biogenesis. *Science (80-.).* **276**, 1420–1422 (1997).

211. Tuuminen, T. Urine as a specimen to diagnose infections in twenty-first century: Focus on analytical accuracy. *Frontiers in Immunology* **3**, (2012).

212. Bentley-Hibbert, S. I., Quan, X., Newman, T., Huygen, K. & Godfrey, H. P. Pathophysiology of antigen 85 in patients with active tuberculosis: Antigen 85 circulates as complexes with fibronectin and immunoglobulin G. *Infect. Immun.* **67**, 581–588 (1999).

213. Shin, A. R. *et al.* Improved sensitivity of diagnosis of tuberculosis in patients in Korea via a cocktail enzyme-linked immunosorbent assay containing the abundantly expressed antigens of the K strain of Mycobacterium tuberculosis. *Clin. Vaccine Immunol.* **15**, 1788–1795 (2008).

214. Jørstad, M. D., Marijani, M., Dyrhol-Riise, A. M., Sviland, L. & Mustafa, T. MPT64 antigen detection test improves routine diagnosis of extrapulmonary tuberculosis in a low-resource setting: A study from the tertiary care hospital in Zanzibar. *PLoS One* **13**, (2018).

215. Landowski, C. P. *et al.* Combinatorial use of antibodies to secreted mycobacterial proteins in a host immune system-independent test for tuberculosis. *J. Clin. Microbiol.* **39**, 2418–2424 (2001).

216. Phunpae, P. *et al.* Rapid diagnosis of tuberculosis by identification of Antigen 85 in mycobacterial culture system. *Diagn. Microbiol. Infect. Dis.* **78**, 242–248 (2014).

217. Liu, Z. *et al.* Clinical value of ELISA-MPT64 for the diagnosis of tuberculous pleurisy. *Curr. Microbiol.* **65**, 313–318 (2012).

218. Kim, J. *et al.* Rapid monitoring of CFP-10 during culture of Mycobacterium tuberculosis by using a magnetophoretic immunoassay. *Sensors Actuators, B Chem.* **177**, 327–333 (2013).

219. Chen, Y. *et al.* A sandwich-type electrochemical aptasensor for Mycobacterium tuberculosis MPT64 antigen detection using

C60NPs decorated N-CNTs/GO nanocomposite coupled with conductive PEI-functionalized metal-organic framework. *Biomaterials* **216**, 119253 (2019).

220. Kim, E. J. *et al.* An easy and sensitive sandwich assay for detection of Mycobacterium tuberculosis Ag85B antigen using quantum dots and gold nanorods. *Biosens. Bioelectron.* **87**, 150–156 (2017).

221. Romeo, A., Leung, T. S. & Sánchez, S. Smart biosensors for multiplexed and fully integrated point-of-care diagnostics. *Lab Chip* **16**, 1957–1961 (2016).

222. Dincer, C., Bruch, R., Kling, A., Dittrich, P. S. & Urban, G. A. Multiplexed Point-of-Care Testing – xPOCT. *Trends in Biotechnology* **35**, 728–742 (2017).

223. Spindel, S. & Sapsford, K. E. Evaluation of optical detection platforms for multiplexed detection of proteins and the need for point-of-care biosensors for clinical use. *Sensors (Switzerland)* **14**, 22313–22341 (2014).

224. Romanov, V. *et al.* A critical comparison of protein microarray fabrication technologies. *Analyst* **139**, 1303–1326 (2014).

225. Liu, G., Petrosko, S. H., Zheng, Z. & Mirkin, C. A. Evolution of Dip-Pen Nanolithography (DPN): From Molecular Patterning to Materials Discovery. *Chemical Reviews* **120**, 6009–6047 (2020).

226. Brown, K. A., Eichelsdoerfer, D. J., Liao, X., He, S. & Mirkin, C. A. Material transport in dip-pen nanolithography. *Frontiers of Physics* **9**, 385–397 (2014).

227. Rozhok, S., Piner, R. & Mirkin, C. A. Dip-pen nanolithography: What controls ink transport? *J. Phys. Chem. B* **107**, 751–757 (2003).

228. Tsarfati-BarAd, I., Sauer, U., Preininger, C. & Gheber, L. A. Miniaturized protein arrays: Model and experiment. *Biosens. Bioelectron.* **26**, 3774–3781 (2011).

229. Fabri-Faja, N. *et al.* Early sepsis diagnosis via protein and miRNA biomarkers using a novel point-of-care photonic biosensor. *Anal. Chim. Acta* **1077**, 232–242 (2019).

230. Dey, P. *et al.* Label-free Bacteria Quantification in Blood Plasma by a Bioprinted Microarray Based Interferometric Point-of-Care

Device. *ACS Sensors* **4**, 52–60 (2019).

231. Sekula-Neuner, S. *et al.* Allergen Arrays for Antibody Screening and Immune Cell Activation Profiling Generated by Parallel Lipid Dip-Pen Nanolithography. *Small* **8**, 585–591 (2012).

232. Basnar, B. & Willner, I. Dip-Pen-Nanolithographic Patterning of Metallic, Semiconductor, and Metal Oxide Nanostructures on Surfaces. *Small* **5**, 28–44 (2009).

233. Zhu, N. *et al.* A novel coronavirus from patients with pneumonia in China, 2019. *N. Engl. J. Med.* **382**, 727–733 (2020).

234. WHO. *Coronavirus disease (COVID-19) Global epidemiological situation 11 October*. (2020).

235. Astuti, I. & Ysrafil. Severe Acute Respiratory Syndrome Coronavirus 2 (SARS-CoV-2): An overview of viral structure and host response. *Diabetes Metab. Syndr. Clin. Res. Rev.* **14**, 407–412 (2020).

236. Jiang, S., Hillyer, C. & Du, L. Neutralizing Antibodies against SARS-CoV-2 and Other Human Coronaviruses. *Trends in Immunology* **41**, 355–359 (2020).

237. Yan, R. *et al.* Structural basis for the recognition of SARS-CoV-2 by full-length human ACE2. *Science (80-.).* **367**, 1444–1448 (2020).

238. World Health Organization. *Coronavirus disease 2019 (COVID-19): situation report, 73*. (2020).

239. Soler, M., Estevez, M. C., Cardenosa-Rubio, M., Astua, A. & Lechuga, L. M. How Nanophotonic Label-Free Biosensors Can Contribute to Rapid and Massive Diagnostics of Respiratory Virus Infections: COVID-19 Case. *ACS Sensors* **5**, 2663–2678 (2020).

240. Alcoba-Florez, J. *et al.* Sensitivity of different RT-qPCR solutions for SARS-CoV-2 detection. *Int. J. Infect. Dis.* **99**, 190–192 (2020).

241. Tang, Y. W., Schmitz, J. E., Persing, D. H. & Stratton, C. W. Laboratory diagnosis of COVID-19: Current issues and challenges. *Journal of Clinical Microbiology* **58**, (2020).

242. Krammer, F. & Simon, V. Serology assays to manage COVID-19. *Science (80-.).* **368**, 1060–1061 (2020).

243. Panbio COVID-19 Ag Rapid Test Device | Abbott Point of Care Testing. Available at: https://www.globalpointofcare.abbott/en/product-details/panbio-covid-19-ag-antigen-test.html. (Accessed: 20th October 2020)

244. Linares, M. *et al.* Panbio antigen rapid test is reliable to diagnose SARS-CoV-2 infection in the first 7 days after the onset of symptoms. *J. Clin. Virol.* 104659 (2020). doi:10.1016/j.jcv.2020.104659

245. Maldonado, J. *et al.* Label-free detection of nosocomial bacteria using a nanophotonic interferometric biosensor. *Analyst* **145**, 497–506 (2020).

246. Whitt, M. A. Generation of VSV pseudotypes using recombinant ΔG-VSV for studies on virus entry, identification of entry inhibitors, and immune responses to vaccines. *J. Virol. Methods* **169**, 365–374 (2010).

247. Zou, L. *et al.* SARS-CoV-2 viral load in upper respiratory specimens of infected patients. *New England Journal of Medicine* **382**, 1177–1179 (2020).

248. Pan, Y., Zhang, D., Yang, P., Poon, L. L. M. & Wang, Q. Viral load of SARS-CoV-2 in clinical samples. *The Lancet Infectious Diseases* **20**, 411–412 (2020).

249. Wölfel, R. *et al.* Virological assessment of hospitalized patients with COVID-2019. *Nature* **581**, 465–469 (2020).

250. Sánchez-Santed, F., Colomina, M. T. & Herrero Hernández, E. Organophosphate pesticide exposure and neurodegeneration. *Cortex* **74**, 417–426 (2016).

251. WHO. *Fenitrothion in Drinking-water Background document for development of WHO Guidelines for Drinking-water Quality*. (2004).

252. Chough, S. H. *et al.* Organophosphorus hydrolase-based amperometric sensor: Modulation of sensitivity and substrate selectivity. *Electroanalysis* **14**, 273–276 (2002).

253. Richardson, J. R., Fitsanakis, V., Westerink, R. H. S. & Kanthasamy, A. G. Neurotoxicity of pesticides. *Acta Neuropathol.* **138**, 343–362 (2019).

254. Pope, C., Karanth, S. & Liu, J. Pharmacology and toxicology of cholinesterase inhibitors: Uses and misuses of a common mechanism of action. in *Environmental Toxicology and Pharmacology* **19**, 433–446 (Elsevier, 2005).

255. Giordano, G. *et al.* Organophosphorus insecticides chlorpyrifos and diazinon and oxidative stress in neuronal cells in a genetic model of glutathione deficiency. *Toxicol. Appl. Pharmacol.* **219**, 181–189 (2007).

256. Çakir, Ş. & Sarikaya, R. Genotoxicity testing of some organophosphate insecticides in the Drosophila wing spot test. *Food Chem. Toxicol.* **43**, 443–450 (2005).

257. Rahman, M. F., Mahboob, M., Danadevi, K., Saleha Banu, B. & Grover, P. Assessment of genotoxic effects of chloropyriphos and acephate by the comet assay in mice leucocytes. *Mutat. Res. - Genet. Toxicol. Environ. Mutagen.* **516**, 139–147 (2002).

258. Yeh, S. P., Sung, T. G., Chang, C. C., Cheng, W. & Kuo, C. M. Effects of an organophosphorus insecticide, trichlorfon, on hematological parameters of the giant freshwater prawn, Macrobrachium rosenbergii (de Man). *Aquaculture* **243**, 383–392 (2005).

259. WHO. *Specifications and evaluations for public health pesticides: Fenitrothion O,O-dimethyl O-4-nitro-m-tolyl phosphorothioate*. (2010).

260. Wang, D., Naito, H. & Nakajim, T. The Toxicity of Fenitrothion and Permethrin. *Insectic. - Pest Eng.* (2012). doi:10.5772/27884

261. FAO/WHO. *Fenitrothion (FAO/PL:1969/M/17/1)*. (2000).

262. United States Environmental Protection Agency. *Reregistration Eligibility Decision for Fenitrothion*. (1995).

263. FAO, W. and. *Pesticide Residues in Food*. (2003).

264. Smith, A. G. & Gangolli, S. D. Organochlorine chemicals in seafood: Occurrence and health concerns. *Food and Chemical Toxicology* **40**, 767–779 (2002).

265. Kumar, P., Kim, K. H. & Deep, A. Recent advancements in sensing techniques based on functional materials for organophosphate pesticides. *Biosens. Bioelectron.* **70**, 469–481 (2015).

266. Li, Z. & Jennings, A. *Worldwide regulations of standard values of pesticides for human health risk control: A review*. *International Journal of Environmental Research and Public Health* **14**, (2017).

267. WHO. *Guidelines for drinking-water quality, 4th edition, incorporating the 1st addendum*. (WHO, 2017).

268. WHO. *A global overview of national regulations and standards for drinking-water quality*. (2018).

269. Schellin, M., Hauser, B. & Popp, P. Determination of organophosphorus pesticides using membrane-assisted solvent extraction combined with large volume injection–gas chromatography–mass spectrometric detection. *J. Chromatogr. A* **1040**, 251–258 (2004).

270. Sánchez, M. E., Méndez, R., Gómez, X. & Martín-Villacorta, J. Determination of diazinon and fenitrothion in environmental water and soil samples by HPLC. *J. Liq. Chromatogr. Relat. Technol.* **26**, 483–497 (2003).

271. Sherma, J. Pesticides. *Anal. Chem.* **65**, 40–54 (1993).

272. Grigoryan, H. *et al.* Mass spectral characterization of organophosphate-labeled lysine in peptides. *Anal. Biochem.* **394**, 92–100 (2009).

273. Thompson, C. M., Prins, J. M. & George, K. M. Mass spectrometric analyses of organophosphate insecticide oxon protein adducts. *Environmental Health Perspectives* **118**, 11–19 (2010).

274. Wang, J., Chatrathi, M. P., Mulchandani, A. & Chen, W. Capillary electrophoresis microchips for separation and detection of organophosphate nerve agents. *Anal. Chem.* **73**, 1804–1808 (2001).

275. Watanabe, E. *et al.* Enzyme-linked immunosorbent assay based on a polyclonal antibody for the detection of the insecticide fenitrothion. Evaluation of antiserum and application to the analysis of water samples. *J. Agric. Food Chem.* **50**, 53–58 (2002).

276. Hua, X. *et al.* Development of an Enzyme Linked Immunosorbent Assay and an Immunochromatographic Assay for Detection of Organophosphorus Pesticides in Different Agricultural Products. *PLoS One* **7**, (2012).

277. Ensafi, A. A., Rezaloo, F. & Rezaei, B. Electrochemical

Determination of Fenitrothion Organophosphorus Pesticide Using Polyzincon Modified-glassy Carbon Electrode. *Electroanalysis* **29**, 2839–2846 (2017).

278. Qi, P. *et al.* Sensitive determination of fenitrothion in water samples based on an electrochemical sensor layered reduced graphene oxide, molybdenum sulfide (MoS2)-Au and zirconia films. *Electrochim. Acta* **292**, 667–675 (2018).

279. Kant, R. Surface plasmon resonance based fiber–optic nanosensor for the pesticide fenitrothion utilizing Ta2O5 nanostructures sequestered onto a reduced graphene oxide matrix. *Microchim. Acta* **187**, 1–11 (2020).

280. Huertas, C. S., Fariña, D. & Lechuga, L. M. Direct and Label-Free Quantification of Micro-RNA-181a at Attomolar Level in Complex Media Using a Nanophotonic Biosensor. *ACS Sensors* **1**, 748–756 (2016).

281. Maldonado, J., González-Guerrero, A. B., Domínguez, C. & Lechuga, L. M. Label-free bimodal waveguide immunosensor for rapid diagnosis of bacterial infections in cirrhotic patients. *Biosens. Bioelectron.* **85**, 310–316 (2016).

282. Chocarro-Ruiz, B. *et al.* A CO2 optical sensor based on self-assembled metal-organic framework nanoparticles. *J. Mater. Chem. A* **6**, 13171–13177 (2018).

283. Mauriz, E. *et al.* Direct surface plasmon resonance immunosensing of pyraclostrobin residues in untreated fruit juices. *Anal. Bioanal. Chem.* **404**, 2877–2886 (2012).

284. NHMRC. *Australian Drinking Water Guidelines*. (2018).